Ph.D. DISSERTATION

Micro-Structured Anisotropic Elastomer Composite-Based Electrical Components for Soft Electronics

유연 전자 회로를 위한 마이크로 구조의
이방성 엘라스토머 복합소재 기반 전자 소자

February 2023

DEPARTMENT OF ELECTRICAL AND COMPUTER ENGINEERING
COLLEGE OF ENGINEERING
SEOUL NATIONAL UNIVERSITY

JISEOK SEO

Micro-Structured Anisotropic Elastomer Composite-Based Electrical Components for Soft Electronics

유연 전자 회로를 위한 마이크로 구조의 이방성 엘라스토머 복합소재 기반 전자 소자

지도교수 홍 용 택

이 논문을 공학박사 학위논문으로 제출함
2023 년 2 월

서울대학교 대학원
전기 · 정보 공학부
서 지 석

서지석의 공학박사 학위논문을 인준함
2023 년 2 월

위 원 장	정 윤 찬	(인)
부위원장	홍 용 택	(인)
위 원	곽 정 훈	(인)
위 원	Steve Park	(인)
위 원	정 승 준	(인)

Abstract

Micro-Structured Anisotropic Elastomer Composite-Based Electrical Components for Soft Electronics

Jiseok Seo
Department of Electrical and Computer Engineering
College of Engineering
Seoul National University

Soft electronics provide stretchability beyond flexibility, enabling the implementation of a device capable of various deformations which are not realizable with a flexible device. In order to implement futuristic applications with soft electronics, a multi-functional system in which various single-level devices are integrated on the stretchable platform is needed. The components for the highly integrated multi-functional system can be divided into three main categories: a single-level functional device, a VIA for integrating each functional device in 3D scheme, and a probe unit forming electrical connections for signal transfer and inspection of fabricated devices. The material-based and structure-based strategies are applied to impart not only the softness, but also the functionality suitable for each role to the device components. In this dissertation, the novel strategies for implementing three main components on the stretchable platform for the highly

integrated multi-functional system, by combining magnetically induced anisotropic structure of composite and micro-perforated membrane, are discussed.

As a single-level active device for the multi-functional system, soft pressure sensor arrays with high resolution up to 100 ppi that can cover the resolution of various types of human tactile sense are developed. Patternability of ferromagnetic composite with the magnetic field is analyzed through the finite element analysis (FEA) and the need of a frame for isolation of sensor pixels is discussed. By introducing the micro-perforated membrane to the composite, the spatial resolution of pressure sensor arrays is determined as 100 ppi through the two-point discrimination test. Consequently, the real-time pressure mapping and categorization in the resolution of 100 ppi is demonstrated using the readout system.

As a connector for the signal transfer and inspection process, the soft probe unit that prevents damage to the electrodes on deformable electronic devices caused by the physical contact is developed. With optimized replication process for the perforated membrane, the 500 ppi SPU without crosstalk within the contact electrodes is obtained. The low contact resistance and protective characteristics of the SPU are verified with application to the inkjet-printed electrodes on the flexible substrate. The feasibility of proposed SPU to the practical usage is confirmed with introduction to the commercial FPCB connector for inspection process and electrodes for solution-processed PLED.

As a connecting link for integration of single-level devices, the mechanically durable stretchable VIA enabling the facile bottom-up stacking process

is developed. The effect of micro-structures on dispersion of the mechanical stress to the elastomeric substrate under the stretched state is investigated with FEA simulation and digital image correlation (DIC) analysis of real samples. The mechanical durability and reliability of proposed VIA are verified with the stretching test and electrical measurement combining the transmission line method and 4-wire measurement method. To show the feasibility of proposed approach to the multi-layered stretchable electronics applications, stretchable passive matrix LED arrays operating stably under crumpled or biaxially stretched states are demonstrated.

This study provides the novel methodologies for realization of key components for highly integrated stretchable electronics utilizing the micro-structured anisotropic elastomer composite. Impartment of functionality and enhancement of device performance are carried out with formation of the magnetic field, change of filler characteristics, and introduction of micro-structures. In addition to the verified feasibility of proposed methodologies, facile and large-area processability of the micro-perforated membrane fabricated by utilizing a mold facilitates the commercialization of the proposed technology. It is expected that systematic approaches to implementing soft electrical components through design, analysis, and optimization in this dissertation will pave the way for realization of highly integrated multi-functional stretchable electronic systems.

Keywords: Soft electronics, Elastomer composite, Pressure sensor, Probe unit, Vertical Interconnect access, Micro-structure, Anisotropic composite, Ferromagnetic

Student Number: 2016-20919

Table of Contents

List of Tables

List of Figures

Chapter 1. Introduction

1.1. Soft Electronics

Soft electronics enables implementation of the device capable of various deformations that cannot be realized with a flexible device by granting stretchability beyond flexibility. It has been widely studied due to the possibilities to be applied to various practical applications via new form factors, such as human-machine interfaces,[1, 2] health monitoring system,[3-5] electronic skin,[6, 7] and soft robotics as shown in Figure 1.1.[8, 9] Considering that implementation of the flexible display enables the commercialization of foldable smartphones which were not realizable before, the development of soft electronics will open a new era of wearable devices. People's desire to have access to their electronic devices anytime anywhere became the trigger for the development of wearable electronics. Although products such as a smart watch that reduce the bulkiness of wearable devices have been commercialized thanks to the technology development of semiconductors and batteries, they still have a rigid form factor with a bad fit. Eventually, it is possible to realize compact and comfortable devices with conformability through the implementation of soft electronics such as skin-attachable devices (Figure 1.2). To make conformal contact on the surface with uneven 3D morphologies like skin, softness is required throughout the entire device.

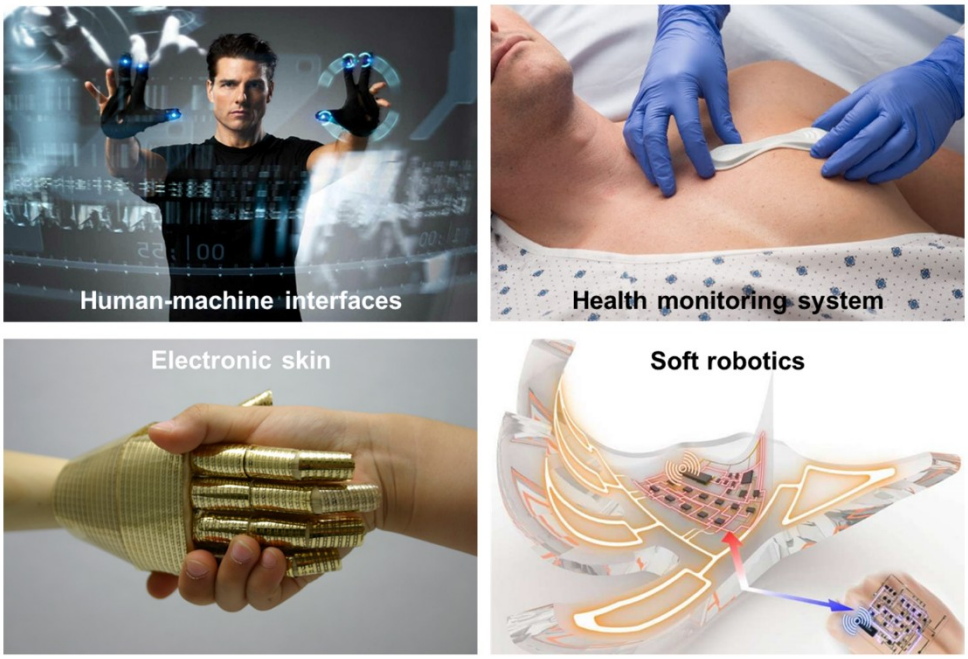

Figure 1.1 | Various applications of soft electronics. Human-machine interfaces (Source: Movie "Minority Report"),[10] health monitoring system (Source: VitalConnect),[11] electronic skin (Source: T. Someya group),[12] and soft robots[8] can be implemented with soft electronics.

Figure 1.2 | The evolution of wearable electronics. Through introduction of soft electronics, rigid and bulky device is converted into the compact device with conformal and comfortable fit. (Source: Seiko,[13] Samsung,[14] and Y. Hong group[8])

In general, stretchable materials have lower performance in terms of functionality compared to rigid or crystalline materials, due to the amorphous phase that the molecules are loosely bound to each other. To overcome the problem of low performance, the concept of stretchable hybrid electronics was introduced. The performance of stretchable electronics is improved by attaching a high-performance silicon chip on the stretchable platform or forming brittle elements with high-performance on rigid structures formed on the substrate.[15-20] Although it is fine as an intermediate step on the way to realizing high-performance soft electronics, it is not the final destination of soft electronics due to poor conformability and limited stretchability due to the rigid parts. Therefore, more studies on imparting intrinsic stretchability to each functional device should be conducted.

1.2. Various Strategies for Realization of Soft Electronics

1.2.1. Material-Based Strategies

Among various novel strategies for realization of soft electronics, imparting softness to the material used to fabricate the stretchable device is one of the easiest approaches. By using intrinsically stretchable materials that can endure the applied strain due to various deformation such as bending and stretching, soft electronics can be implemented without any complex design or fabrication process. Devices composed of soft materials offer comfortable usability induced by the softness and conformal contact with 3D morphologies. Intrinsically stretchable materials have been widely studied including stretchable polymer,[21-23] liquid metal,[24-26] network of 1D material,[27-29] and elastomer composite.[30-32] These soft materials are used to convert conventional rigid devices into stretchable devices with functionality suitable for each characteristic. Figure 1.3 summarizes the aforementioned examples of material-based strategies.

In the case of stretchable polymer, various physical properties such as electrical and mechanical characteristics can be controlled by the molecular engineering. Through several novel strategies, controlling stretchability and functionality of the polymer is possible: engineering of side chains to control crystallinity,[33] blending additives for phase separation or change of crystallinity,[22, 34, 35] and copolymerization for introduction of rigid and soft parts.[36-38] The polymer can be applied to various stretchable devices including electrode, sensor, light-emitting

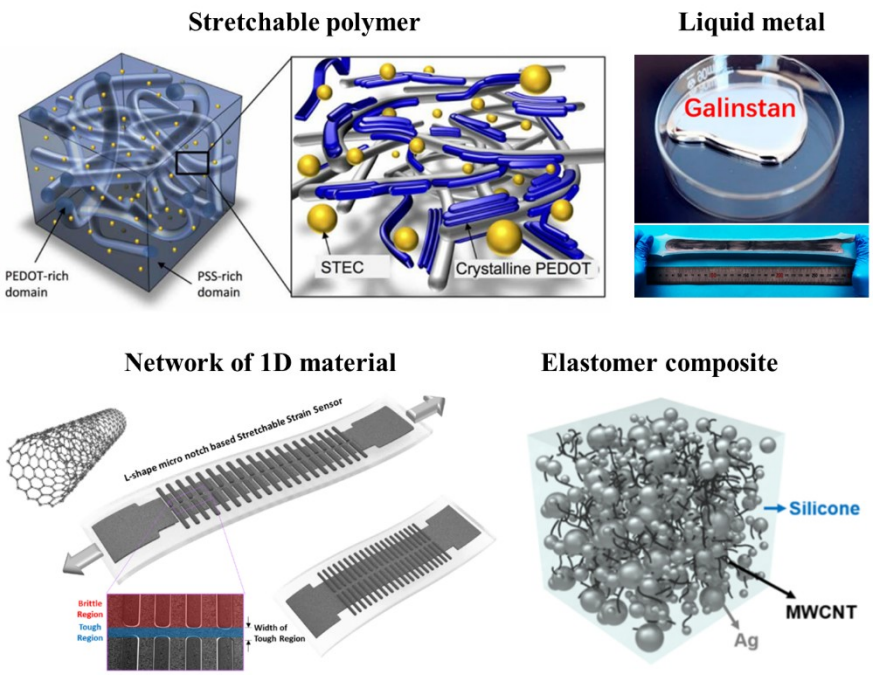

Figure 1.3 | Material-based strategies for soft electronics: stretchable polymer,[22] liquid metal,[24] network of 1D material,[29] and elastomer composite.[31]

diode, and transistor through the precise design of the polymer for the functionality of the device.

Liquid metal is widely used as stretchable electrodes due to its high conductivity originated from the nature of metal and high stretchability induced by the liquid-phase. However, the leakage issue of liquid metal makes it difficult to be integrated with other components because the careful encapsulation is needed. Since the liquid metal only shows the metallic property, it is used in the form of elastomer composite for impartment of various functionality.

1D materials such as metal nanowire and carbon nanotube (CNT) exhibit stretchability as sliding motion among the wires occurs during stretching through the formation of random network. In particular, CNT is applied to various applications such as electrode, sensor, and transistor thanks to not only its stretchability, but also its superior mechanical and electrical characteristics including the semiconducting property according to the chirality.

Elastomer composite can realize various functionality in addition to the stretchability by forming the mixture of elastomer and fillers including the materials mentioned above. No limitations on material selection and no need of complicated material engineering for stretchability facilitate the wide application of elastomer composite to various stretchable devices.

1.2.2. Structure-Based Strategies

Although it is desirable to configure all components with soft materials for the implementation of stretchable electronics, impartment of softness is not always possible in various functional devices. Precise engineering of materials for both good stretchability and desired characteristics is a formidable task. In addition, in the case of forming elastomer composite with the functional material, electrical performance of the material is degraded because the elastomer acts as a dielectric layer to hinder the flow of charges. Therefore, in order to implement stretchable electronics without degradation of device performance, a platform where materials used in the conventional rigid device can be applied is required. Many researches on structural

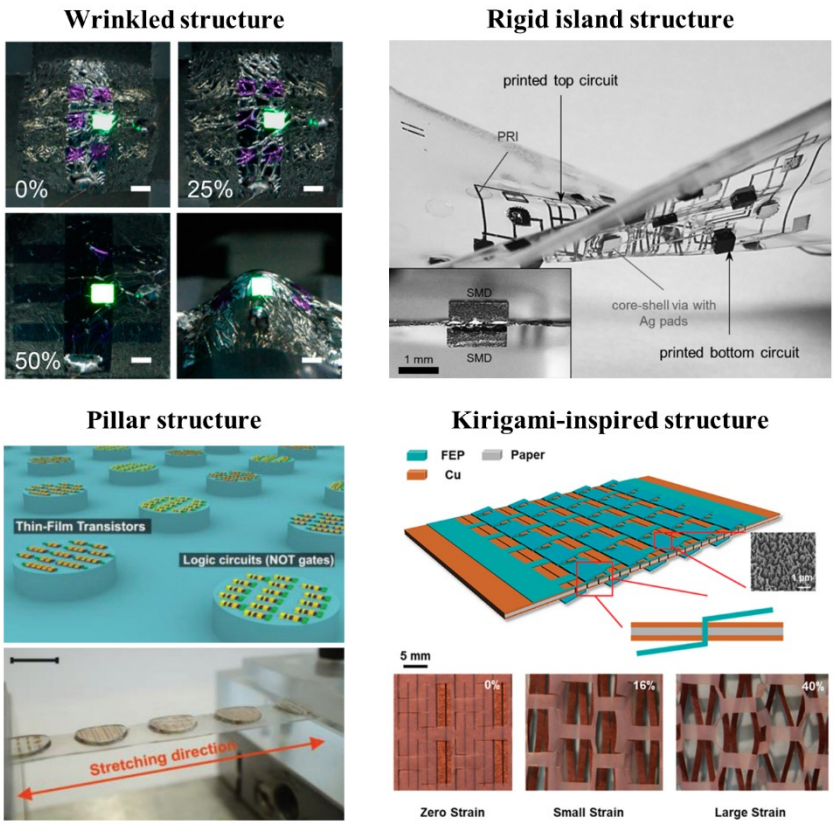

Figure 1.4 | Structure-based strategies for soft electronics: wrinkled,[39] rigid island,[16] pillar,[45] and kirigami-inspired structures.[46]

design of the substrate that can protect rigid materials from the mechanical stress have been investigated including wrinkled structures,[15, 39, 40] rigid islands,[16, 41, 42] pillar structures,[43-45] and kirigami-inspired structures.[46-49] Through these structure-based approaches, conversion of conventional rigid devices into stretchable devices is possible without material engineering. Figure 1.4 summarizes the aforementioned examples of structure-based strategies.

With pre-stretching of the substrate before fabrication of the upper layers, randomly wrinkled structures are obtained when the substrate is released to the pristine state. This wrinkle structure guarantees stretchability up to the strain that was pre-stretched even with the brittle material that is vulnerable to strain. However, there are still problems of scalability due to need of manual operation for pre-stretching, poor compatibility of the pre-stretched substrate with other fabrication processes, and alignment issue caused by pre-stretching.

The rigid island structure formed with the material with high Young's modulus compared to the substrate protect the device fabricated above from the applied strain by dispersion of stress to the soft substrate. The brittle devices can be formed on the rigid island using the existing fabrication process. Although the device on the rigid island is perfectly protected from strain regardless of brittleness, the issue of mechanical durability due to heterogeneity of the substrate and rigid island still exists. The concentrated strain due to difference in modulus causes the irreversible fracture and delamination at the interface of the substrate and rigid island, resulting in the limitations on the stretchability.

By forming protruding pillar structures with the trench, the device above the pillar is protected from the mechanical stress because the strain is concentrated on the thin trench. Although the substrate including the pillar and trench consists of the homogeneous material compared to the substrate with rigid islands, stretchability is limited due to existence of the strain-concentrated region. In addition, due to the difference in thickness between pillar and trench, it is difficult to form

interconnections between devices formed on pillars, which hinders the implementation of the system through integration of devices.

The kirigami-inspired method induces the rotational or three-dimensional deformation of the substrate by removal of unnecessary parts or making cuts in the substrate. Through the exquisite design of the kirigami structure, the brittle parts of the substrate become free from the strain by converting the tensile deformation on two-dimensional scheme to the rotational deformation on three-dimensional scheme. Because it accompanies 3D deformation, the usage of this method is limited when the substrate is attached to 3D morphology through conformal contact. Additionally, the scalability issue arises due to complex and limited design of kirigami structure and the low fill-factor of the devices on the intact region.

1.3. Motivation

In order to implement aforementioned applications such as health monitoring device and human-machine interfaces with soft electronics, a multi-functional system in which various single-level devices are integrated is needed (Figure 1.5). Three main components are needed for realization of highly integrated multi-functional system: a single-level active device performing each function (e.g. light-emitting diode, transistor, and sensor), a VIA enabling high density integration through the connection in the 3D scheme between each functional device, and a probe unit forming electrical connections for signal transfer and inspection of fabricated devices. When implementing these types of components on the stretchable platform, an approach using an intrinsically stretchable material is more suitable for integration with various devices than an approach that gives stretchability through structural design to a brittle device. Therefore, the elastomer composite was considered as a candidate for stretchable material due to its wide variety of functionalities according to the filler. In addition, in order to introduce the additional functionalities while retaining stretchability of the composite, introduction of the perforated structure with through-holes was examined.

The elastomer composite is applied to the various applications due to the availability of controlling material characteristics with ease, such as the conductor,[50] heat conductor,[51] semiconductor,[52] luminescent device,[53] and pressure sensor as shown in Figure 1.6.[54] The device performance originated from the filler properties

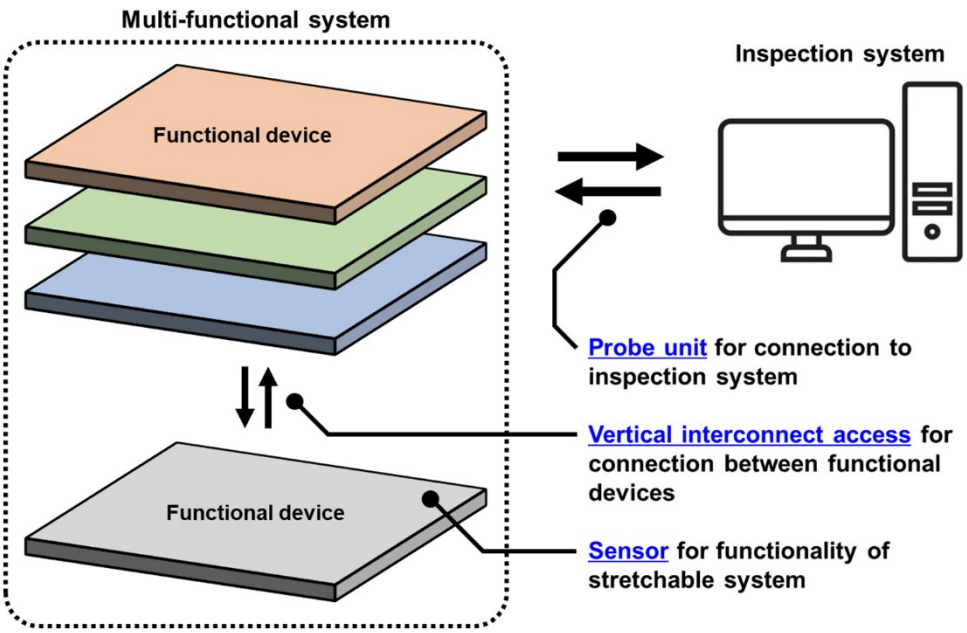

Figure 1.5 | Main concept for realization of multi-functional system. The single-level functional device, VIA, and probe unit are required for formation, operation, and inspection of the highly integrated multi-functional system.

can be controlled by varying the filler concentration. Especially, when the ferromagnetic particle is used as the filler, changes of the filler structure induced by the magnetic field enables control of device performance with the magnetic field in addition to the filler concentration. In addition, the percolation threshold of the anisotropic composite formed with the magnetic field decreases due to the filamentous structure, which leads the same conductivity with the isotropic composite with higher filler concentration.[55-57] Reduction of the filler concentration of the anisotropic composite for the same conductivity with the isotropic composite causes the decrease of Young's modulus of the composite.[58] Accordingly, usage of

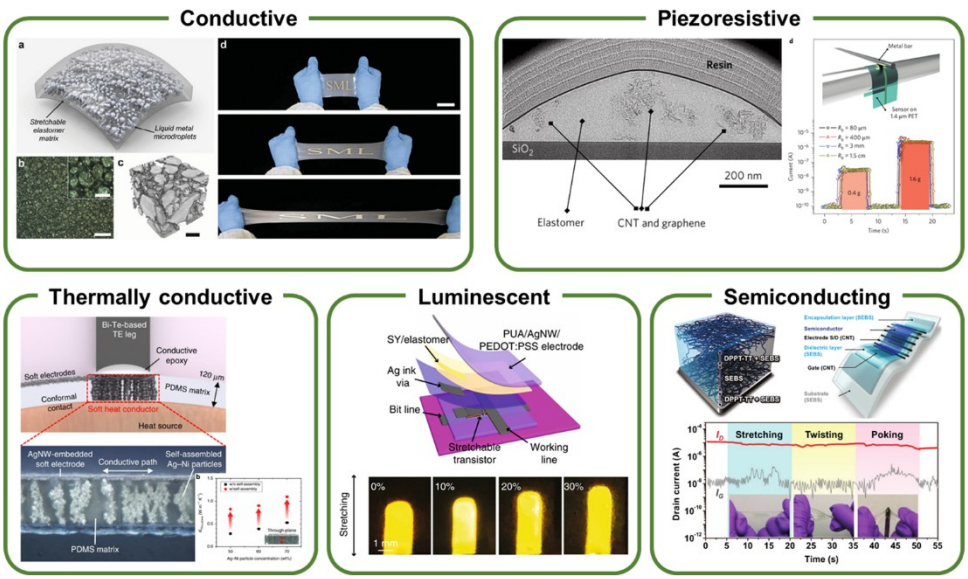

Figure 1.6 | Various functionalities of elastomer composite. The composite can show conductive,[50] piezoresistive,[54] thermally conductive,[51] luminescent,[53] and semiconducting properties by varying the filler.[52]

ferromagnetic particle as the filler reinforces the elastomeric characteristic of the composite, stretchability.

To achieve additional characteristics that cannot be satisfied by the elastomer composite alone, the micro-perforated structure was introduced. As shown in Figure 1.7, the perforated structures with periodic through-hole patterns are used for various purposes, including making patterns,[59-61] filtering particles,[62-64] connecting two different layers,[65, 66] and imparting mechanical durability to the substrate.[67-69] The perforated membrane can be fabricated with facile process of replicating the structure of the mold.[70-72] Particularly, when the etched silicon wafer is used as a master mold, a low-cost, high-resolution, and large-area process is

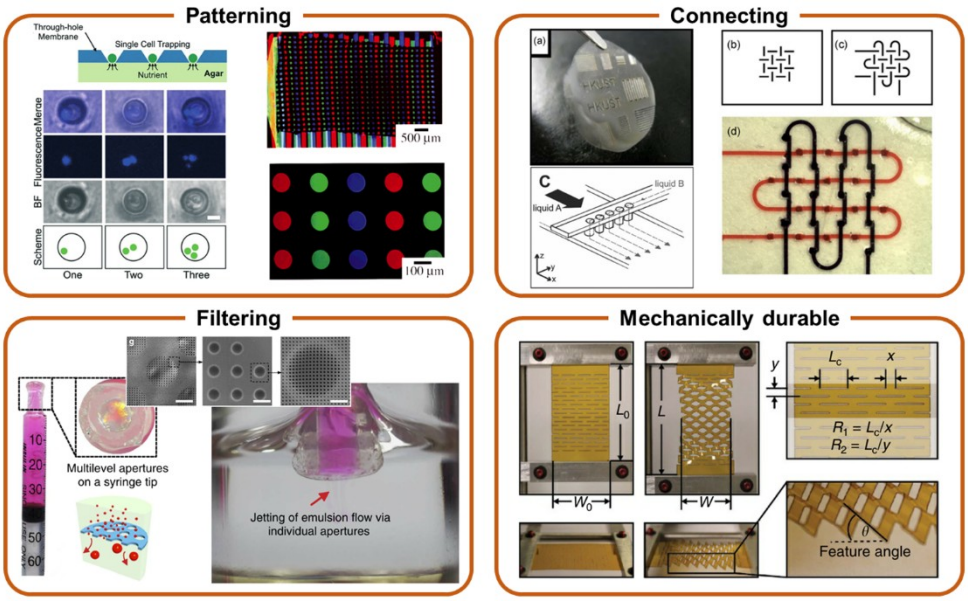

Figure 1.7 | Various functionalities of perforated membrane. The perforated structures are used for various purposes, including making patterns,[59, 61] filtering particles,[62] connecting two different layers,[65, 66] and imparting mechanical durability to the substrate.[67]

possible because the mold can be used semi-permanently and no additional photo-lithography process is required. By applying the perforated structure, elimination of lateral conduction path by high-resolution patterning of the composite and enhancement of mechanical reliability by introduction of micro-structures can be achieved. In conclusion, the novel strategies for implementing three main components on the stretchable platform for the highly integrated multi-functional system, by combining magnetically induced anisotropic structure of composite and micro-perforated membrane, will be discussed in this dissertation.

1.4. Organization of This Dissertation

This dissertation consists of five chapters, including Introduction and Conclusion. Chapter 1 introduces the importance, aim, and implementation of soft electronics including brief description about two main strategies for realization of soft electronics. Implementation of key components on the stretchable platform for the highly integrated system through two main approaches, elastomer composite and perforated membrane, which can impart various functionalities in addition to stretchability is discussed.

Chapter 2 introduces highly sensitive soft pressure sensor arrays with high resolution that can mimic the human tactile sense. Patternability of ferromagnetic composite with the magnetic field is analyzed through the finite element analysis (FEA) and the need of a frame for isolation of sensor pixels is discussed. By introducing the micro-perforated membrane to the composite, the spatial resolution of pressure sensor arrays is determined as 100 ppi through the two-point discrimination test. Consequently, the real-time pressure mapping and categorization in the resolution of 100 ppi is demonstrated using the readout system.

Chapter 3 introduces a soft probe unit that can make electrical connections without damaging the electrodes on the deformable substrate. With optimized replication process for the perforated membrane, the 500 ppi SPU without crosstalk within the contact electrodes is obtained. The low contact resistance and protective characteristics of the SPU are verified with application to the inkjet-printed

electrodes on the flexible substrate. The feasibility of proposed SPU to the practical usage is confirmed with introduction to the commercial FPCB connector for inspection process and electrodes for solution-processed PLED.

Chapter 4 introduces a mechanically durable stretchable vertical interconnect access that enables the facile bottom-up stacking process for the multi-layered system. The effect of micro-structures on dispersion of the mechanical stress to the elastomeric substrate under the stretched state is investigated with FEA simulation and digital image correlation (DIC) analysis of real samples. The mechanical durability and reliability of proposed VIA are verified with the stretching test and electrical measurement combining the transmission line method and 4-wire measurement method. To show the feasibility of proposed approach to the multi-layered stretchable electronics applications, stretchable passive matrix LED arrays operating stably under crumpled or biaxially stretched states are demonstrated.

Finally, Chapter 5 summarizes the motivation, proposed strategies, and achievements including demonstration of practical applications, explained in this dissertation.

Chapter 2. High Resolution Soft Pressure Sensor for Electronic Skin

2.1. Introduction

Electronic skin (e-skin) senses diverse external stimuli (temperature, humidity, strain, pressure, etc.) through conversion of stimuli into electrical signals with a sensor. Especially, a pressure sensor that can detect applied forces to the e-skin enables mimicking one of the most frequently used human senses in daily life, a tactile sense. As show in Figure 2.1, the pressure sensor can be divided into four different types

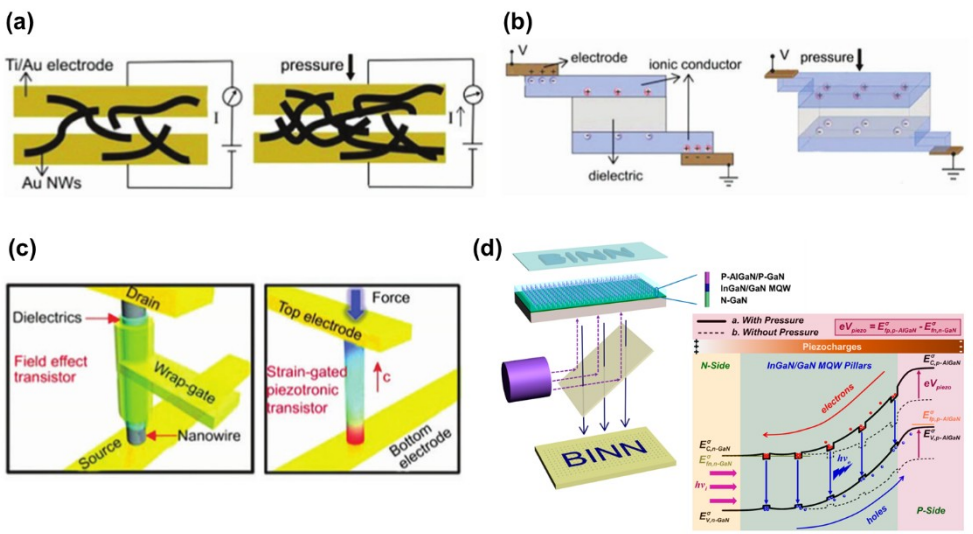

Figure 2.1 | Types of pressure sensor according to the sensing mechanisms: (a) piezoresistive,[73] (b) piezocapacitive,[76] (c) piezoelectric,[78] and (d) piezophototronic pressure sensors.[82]

according to the sensing mechanisms, piezoresistive,[73-75] piezocapacitive,[3, 76, 77] piezoelectric,[78-80] and piezophototronic type.[81-83] The piezoresistive pressure sensor that the applied pressure induces change of resistance has the advantage of easy signal collection and wide detection range. However, the power dissipation problem and limitations on the spatial resolution remain as an obstacle to e-skin applications. Although the capacitive pressure sensor can be fabricated with high resolution in a large area due to the crossover structure of electrodes, it needs complex readout circuits. In the case of piezoelectric and piezophototronic pressure sensors, in spite of high resolution processability and fast response time, it is hard to apply these sensors to e-skin applications due to the complex signal collection and limitations on stretchability.

Recently, realization of e-skin has been investigated to achieve sufficient spatial resolution for mimicking the tactile sense by integrating a large number of sensors as shown in Figure 2.2.[84, 85] Additionally, active components such as

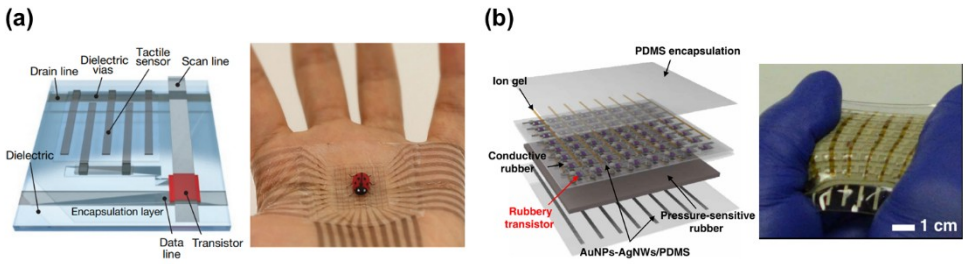

Figure 2.2 | Examples of e-skin realized with integrated pressure sensor arrays. Intrinsically stretchable pressure sensor arrays with (a) CNT-based pressure sensor and (b) elastomer composite-based pressure sensor.[84, 85]

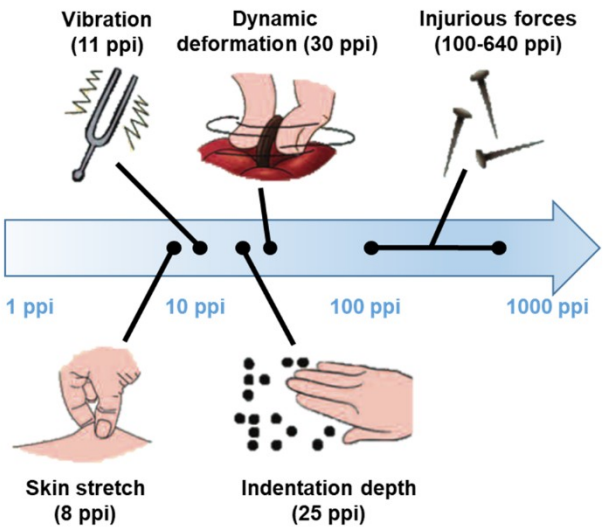

Figure 2.3 | Resolution of the human tactile sense according to the skin stimulus. The resolution was calculated from the tactile receptor density.[90]

transistor[86, 87] or Schottky diode junction[88, 89] are integrated with pressure sensor arrays to enhance the device performance of sensitivity or detection range. However, these methods are not compatible with the low-cost and large-area fabrication process because complex and time-consuming processes such as photolithography are needed to implement the sensor arrays. In addition, due to relatively low resolution compared to human tactile receptors, not all mechanical stimuli including injurious forces can be handled as shown in Figure 2.3.[90] For realization of high resolution pressure sensor arrays exceeding 100 ppi, pressure mapping was demonstrated utilizing the electroluminescent imaging technique (Figure 2.4). With piezoelectric nanowire LED or quantum-dot LED, high resolution that exceed resolution of the human tactile sense could be achieved by sensing the illumination at the pressure-applied region.[82, 91] However, due to need of optical systems including

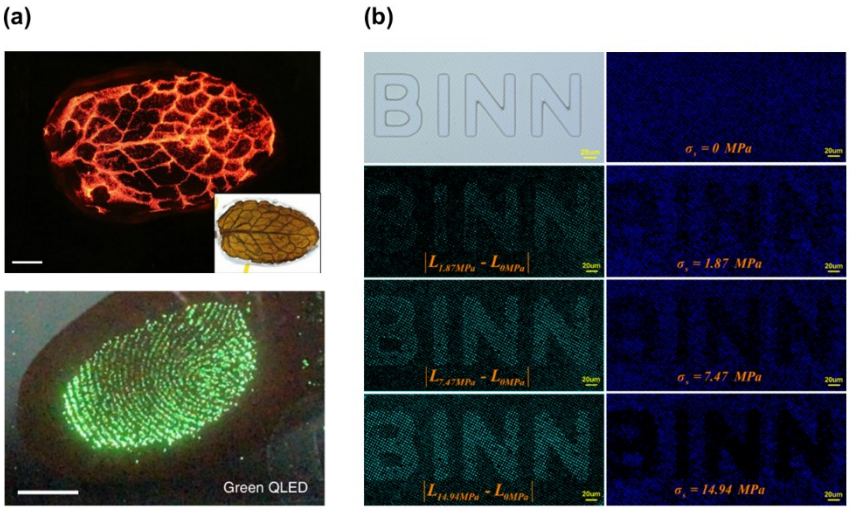

Figure 2.4 | Examples of high-resolution pressure sensor arrays utilizing the electroluminescent imaging technique. (a) Quantum-dot LED and (b) piezoelectric nanowire LED were used to indicate the pressure-applied region.[82, 91]

the image sensor for signal collection, application to the wearable device is limited. Therefore, a facile strategy for soft and high resolution pressure sensor arrays whose signal can be easily obtained is needed to realize e-skin applications.

In this chapter, soft pressure sensor arrays with high resolution up to 100 ppi that can cover the resolution of various types of human tactile sense utilizing the anisotropic elastomer composite and micro-perforated elastomer membrane are reported. When the magnetic field is applied to the composite with ferromagnetic fillers, ferromagnetic particles in the elastomer matrix form anisotropic filamentous structures along the direction of the magnetic field. Due to the filamentous structures, sensitivity of the pressure sensor can be highly enhanced when the pressure is applied

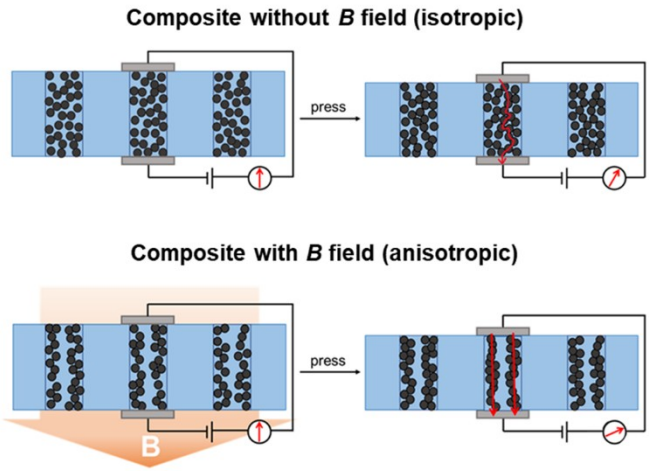

Figure 2.5 | Mechanisms for enhanced sensitivity of the anisotropic composite. Even when the same pressure is applied, the number of generated conduction paths is much higher in the case of anisotropic composite.

(Figure 2.5). In the case of isotropic composite that fillers are uniformly distributed in the composite, charges cannot flow directly along the direction of the electric field even when the inter-particle distance is shortened due to the pressure. Charges have to move through adjacent particles to make the conduction path longer, resulting in small conductivity change according to the applied pressure. On the other hand, due to the filamentous structures, the amount of generated conduction paths is high even at the low pressure. Therefore, the pressure sensor fabricated with anisotropic composite shows high sensitivity compared to the isotropic composite. By combining the anisotropic composite with the micro-perforated membrane that is used to pattern the composite in high resolution up to 100 ppi, pressure sensor arrays without crosstalk between neighboring pixels were implemented. In addition, real-time mapping and categorization of applied forces were demonstrated with the readout system of 2,304 pixels to show the feasibility of the proposed pressure sensor to be applied to e-skin applications.

2.2. Experimental Section

2.2.1. Materials

Poly(dimethylsiloxane) (PDMS) was purchased from Dow Corning Corp. (Sylgard 184) and mixed with a curing agent at an appropriate ratio before use. Trichloro(1H,1H,2H,2H-perfluorooctyl)silane (FOTS) (Sigma-Aldrich) was used as an anti-adhesion agent that makes cured PDMS delaminate from the carrier substrate with ease. Silver nano-particle (AgNP) ink (DGP 40LT-15C, ANP Co., Ltd.) was used to fabricate electrodes with an inkjet-printer for readout of pressure sensor arrays. Poly(ethylene 2,6-naphthalate) (PEN) film with a thickness of 125 μm was purchased from DuPont Teijin Films (Teonex Q65HA) and used as a protective layer of the magnetic field modulator to prevent permeation of PDMS to the pillar structure. Spherically-shaped nickel (Ni) particles with a spiky morphology and a mean size of 3 - 6 μm (AH50, Hunter Chemical LLC.) were mixed with PDMS at the desired concentration to form the elastomer composite. Silver epoxy (LOCTITE ABLESTIK CE 3103WLV, Henkel Corp.) and 50 μm-thick copper wire (Nilaco Corp.) were used to make electrical connections between electrodes and the source measure unit.

2.2.2. Fabrication Process

Pressure sensor patterned with the magnetic field modulator: A pair of iron structured with pillar arrays as magnetic field modulators were installed at aluminum molds for alignment of the top and bottom modulators. PEN film was attached on the field modulator to prevent liquid PDMS from permeating the pillar structures. Spacers with an intended thickness were formed with Kapton tape on the PEN cover to maintain the uniform thickness of the substrate with pressure sensors throughout the area that the magnetic field is applied. After PDMS was mixed with a curing agent with a ratio of 10:1 using a paste mixer (ARE-310, Thinky), Ni particles were added as the desired concentration and mixed again. After the mixture of liquid PDMS and Ni particles with desired filler concentration was poured on the PEN cover, the sample was placed in the vacuum desiccator until all air bubbles in the composite were removed. Covering the sample with the top aluminum mold containing the field modulator was followed by tightening screws of the mold to avoid the misalignment of modulators induced by the magnetic force. A pair of samarium-cobalt permanent magnets were attached to the top and bottom field modulators. The sample was left for 10 min to give enough time for rearrangement of ferromagnetic particles in the magnetic field and cured at 100 °C for 1 h in the convection oven.

Pressure sensor patterned with the micro-perforated membrane: The perforated membrane fabricated with the PDMS mold using the replication process was laminated to the PEN-attached glass carrier substrate. Spacers having the same

thickness as the membrane were attached to prevent the membrane from distortion due to the pressure caused by the magnetic force between a pair of magnets. Mixture of liquid PDMS and Ni particles with desired filler concentration was poured on the membrane. To make the mixture fill the holes at the membrane, the sample was placed in the vacuum desiccator until all air bubbles were removed. After the air bubbles were entirely eliminated using the vacuum desiccator, the blade-coating was conducted to remove excess Ni particles and PDMS on the membrane. The top side of the sample was covered with the PEN-attached glass substrate to prevent the composite from protruding when the magnetic field is applied. A pair of samarium-cobalt permanent magnets were placed at the top and bottom sides of the sample to apply the uniform magnetic field. The sample was left for 10 min to give enough time for rearrangement of ferromagnetic particles in the magnetic field and cured at 100 °C for 1 h in the convection oven.

Electrodes for readout of pressure sensor arrays: For the substrate of top electrodes that cover the top side of pressure sensor arrays, PDMS with the thickness of 100 μm was used to ensure that the pressure can be transmitted to the sensor pixel. For the surface treatment of an anti-adhesion agent, the glass carrier substrate was treated with the air-plasma at 100 W for 1 min (Cute-MPR, Femto Science) and left with FOTS solution in a desiccator connected with a vacuum pump overnight. After PDMS was spin-coated on the FOTS-treated carrier substrate at 1000 rpm for 1 min, PDMS was fully cured at 100 °C for 1h. For the hydrophilic surface of PDMS to achieve good wetting of AgNP ink, the PDMS substrate was treated with UV/O_3 for 30 min. Inkjet-printing of AgNP ink was conducted with a drop-on-demand inkjet-

printer (Dimatix 2831, Fujifilm Dimatix Inc.) at the platen temperature of 60 °C. For evaporation of residual solvents and sintering of AgNPs, the substrate was annealed at 150 °C for 1 h on the hot plate. In the case of bottom electrodes, the 500 μm-thick glass was used as the substrate. The inkjet-printing and annealing process were carried out with the glass substrate treated with UV/O_3 for 5 min. The width of electrodes and gap between neighboring electrodes were 150 μm and 100 μm.

2.2.3. Characterization

Basic electrical characteristics of the pressure sensor were measured using a Keithley 2400 SourceMeter (Tektronix, Inc.). The pressure sensor was sandwiched between top and bottom copper electrodes with a width of 1 mm fabricated on the FPCB. For two-point discrimination test and measurement of the leakage current, a semiconductor parameter analyzer (Agilent 4155C, Agilent Technologies Inc.) was used. Inkjet-printed silver electrodes on the glass substrate and the 100 μm-thick PDMS were used as bottom and top electrodes, respectively.

The pressure was applied and measured with a digital force gauge (DTG-1, Digitech Co., Ltd.) installed on an automatic test stand (ASM-1000, Digitech Co., Ltd.). The maximum detection range and resolution of the force gauge is 1000 gf and 0.1 gf. The automatic test stand can be controlled at the interval of 0.01 mm. A force gauge tip with a diameter of 7 mm was used to apply the force to the pressure sensor at the speed of 1 - 10 mm/min.

Optical images of pressure sensors were obtained with an optical microscope (DSC510, Olympus). A field emission scanning electron microscope (FE-SEM) (S-4800, Hitachi) was used to capture the images of PDMS mold, membrane, and cross section of the pressure sensor.

2.3. Results and Discussion

2.3.1. Patterning Method of the Pressure Sensor

Patterning of pressure sensor using the magnetic field was implemented due to the ferromagnetic filler of the elastomer composite for the sensor. Because ferromagnetic particles are dragged to the point where the magnetic field is strong compared to that of the surrounding area, the magnetic field modulator is introduced to concentrate the magnetic field as shown in Figure 2.6.[51] When a permanent magnet is attached to the bottom of the field modulator, the magnetic field is concentrated to each pillar structure due to the high permeability of iron. As shown in FEA simulation, by arranging a pair of modulators facing each other, the magnetic field is concentrated on the crossover. When the ferromagnetic particle is placed between

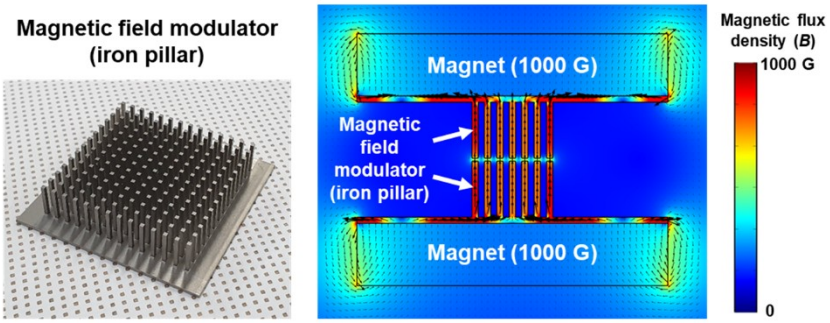

Figure 2.6 | Magnetic field modulator for concentration of the magnetic field. At the FEM simulation, the width of pillar, gap between pillars and the gap between top and bottom modulators is 1 mm, 2 mm, and 0.5 mm, respectively.

two modulators, the magnetic force on the ferromagnetic particle induced by ununiformity of the magnetic field can be expressed as[92, 93]

$$F = \mu_0 V M \cdot \nabla H \tag{3.1}$$

where μ_0 is the vacuum permeability, V is the volume of the particle, M is the magnetization, and H is the magnetic field intensity. The magnetic flux density B is related to H as follow

$$B = \mu_0(H + M) = \mu_0(1 + \chi)H = \mu_0 \mu_r H \tag{3.2}$$

where χ is the magnetic susceptibility, and μ_r is the relative permeability. By combining Equation (3.1) and (3.2), the magnetic force acting on the ferromagnetic particle can be rewritten as

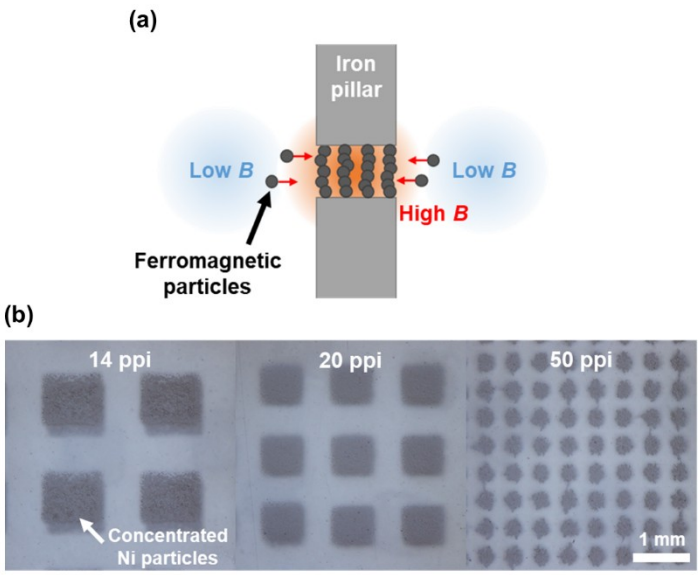

Figure 2.7 | Patterning of the ferromagnetic composite using the field modulator. (a) Mechanism for convergence of ferromagnetic particles in the ununiform magnetic field. (b) Composite patterned in various resolution by varying dimensions of the field modulator.

$$F = \frac{\chi}{\mu_0} VB \cdot \nabla B \tag{3.3}$$

In other words, the ferromagnetic particle in the ununiform magnetic field is dragged from the point where the magnetic field is weak to the point where the magnetic field is strong (Figure 2.7a). These converged particles are aligned along the direction of the magnetic field to form anisotropic filamentous structures. As shown in Figure 2.7b, by varying dimensions of the field modulators, ferromagnetic fillers in elastomer matrix were patterned in various resolution.

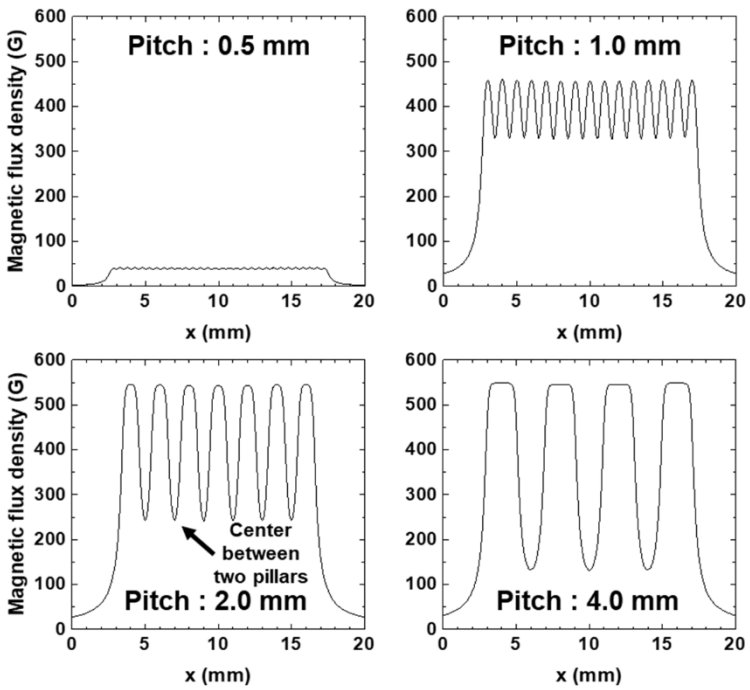

Figure 2.8 | FEA results of the magnetic flux density according to the pitch between iron pillars. A pair of modulators is arranged in facing each other with a gap between top and bottom modulators of 0.5 mm. The magnetic flux density at the middle of two modulators is depicted in each case.

In order to confirm the resolution limit of patterning process using the modulator, FEA simulation was conducted according to the pitch between iron pillars. The distance between a pair of modulators was set as 500 μm which was used as a parameter for fabrication of the stretchable substrate with pressure sensors. When the pitch of the pillars was changed, the ratio of the width of pillars to the gap between pillars was maintained as 1:1. The magnetic flux density at the middle of two modulators according to the pitch of iron pillars is depicted in Figure 2.8. As the pitch of pillar arrays decreases, the maximum magnetic flux density also decreases due to interference between pillar structures. This reduction of flux density according to the reduced pitch of iron pillars affects the patternability of ferromagnetic fillers using field modulators. For patterning of particles, particles distributed among pillars have to converge to the crossover of two facing modulators. Therefore, the magnetic force applied at the center between two pillars has the greatest influence on patternability because the flux density is minimum at this point as shown in Figure 2.9a. As Equation (3.3), the magnetic force is proportional not only to the flux density, but also to the gradient of the flux density. The norm of the gradient of flux density at the center between two pillars where the flux density is minimum is depicted according to the pitch of iron pillars (Figure 2.9b). As with the change in the maximum flux density, the norm of gradient of the flux density also decreases with the pitch. At the inset image of Figure 2.9b, as represented with white arrows, partially not-patterned ferromagnetic particles exist between the pillars in the case of the pitch with 0.5 mm. As a result, it is not possible to pattern the composite to

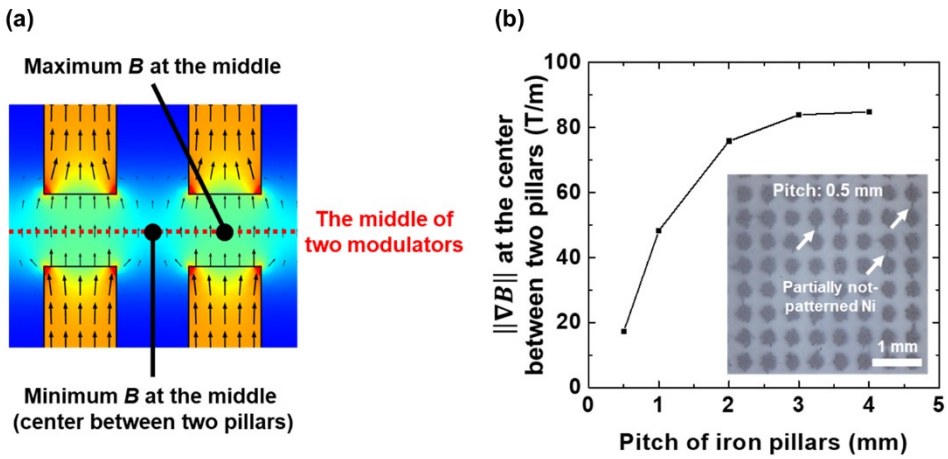

Figure 2.9 | Ununiform magnetic flux density induced by the field modulators. (a) Distribution of the magnetic flux density around the crossover of two field modulators. (b) The norm of gradient of the flux density at the center between two pillars according to the pitch of iron pillar.

fabricate pressure sensors with the pitch smaller than 0.5 mm using only field modulators.

To fabricate pressure sensors with higher spatial resolution compared to sensors fabricated with the field modulator, the perforated elastomer membrane with through-holes was considered as a frame for patterning the composite. The perforated membrane could be achieved through a facile replication method that PDMS replicates the structure of a mold. SEM images of PDMS pillar arrays used as a mold and perforated membrane are represented in Figure 2.10. The PDMS mold where PDMS pillars with a width of 150 μm and an aspect ratio of 2:1 are uniformly arranged in 250 μm-pitch was fabricated using a silicon master mold patterned through deep-etching process. Subsequently, the perforated membrane containing

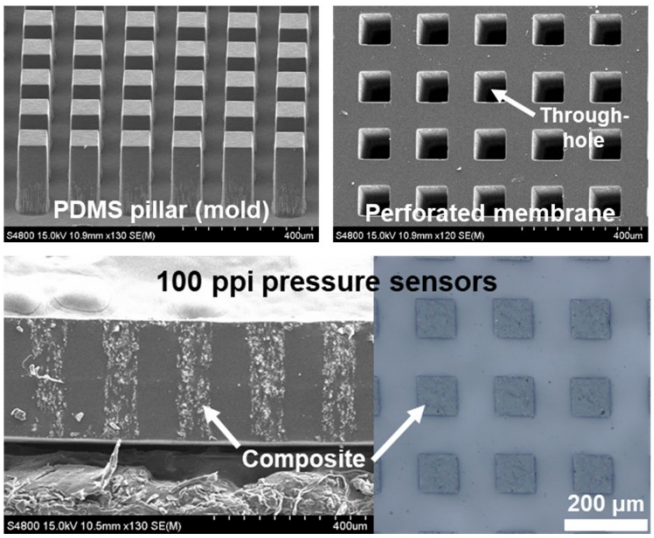

Figure 2.10 | SEM images of PDMS pillar arrays, perforated membrane, and high-resolution pressure sensor arrays. The optical image of pressure sensor arrays shows the top side of the arrays.

through-holes with the same dimension as the PDMS mold was successfully fabricated. Pressure sensor arrays with the same resolution of the mold was achieved by injecting the composite into the through-holes at the membrane. To mimic the human tactile receptors that can sense injurious forces like stabbing, the spatial resolution of pressure sensor was determined as 100 ppi. Detailed fabrication process of PDMS mold and perforated membrane will be discussed in Chapter 3.

2.3.2. Electrical Characteristics of the Pressure Sensor Patterned with a Perforated Membrane

To optimize the pressure sensor for wide operating pressure range and high sensitivity, pressure sensors with various filler concentration were fabricated. The characteristics of resistance change according to the applied pressure are depicted in Figure 2.11a. In the case of the composite with too low filler concentration, the resistance change was small because there was little current path formed despite the increased pressure. As the filler concentration increased, the resistance decreased further when the pressure was applied, resulting in the increase of sensitivity. In addition, increased number of conduction paths and enhanced contact resistance with electrodes affect the stable operation of the pressure sensor when the filler concentration was high. As a result, the composite with filler concentration of 70 wt% showed stable resistance change with the highest sensitivity according to the pressure. To confirm the effect of the magnetic field on the performance of the pressure sensor, the resistance change of the pressure sensor fabricated without the applied magnetic field was compared with that of the sensor fabricated with the magnetic field (Figure 2.11b). Even at the high filler concentration, the isotropic composite showed negligible change of resistance compared to the anisotropic composite because the number of current paths generated by the applied pressure is small. Accordingly, because the sensitivity is too low at the pressure range applied in daily activities, the isotropic composite is not suitable to be applied to the pressure sensor for realization of e-skin.

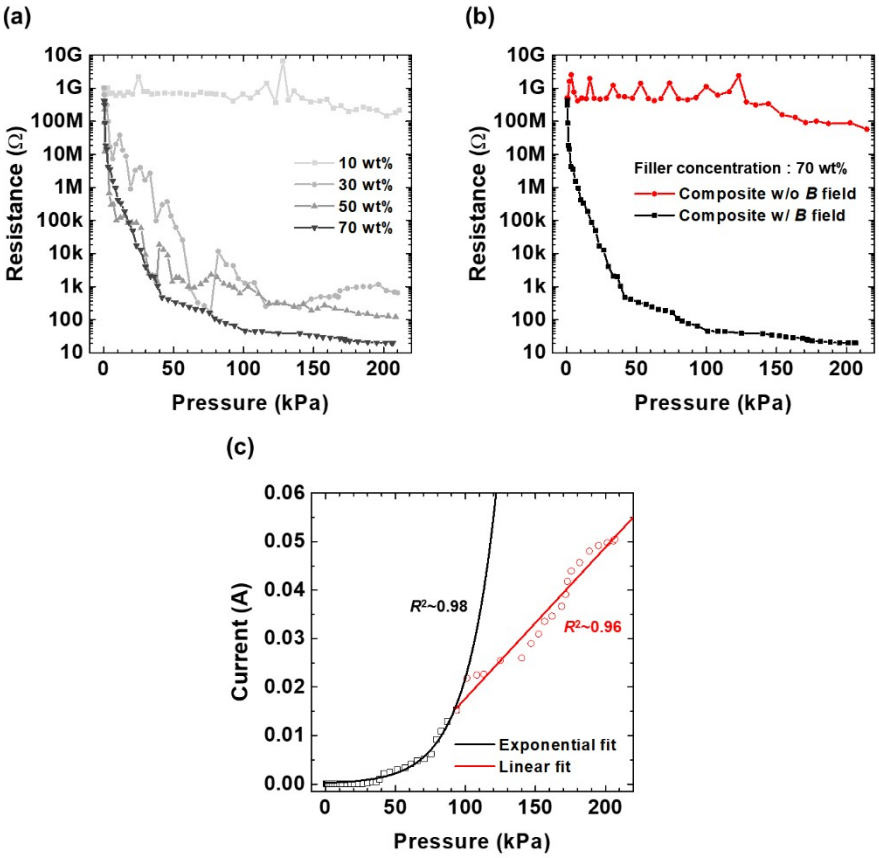

Figure 2.11 | Resistance-pressure characteristics of high-resolution pressure sensors. The resistance changes according to (a) the filler concentration and (b) application of the magnetic field at the fabrication process, when the pressure is applied. (c) The current-pressure graph with exponentially and linearly fitted curves at the different pressure range.

To analyze piezoresistive characteristics of the pressure sensor with anisotropic composite, the current-pressure curve is depicted in Figure 2.11c. If the tunneling effect through the insulating gaps between conductive fillers is dominant at the composite, the expected current change according to the applied pressure is

expressed as the exponential form. Assuming that all tunneling junctions between fillers are identical, the current change of the composite is given by[94]

$$I(P) = I_0 \exp\left(\frac{2\alpha dP}{3\beta}\right) \tag{3.4}$$

where P is the pressure, α is the tunneling exponent, d is the tunneling distance, and β is the bulk modulus. At the low pressure range (< 90 kPa), the current change of the anisotropic composite is fitted by the exponential curve (R^2 ~ 0.98). In other words, conduction through the inter-particle tunneling is dominant at the low pressure range because conduction paths through filamentous structures are not completely formed. On the other hand, at the high pressure range (> 90 kPa), the current change is approximated by the linear equation (R^2 ~ 0.96), which means that conduction is no longer dominated by the tunneling effect. The increased contact area between filamentous structures and the increased number of electrical connections between filaments have a major influence on the change of conductivity because the inter-particle distance is short enough to make conduction paths at the high pressure range. In this pressure range, the pressure sensor showed a remarkable sensitivity of higher than 10^5 kPa^{-1} because the amount of current change is much larger compared to the initial current value.

The graph of current changes when various pressures are applied to the sensor is shown in Figure 2.12a. The pressure sensor could distinguish various pressures of 1, 10, and 100 kPa due to the large difference in the current change. In addition, when the high pressure of 2.4 MPa was applied to the sensor by a sharp tip with a diameter of 300 μm, the sensor normally sensed the pressure. To check the

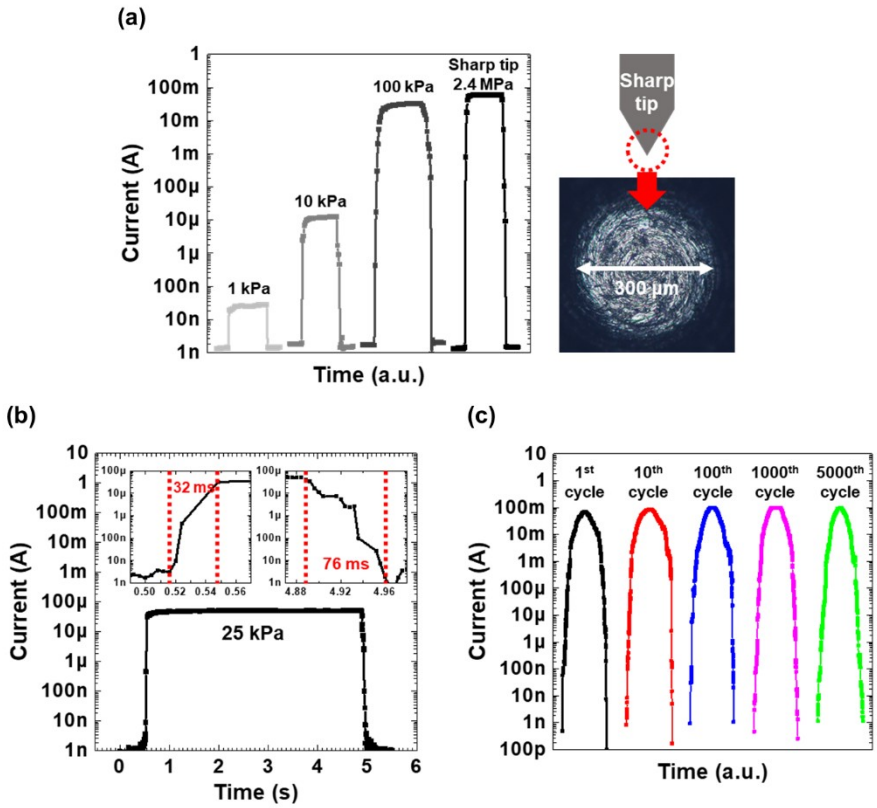

Figure 2.12 | Basic electrical characteristics of the high-resolution pressure sensor. (a) Current changes when various pressures are applied to the sensor. (b) Measurement of response and relaxation times of the sensor when the pressure of 25 kPa is applied. (c) The results of the cyclic pressing test with the pressure of 100 kPa. The current changes at the first, 10th, 100th, 1000th, and 5000th cycle are depicted.

response and relaxation time of the sensor due to the viscoelasticity of PDMS, a pressure of 25 kPa was loaded and unloaded at a high speed of 10 mm/min (Figure 2.12b). The response and relaxation time were measured as 32 ms and 76 ms, respectively, which is comparable to the human skin.[95] The cyclic pressing test was also conducted to assess the mechanical reliability of the sensor. Even after the

pressure of 100 kPa was repeatedly applied to the sensor for 5,000 times, the sensor operated stably maintaining its initial current-pressure characteristics.

2.3.3. Determination of Spatial Resolution of the Pressure Sensor

In order to confirm the spatial resolution of the pressure sensor, a two-point discrimination (2PD) test was carried out. The 2PD test is widely used in a clinic for assessing human tactile perception, especially the resolution of the tactile sense.[96] Calipers with two sharp tips are used to define the shortest length between two tips that the subject can feel the two distinct points (Figure 2.13a). Similarly, with two 100 μm-sized probe tips, the 2PD test of the pressure sensor was conducted with gradually decreasing the distance between two pressure-applied pixels (Figure 2.13b). As shown in Figure 2.13c, pressure sensor arrays were sandwiched between top and bottom electrodes. Top electrodes were fabricated by inkjet printing a silver

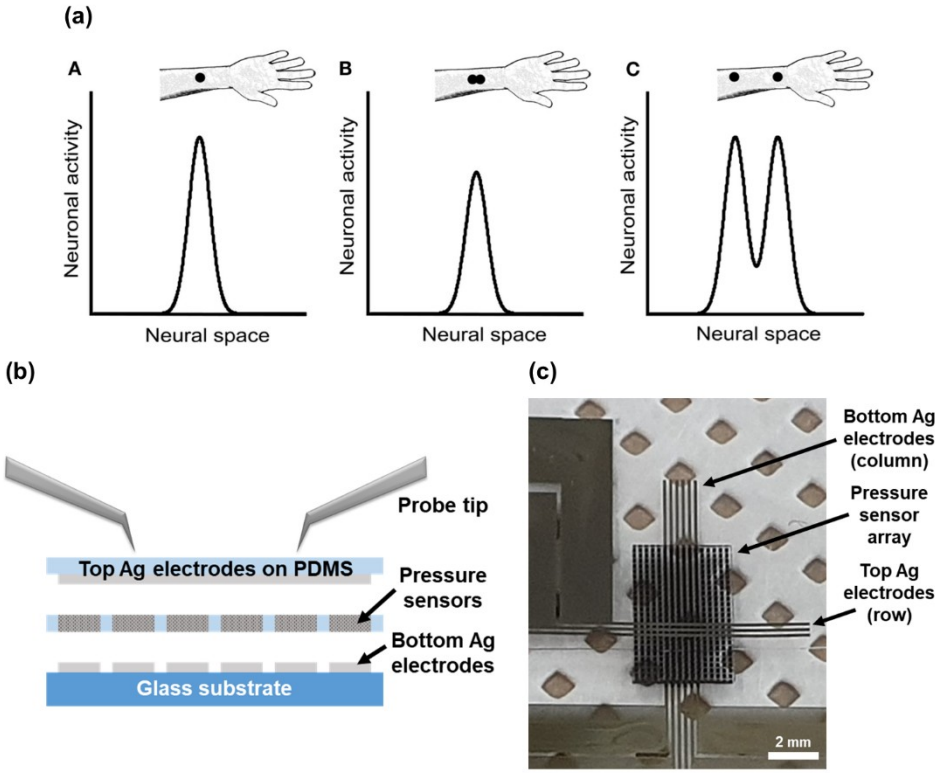

Figure 2.13 | Two-point discrimination test for determination of the spatial resolution. (a) Schematic illustrations of the 2PD test used in a clinic for assessing human tactile perception with calipers.[96] (b) Schematic image and (c) optical image of the pressure sensor arrays prepared for the 2PD test. The top substrate was fabricated with PDMS to ensure that the pressure can be transmitted to the sensor pixel.

ink on 100 μm-thick PDMS to ensure that the pressure can be transmitted to the sensor pixel. When the distance between two pixels pressed by probe tips decreased from 750 μm to 250 μm, the pressure sensor arrays could distinguish the pressed points without any severe crosstalk at the neighboring pixels (Figure 2.14). Therefore,

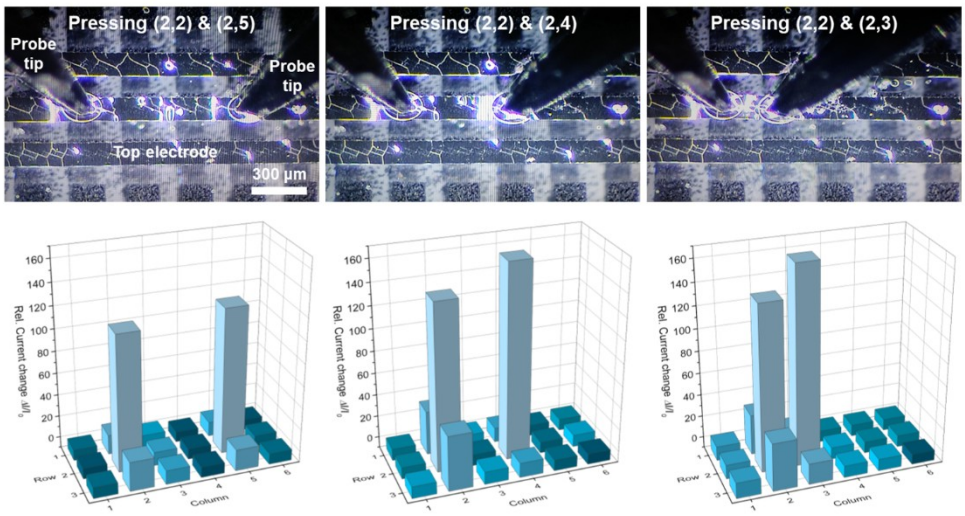

Figure 2.14 | Results of the 2PD test of high-resolution pressure sensor arrays. The relative current changes of each pixel are depicted for each case when the distance between two pixels pressed by probe tips decreased from 750 μm to 250 μm.

the spatial resolution of fabricated pressure sensor arrays could be determined as 100 ppi (250 μm-pitch).

On the other hand, when the 2PD test was carried out with the not-patterned composite that filamentous structures are uniformly distributed throughout the substrate, not-patterned pressure sensor arrays could not properly distinguish the two pressure-applied pixels (Figure 2.15a). This is because in the case of pressure sensor arrays with not-patterned composite, current changes occur in the pixels adjacent to the pressure-applied pixel due to the crossstalk effect. In order to determine the cause of crosstalk between pixels, the leakage current between the electrodes was measured while each sensor array (not-patterned sensors and patterned sensors with

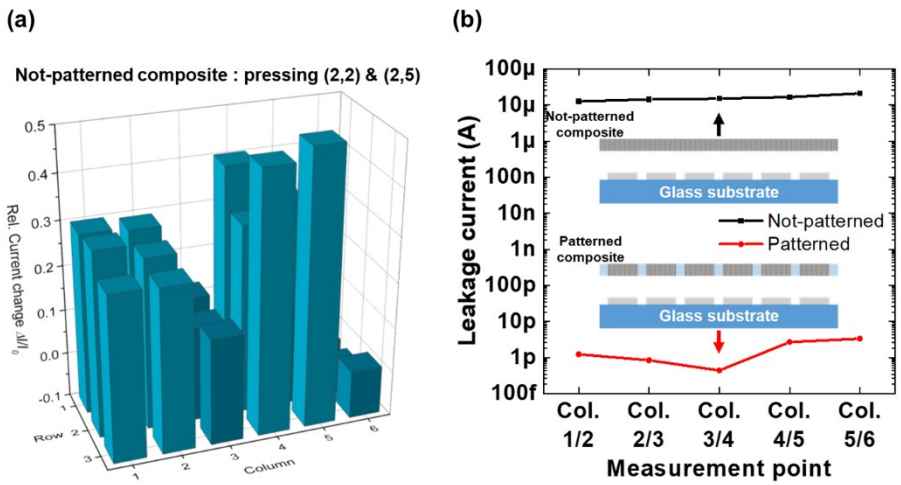

Figure 2.15 | Comparison of spatial resolution of pressure sensors according to the structure for isolation of the pixels. (a) The relative current changes of each pixel when two pixels of (2,2) and (2,5) were pressed with probe tips in the case of non-patterned composite. (b) The leakage current between two neighboring electrodes at not-patterned or high-resolution patterned composite.

the membrane) was laminated on the bottom electrodes. Pressure sensors fabricated with the perforated membrane showed negligible leakage current lower than 10 pA between two neighboring electrodes. In the case of the not-patterned composite, meanwhile, the leakage current was measured as about 10 μA (Figure 2.15b). This high leakage current induced crosstalk between neighboring pixels to obscure distinction between pristine and pressure-applied pixels. Therefore, the proposed method not only achieves structurally patterned pixels of the pressure sensor, but also guarantees orthogonality between pixels in operation of pressure sensor arrays.

2.3.4. Real-Time Pressure Mapping Applications

To examine the feasibility of proposed pressure sensor arrays to the e-skin applications, real-time pressure mapping system with readout circuits was demonstrated. The readout system (MC1600, Kitronyx) consists of multiplexers that can select between 48 columns and 48 rows, analog-to-digital converter (ADC) with 8-bit resolution, and a microcontroller unit (MCU) (Figure 2.16a). Analog signals of 2,304 pixels (48x48) with the resistance range of 0.05 - 12.75 kΩ were converted

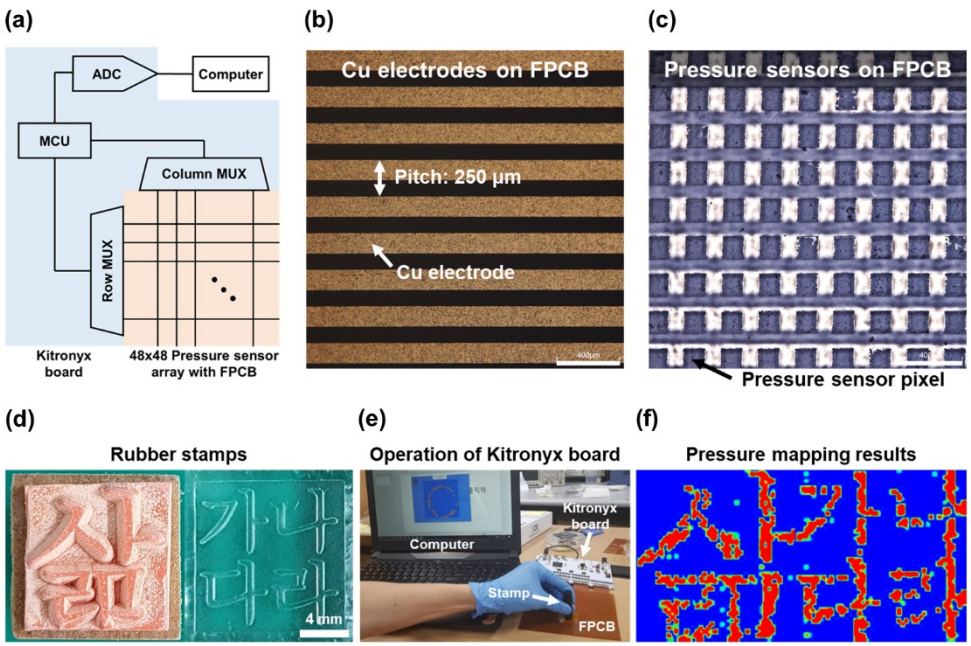

Figure 2.16 | Real-time pressure mapping of 2,304 pressure sensor pixels. (a) Schematic diagram of the readout system. Optical images of (b) Copper electrodes with the same resolution with the pressure sensor arrays on FPCB, (c) Pressure sensor arrays laminated on FPCB, and (d) rubber stamps used to apply the pressure with conformal contact. (e) Operation of the real-time pressure mapping system with a computer. (f) Results of pressure mapping in high resolution enough to recognize the font of the letters engraved on the stamps.

into 8-bit digital signals with a scan rate of 20 Hz. Copper electrodes on FPCB with the pitch of 250 μm (100 ppi) were used to make electrical connections between pressure sensor arrays and readout system (Figure 2.16b). By aligning pressure sensor arrays with top and bottom electrodes on FPCB, 48x48 sensor arrays with readout electrodes were achieved (Figure 2.16c).

Rubber stamps that were finely engraved with complex Korean letters were used to apply the pressure for the conformal contact between the stamp and pressure sensor arrays (Figure 2.16d). Pressure mapping of the rubber stamp was conducted in real-time using software on a computer connected to the readout system (Figure 2.16e). As shown in Figure 2.16f, the pressure mapping was successfully carried out

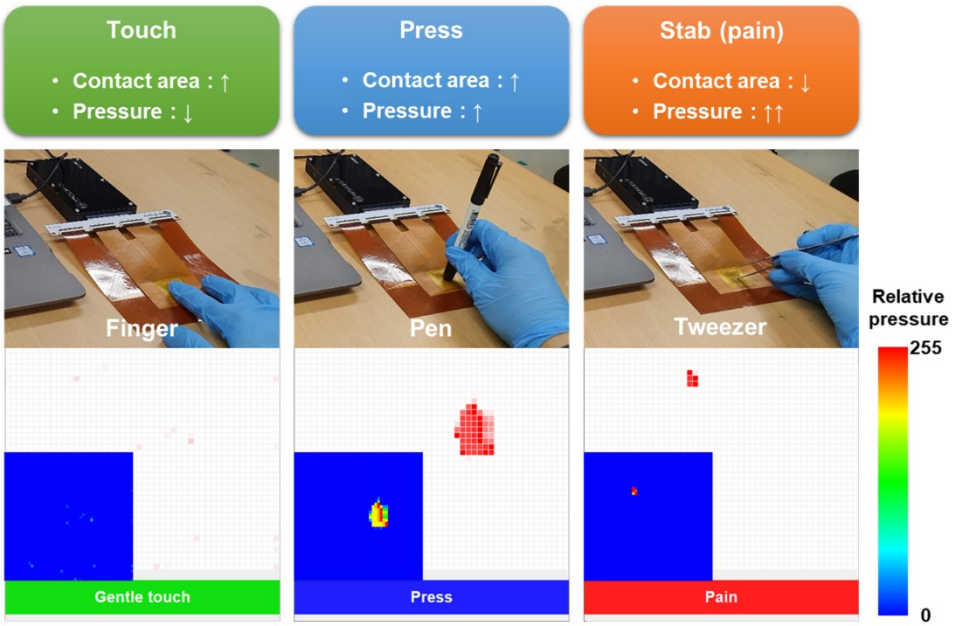

Figure 2.17 | Real-time categorization of applied pressure. Applied forces are categorized into three groups: touch, press, and stab, according to the pressure level and pressure-applied area with Python program.

in high resolution enough to recognize the font of the letters engraved on the stamp. In addition, real-time categorization of applied pressure was implemented using the readout system and Python program (Figure 2.17). Applied forces were categorized into three groups: touch, press, and stab, according to the pressure level and pressure-applied area. When forces were applied to the pressure sensor arrays with a finger, pen, and tweezer, the software automatically classified the pressure by a finger as a gentle touch; the pressure by a pen as press; and the pressure by a tweezer as stab. This demonstration of real-time mapping and categorization of applied forces shows the applicability of proposed pressure sensor to the e-skin that mimics a tactile sense of the human skin.

2.4. Conclusion

In summary, this chapter introduced soft pressure sensor arrays with high resolution up to 100 ppi that can cover the resolution of various types of human tactile sense patterned with the micro-perforated membrane. By applying the magnetic field to the ferromagnetic elastomer composite that shows piezoresistivity, sensitivity of the pressure sensor was highly enhanced with the anisotropic filamentous structure of ferromagnetic particles. Due to the use of ferromagnetic particles as the filler, pressure sensor arrays could be patterned with modulation of the magnetic field. However, when resolution of the modulator reached 50 ppi, ferromagnetic particles were not fully patterned due to reduced gradient of the magnetic flux density induced by the interference between pillar structures. Therefore, the patterning method utilizing perforated membrane as a frame was introduced to achieve resolution of 100 ppi that is the minimum limit of the human tactile receptor for sensing injurious forces. The patterned pressure sensor showed remarkable sensitivity of higher than 10^5 kPa^{-1} and great mechanical reliability that the sensor operated stably even after cyclic press of 5,000 times. At the 2PD test that determines the spatial resolution of the sensor, pressure sensor arrays could distinguish two pressed points with the minimum gap of 250 μm without any severe crosstalk with neighboring pixels. Real-time pressure mapping of 2,304 pixels was carried out using the computer-connected readout system. In addition, real-time categorization of applied forces according to the pressure level and pressure-applied area was implemented using Python program.

This demonstration of real-time mapping and categorization of applied forces shows the feasibility of proposed pressure sensor arrays to be applied to e-skin that mimics a tactile sense of the human skin.

Chapter 3. Soft Probe Unit for Inspection of Deformable Electronic Devices

3.1. Introduction

A probe unit is one of the most important electrical components for signal transferring or inspection process during or after the device is fabricated. For the electrical connections to the external equipment, physical contact between contact pads on the device and connectors to the inspection equipment has to be made. In the case of conventional rigid electronics, the direct physical contact to the electrodes does not affect the electrodes because the thickness of the electrode is set to be thick for low electrical resistance. However, in the case of devices fabricated on the deformable substrate, the thickness of each layer is significantly decreased to enhance the deformability and conformability. As shown in Figure 3.1a, the tensile strain is applied to the outer layer of the substrate when the device is bent. Because the bending strain induced by bending is proportional to the distance from the neutral plane, thickness of the device has to be thinner to alleviate the damage induced by the bent state.[97-100] In addition, in order to form a conformal contact on the uneven surface such as a human skin, the deformable substrate requires the reduced thickness as shown in Figure 3.1b.[101] Due to the thinner thickness introduced to enhance deformability and conformability of the device, the direct physical contact

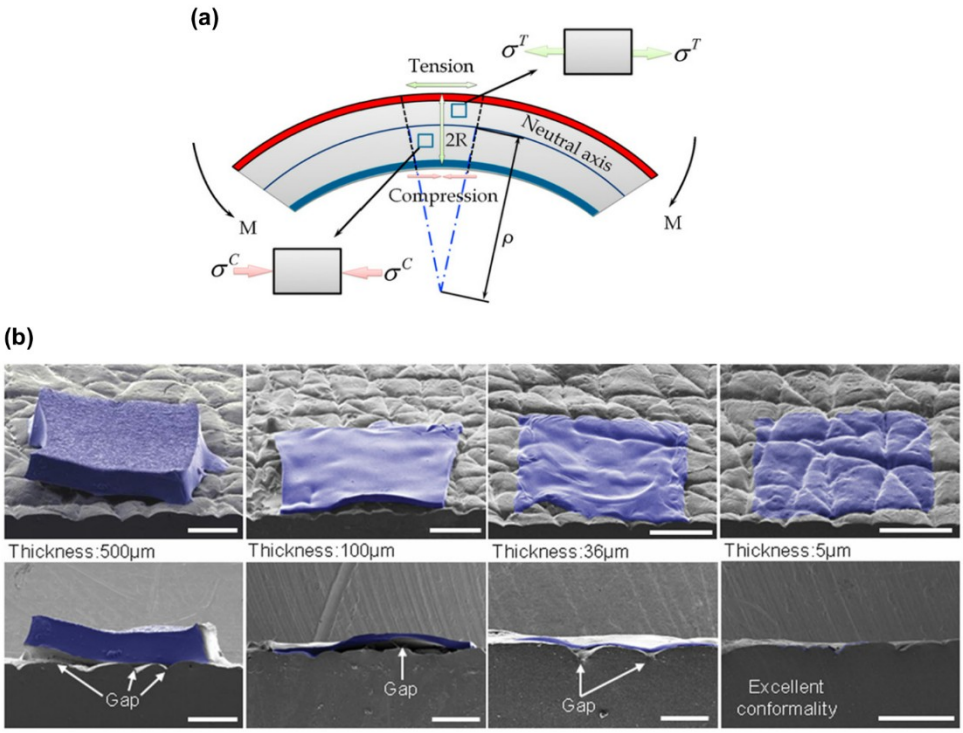

Figure 3.1 | Changes of bending strain and conformability according to the thickness of the deformable substrate. (a) Schematic illustration of the flexible substrate in the bent state. The tensile and compressive strain are applied to the outer and inner layer of the substrate.[98] (b) SEM images of the stretchable substrate (blue-colored) with different thickness laminated on the replica of human skin (grey-colored).[101]

with a rigid connector has the possibilities to generate the cracks on the surface. These cracks can be propagated to other parts under repeated deformation, which affects the mechanical reliability of the device.[29, 102, 103] To avoid this reliability issue, optical inspection methods are introduced to find defects in the device through the pattern analysis using an optical system without a physical connection to the device (Figure 3.2).[104-107] However, the optical inspection has a fundamental limitation of

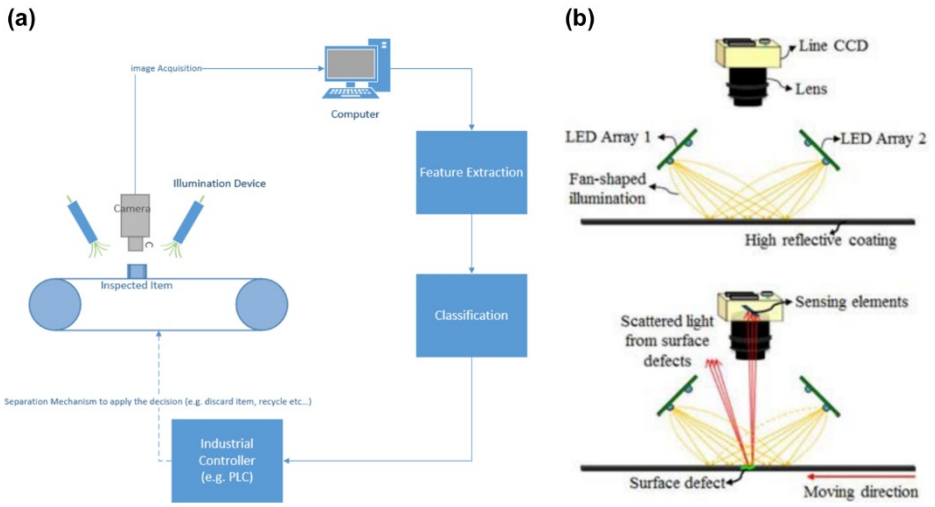

Figure 3.2 | Optical inspection method without a physical connection to the device. Examples of (a) fully automated optical inspection system and (b) optical inspection method to detect surface defects utilizing scattered light.[104, 107]

unavailability for verifying the normal operation of the device. In other words, to analyze the various characteristics of the device, the physical connection is required for the electrical measurements.

In addition to the softness of the probe unit, high resolution is needed due to the increased device density caused by miniaturization of devices to be applied to wearable electronics. There have been many researches on the probe unit with high resolution fabricated using the micro-electromechanical systems (MEMS) process. In order to reduce the mechanical stress on the contact pads during the physical contact, various types of structures such as a cantilever,[108] blade,[109] bump,[110] and spring[111] are applied to the probe unit (Figure 3.3). Despite the specially designed structures, since the part in contact with the thin electrode of the device is a rigid

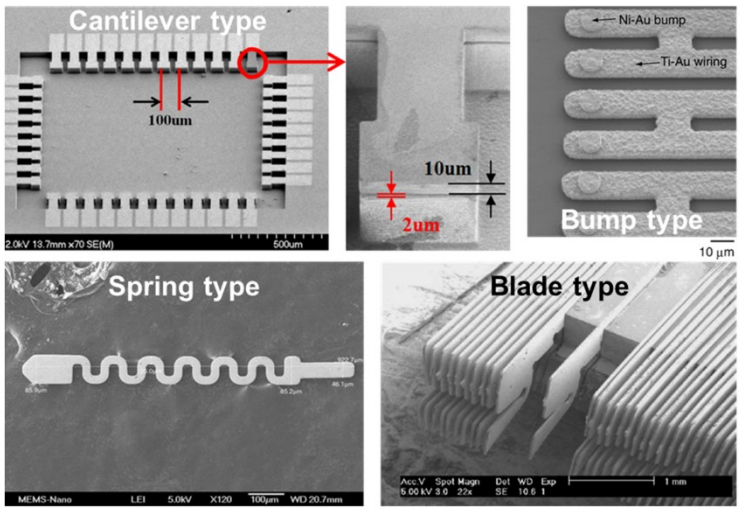

Figure 3.3 | Various types of probe unit fabricated by the MEMS process for high-resolution applications. Shock-absorbing structures, including cantilever,[108] bump,[109] spring,[110] and blade,[111] were applied to reduce the mechanical stress on the contact pads.

metal, damage such as cracks or scrape is inevitable when the excessive pressure is applied. Accordingly, it is necessary to develop a soft probe unit (SPU) that can form electrical connections without damage to deformable and highly integrated devices for wearable electronics.

In this chapter, the soft probe unit with the conductive elastomer composite patterned by the perforated membrane is introduced. The SPU acts as a conductive buffer layer that prevents damage to the electrodes on deformable electronic devices caused by the physical contact for the electrical connections. For the highly enhanced conductivity of the composite, silver-coated iron particles were introduced to the composite with the magnetic field. The micro-perforated membrane was utilized for

patterning the composite to prevent the lateral current flow due to the connections between filamentous structures at the high filler concentration. Fabricated SPU with high resolution of 500 ppi showed low contact resistance and protective properties when applied to the inkjet-printed electrodes on the flexible substrate. In addition, in the case of the electrical contact between electrodes with a fine pitch of 50 μm, any crosstalk through the SPU did not occur due to the patterned morphology. The feasibility of proposed SPU to the practical usage was confirmed with the application to the commercial FPCB connector for inspection process and electrodes for solution-processed polymer LED (PLED). When the SPU-bonded FPCB was used as a connector between the flexible display panel and inspection device, inspection operations such as color switching were performed normally. In addition, due to the conformal contact between the cathode and functional layer of PLED induced by the insertion of SPU, uniform light emission was conducted at the crossover of the anode and cathode.

3.2. Experimental Section

3.2.1. Materials

Poly(dimethylsiloxane) (PDMS) was purchased from Dow Corning Corp. (Sylgard 184) and mixed with a curing agent at an appropriate ratio before use. Trichloro(1H,1H,2H,2H-perfluorooctyl)silane (FOTS) (Sigma-Aldrich) was used as an anti-adhesion agent that makes cured PDMS delaminate from the carrier substrate with ease. (3-aminopropyl)triethoxysilane (APTES) (Sigma-Aldrich) was used to introduce silanol groups to the plastic substrate for formation of irreversible siloxane bonds with the activated PDMS layer. Silver nano-particle (AgNP) ink (DGP 40LT-15C, ANP Co., Ltd.) was used to fabricate electrodes with an inkjet printer for measurement of electrical and mechanical characteristics of the SPU. Poly(ethylene 2,6-naphthalate) (PEN) film with a thickness of 125 μm was purchased from DuPont Teijin Films (Teonex Q65HA) and used as a substrate of electrodes. Ferromagnetic silver-coated iron (Ag-Fe) particles with a mean size of 4.5 μm (Conduct-O-Fil SI03P40, Potters Industries LLC.) were mixed with PDMS at the desired concentration to form the conductive elastomer composite. Silver epoxy (LOCTITE ABLESTIK CE 3103WLV, Henkel Corp.) and 50 μm-thick copper wire (Nilaco Corp.) were used to make electrical connections between electrodes and the source measure unit.

3.2.2. Fabrication Process

PDMS Mold for Replication Process: During the fabrication process of micro-perforated membranes with PDMS, a replication method that PDMS replicates the structure of the mold was used. First of all, a 4-inch silicon wafer as a master mold was etched using a deep silicon etcher to achieve hole arrays with a diameter, spacing, and depth of 20 μm, 30 μm and 100 μm, respectively. For the surface treatment of an anti-adhesion agent, the wafer was treated with the air-plasma at 100 W for 1 min (Cute-MPR, Femto Science) and left with FOTS solution in a desiccator connected with a vacuum pump overnight. After PDMS was mixed with a curing agent with a ratio of 10:1 using a paste mixer (ARE-310, Thinky) and poured over the mold, the mold was placed in a vacuum desiccator to remove air bubbles in hole arrays. The curing process of PDMS was conducted at 100 °C for 1 h. Cured PDMS layer was detached from the master mold to obtain the PDMS mold with pillar structures.

Micro-Perforated PDMS Membrane: The PDMS mold was put on the glass substrate to be used as a mold for the second replication process. The anti-adhesion treatment of the PDMS mold with FOTS was conducted similarly to the silicon master mold. After un-cured PDMS was poured on the PDMS mold and all bubbles were removed by the vacuum desiccator, spin-coating was conducted to expose the top side of pillars at the PDMS mold by removing excess un-cured PDMS on the pillars. After the curing process at 100 °C for 1 h, the micro-perforated PDMS membrane was carefully detached from the PDMS mold using tweezers.

Soft Probe Unit with Patterned Elastomer Composite: The perforated membrane fabricated using the replication process was laminated to the PEN-attached glass carrier substrate. Spacers having the same thickness as the membrane were attached to prevent the membrane from distortion due to the pressure caused by the magnetic force between a pair of magnets. The mixture of 60 wt% Ag-Fe particles in PDMS was poured on the membrane. To make the mixture fill the holes at the membrane, the sample was placed in the vacuum desiccator until all air bubbles were removed. After the air bubbles were entirely eliminated using the vacuum desiccator, the blade-coating was conducted to remove excess Ag-Fe particles and PDMS on the membrane. The top side of the sample was covered with the PEN-attached glass substrate to prevent the composite from protruding when the magnetic field is applied. A pair of samarium-cobalt permanent magnets were placed at the top and bottom sides of the sample to apply the uniform magnetic field. The sample was left for 10 min to give enough time for rearrangement of Ag-Fe particles in the magnetic field. After the sample was cured at 100 °C for 1 h with a pair of magnets attached to it, the PEN film was peeled off from the PDMS layer.

Electrodes for measurement of electrical and mechanical characteristics of SPU: For the hydrophilic surface of PEN to achieve good wetting of AgNP ink, the PEN substrate was treated with UV/O_3 for 10 min. Inkjet printing of AgNP ink was conducted with a drop-on-demand inkjet printer (Dimatix 2831, Fujifilm Dimatix Inc.) at the platen temperature of 60 °C. In the case of the electrodes with a fine pitch and width, the AgNP ink was printed using an electrohydrodynamic (EHD) printer

(SIJ-050, SIJ technology, Inc.). For evaporation of residual solvents and sintering of AgNPs, the substrate was annealed at 150 °C for 1 h on the hot plate.

Irreversible bonding of SPU to FPCB: For the hydrophilic surface to achieve good wetting of the APTES solution, the FPCB was treated with UV/O_3 for 10 min. After the treatment, the APTES solution of 2 wt% in deionized (DI) water was drop-cast on the FPCB. The FPCB was thoroughly cleaned with DI water and blown with a N_2 gun to remove excess APTES on the surface after 10 min. The FPCB was annealed at 100 °C for 30 min on the hot plate to eliminate the residual water. After the APTES-treated FPCB and SPU were treated with the air-plasma at 100 W for 1 min, the SPU was laminated on the FPCB to form irreversible siloxane bonding by the physical contact.

3.2.3. Characterization

Basic electrical characteristics of the elastomer composite and SPU were measured using a Keithley 2400 SourceMeter (Tektronix, Inc.). For measurement of the resistivity of the composite, the composite was sandwiched between top and bottom aluminum electrodes with a width of 1 cm. For measurement of the sheet resistance of the composite, a custom-made four-point probe with a spacing of 1 mm between each probe was used. To measure the resistance of the SPU pixel and electrodes with a fine pitch, a semiconductor parameter analyzer (Agilent 4155C, Agilent Technologies Inc.) connected to the probe station with the fine probe tip with the diameter of 10 μm was used.

The pressure was applied and measured with a digital force gauge (DTG-1, Digitech Co., Ltd.) installed on an automatic test stand (ASM-1000, Digitech Co., Ltd.). A force gauge tip with a diameter of 7 mm was used to apply the force to the SPU at the speed of 1 mm/min. The applied tensile stress to the PDMS composite according to the tensile strain was measured using a universal testing machine (UTM) (Instron 5543, Instron) at a 100 mm/min speed.

Optical images of the composite and SPU were obtained with an optical microscope (DSC510, Olympus). A field emission scanning electron microscope (FE-SEM) (S-4800, Hitachi) was used to capture the images of PDMS mold, membrane, and cross section of the SPU. The thickness and morphology of fabricated membranes were measured by a surface profiler (DektakXT-A, Bruker) with a stylus force of 1 mg to prevent deformation of elastomer due to the applied force.

3.3. Results and Discussion

3.3.1. Applicability of Elastomer Composite to the Soft Probe Unit

The composite of elastomer and conductive particle shows the characteristics of softness of elastomer and conductivity of filler simultaneously. Therefore, the conductive elastomer is suitable for the SPU that can suppress the damage on the contact pad due to the physical contact for the electrical connection. Because high filler concentration is needed to achieve the high conductivity of the composite, stress-strain characteristics of the composite with high filler concentration of 60 wt% were measured to confirm that the composite retains softness of the elastomer. As shown in Figure 3.4, Young's modulus increased about two times in both cases of

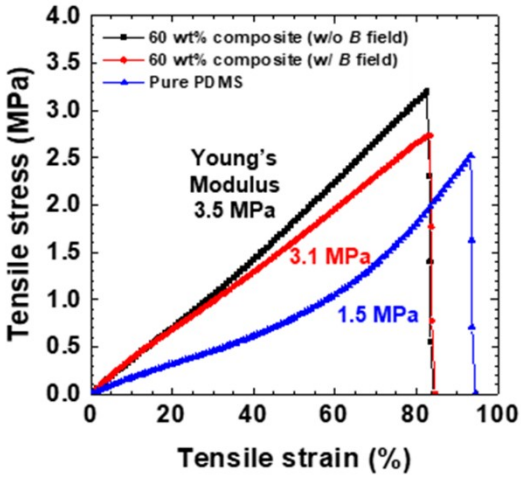

Figure 3.4 | Stress-strain characteristics of pure PDMS and ferromagnetic composite. The width, length, and thickness of the measured samples were 10 mm, 30 mm, and 0.5 mm, respectively.

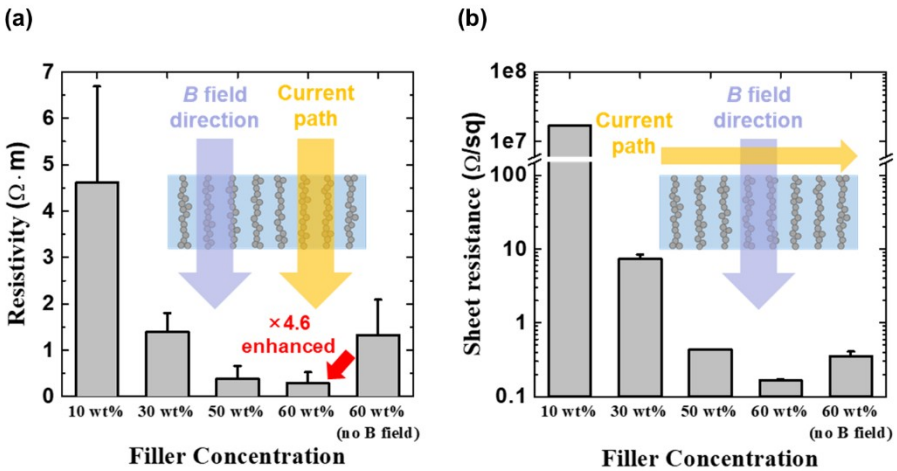

Figure 3.5 | Changes of electrical characteristics of the composite according to the filler concentration. (a) Changes of resistivity when the resistance of the composite was measured by applying the current in the same direction as the magnetic field. (b) Changes of sheet resistance when the resistance was measured by applying the current perpendicular to the direction of the magnetic field.

composites compared to that of pure PDMS due to the rigid metal filler. In spite of the high filler concentration, composites showed a high fracture strain of 83%, which means that the composite still retains elastomeric characteristics of the elastomer.

Changes of the resistivity and sheet resistance according to the filler concentration and the applied magnetic field are shown in Figure 3.5. In the case of measurement of resistivity, the resistance of the composite was measured by applying the current in the same direction as the magnetic field (Figure 3.5a). The composite of silver-coated iron fillers showed conductivity without the applied pressure even at the low filler concentration because the silver is less oxidized

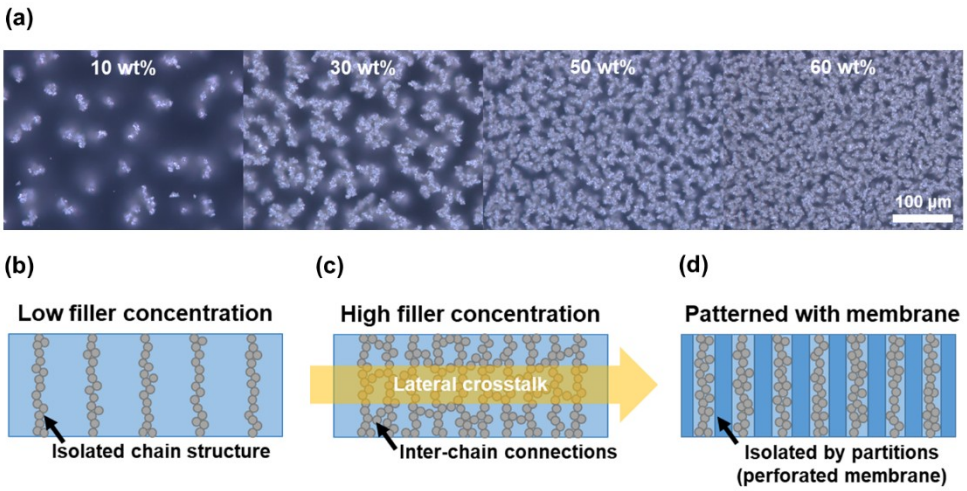

Figure 3.6 | Changes of 3D structures of ferromagnetic filler according to the filler concentration. (a) Surface images of the composite with different filler concentration. Schematic illustrations of cross-sectional images with (b) low filler concentration, (c) high filler concentration, and (d) partition structure for isolated filamentous structures.

compared to the nickel that was used to fabricate the pressure sensor in Chapter 2. The resistivity of composites decreased as the filler concentration increased because more filamentous structures were formed as shown in the optical images of composites in Figure 3.6a. In addition, compared to the composite fabricated without the magnetic field, the composite fabricated with the magnetic field showed enhanced conductivity about 4.6 times.

Different from measurement of the resistivity, the measurement of sheet resistance was conducted by applying the current perpendicular to the direction of the magnetic field (Figure 3.5b). At the low filler concentration such as 10 wt%, the current cannot flow through the horizontal direction because conductive filamentous

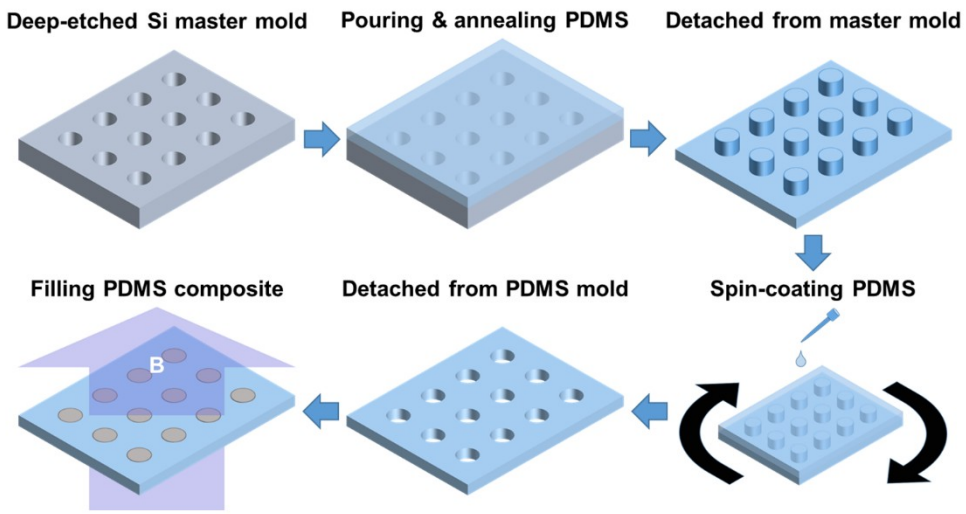

Figure 3.7 | Fabrication process of the soft probe unit using the replication method. During the process, Silicon and PDMS molds were treated with FOTS for formation of the anti-adhesion layer.

structures are isolated (Figure 3.6b). As the filler concentration increases, the closer distance between chain structures induces inter-chain connections. Due to the inter-chain connections, the sheet resistance of composites decreased as the filler concentration increased. Therefore, in order to introduce the composite to the SPU applications, the filler concentration of the composite must be high because the conductivity of the composite is enhanced at the high filler concentration while maintaining its elastomeric characteristics. However, as shown in Figure 3.6c, short circuit between contact pads can be caused by the lateral crosstalk when the composite is applied to the SPU. To prevent the flow of current through the horizontal direction, the patterning method using the perforated membrane as a

frame was introduced (Figure 3.6d). By this patterning method, the SPU without the crosstalk phenomenon could be achieved while maintaining the high conductivity.

3.3.2. Replication Method for Elastomer Membrane to Pattern the Composite

The fabrication process of the SPU with the micro-perforated membrane and anisotropic elastomer composite is depicted as the schematic illustration in Figure 3.7. To obtain the perforated PDMS membrane, a replication method that PDMS replicates the structure of the mold was used. Repeated hole patterns for the perforated membrane were engraved on a silicon wafer (master mold) using a deep-etching process. As an anti-adhesion agent between the silicon master mold and PDMS, FOTS was treated at the master mold using the vapor deposition method.[70, 112] After the liquid PDMS was poured on the FOTS-treated master mold and fully cured, PDMS with periodic pillar structures (second mold) was detached from the master mold, as shown in SEM images in Figure 3.8. By varying the design of the deep-etched silicon master mold, pillar structures with various resolution from 100 dpi to 500 dpi were successfully fabricated. As the second mold for the membrane, PDMS pillar arrays were also treated with FOTS.

For replication of the second mold to form through-hole structures with the same diameter of the pillar of the second mold, spin-coating was conducted to remove the excess PDMS on the pillars after PDMS was poured on the second mold.[113] As shown in the surface profiles and optical images in Figure 3.9,

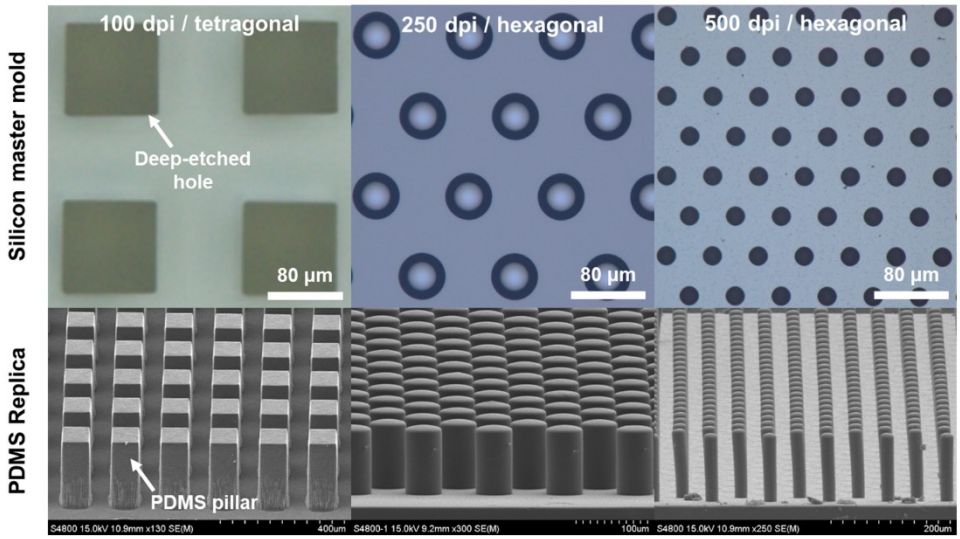

Figure 3.8 | Optical and SEM images of silicon master molds and PDMS replicas.

optimization of spin-coating speed was needed to achieve a uniform thickness of the membrane and open holes. The thickness and morphology of fabricated membranes were measured by a surface profiler according to the spin-coating speed. When the spin-coating speed was too low, the through-holes could not be obtained because the excess PDMS remained on the pillars and closed the holes. On the other hand, when the spin-coating speed was too high, PDMS stuck in the pillar arrays was pulled out at the spin-coating process, resulting in the non-uniform morphology of the perforated membrane. Only by the optimized spin-coating speed, the perforated membrane with the uniform thickness could be fabricated. The SPU was fabricated with a composite of PDMS and ferromagnetic particles by filling the through-holes of the perforated membrane with the composite (Figure 3.10a). Ferromagnetic particles with the core-shell structure (silver-coated iron particles) were used as

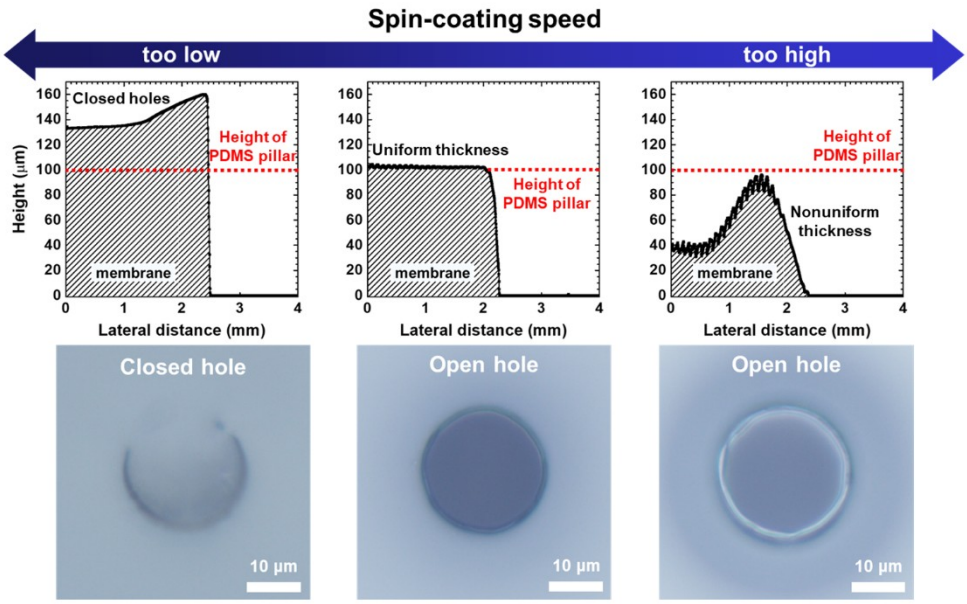

Figure 3.9 | Optimization of spin-coating speed for the micro-perforated membrane with the uniform thickness. To precisely control the morphology of the membrane, the spin-coating speed was split into the interval of 100 rpm.

fillers due to the high conductivity of silver. After the composite was injected into the PDMS hole arrays, the magnetic field was applied to the membrane in the vertical direction. This magnetic field induced the alignment of ferromagnetic fillers according to the direction of the magnetic field, forming filamentous structures (Figure 3.10b). After the curing process, the SPU with the pixel diameter of 20 μm and gap between pixels of 30 μm was fabricated.

3.3.3. Electrical Characteristics of the Soft Probe Unit

In order to figure out whether the fabricated SPU can act as a conductive buffer layer that prevents damage to the electrode, the resistance was measured while the SPU was inserted between two electrodes fabricated on the plastic substrate (Figure 3.11). To form the conformal contact between SPU and electrodes for the low contact resistance, the pressure must be applied to the contact point. When the applied pressure was too low, the SPU-inserted contact showed relatively high resistance compared to the direct contact without the SPU due to the contact resistance between SPU and electrodes as shown in Figure 3.11a. However, when the moderate pressure of about 40 kPa was applied, the difference between the resistance of the SPU-

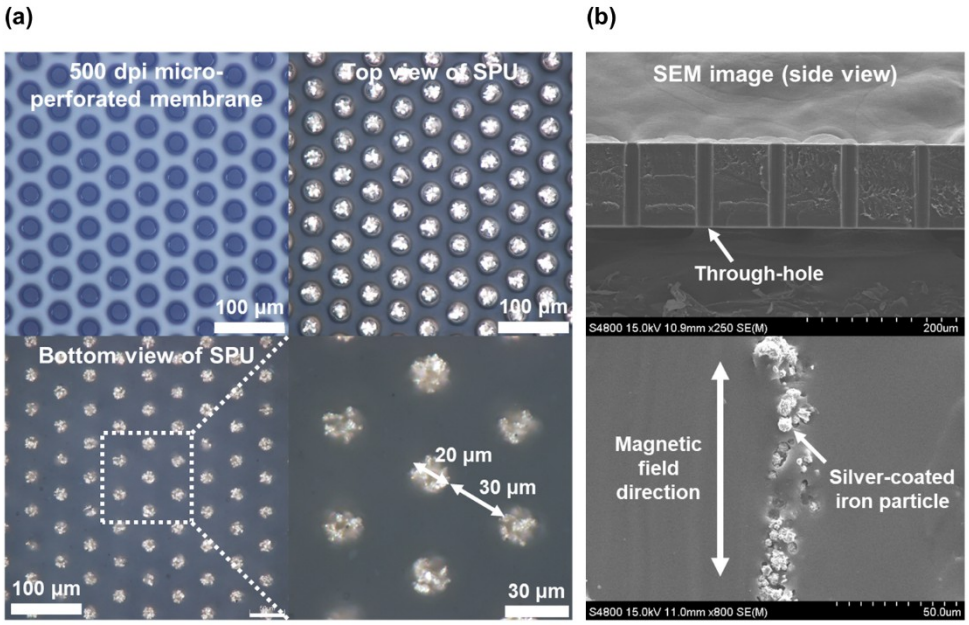

Figure 3.10 | Optical and SEM images of the perforated membrane and SPU. (a) Top and bottom side images of the membrane and SPU. (b) Cross-sectional images of the membrane with through-holes and ferromagnetic composite.

inserted contact and that of the direct contact was less than 0.05 Ω. Therefore, it can be seen that the introduction of SPU does not significantly affect the contact resistance between electrodes as long as an appropriate pressure is applied during contact.

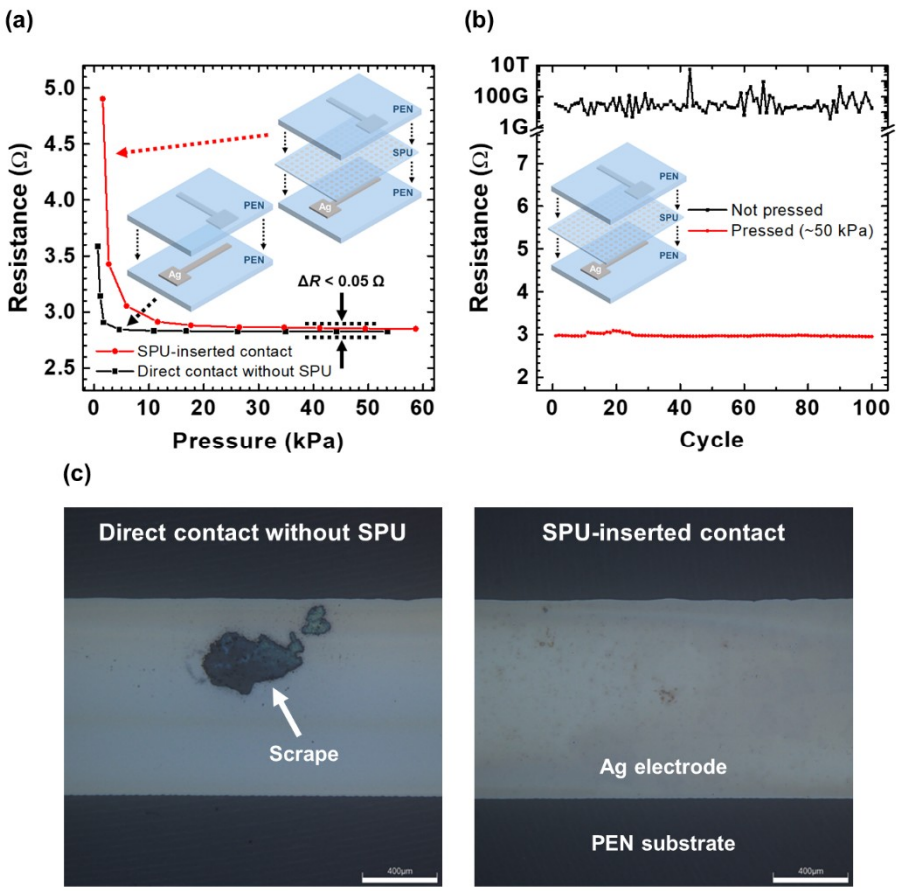

Figure 3.11 | Electrical and protective characteristics of the SPU. (a) Changes of resistance between two flexible electrodes with SPU-inserted contact and direct contact without SPU according to the applied pressure. (b) The cyclic pressing test of SPU-inserted contact with the pressure of 50 kPa. (c) Optical images of the electrode on the flexible substrate after the repeated pressure was applied for 100 cycles.

The cyclic pressing test was conducted to confirm that the SPU can prevent damage to the electrode by acting as a shock absorber (Figure 3.11b). The pressure of 50 kPa was repeatedly applied to the SPU-inserted electrodes by the force gauge combined with the automatic test stand. After 100 cycles of pressing, the resistance of the SPU-inserted contact changed only 0.6%. Optical images of electrodes after the cyclic pressing test with and without SPU are shown in Figure 3.11c. In the case of direct contact without SPU, the scrape was generated on the region in contact with the other electrode. On the other hand, in the case of SPU-inserted contact, there was no noticeable damage to the surface of the electrode. There results show that the proposed SPU can be used as a conductive buffer layer that is inserted between electrodes to prevent damage caused by physical contact with rigid metal.

To confirm that the SPU patterned using the membrane can be applied to form electrical connections at contact pads with fine pitch, the resistance of each SPU pixel was measured (Figure 3.12). As shown at the inset illustration, the SPU was laminated on the highly conductive aluminum electrode fabricated with the vacuum evaporation to ignore the resistance of the electrode. The fine probe tip with the diameter of 10 μm was used to make contact with the SPU pixel with the diameter of 20 μm as shown in the optical image. The average conductivity of eight SPU pixels is 5.5 S/m, which is much lower than that of pure metal due to the limitation of elastomer composite. Nevertheless, since the thickness of the SPU is as thin as 100 μm, the effect of SPU on the entire resistance is insignificant when the SPU is inserted as a buffer layer.

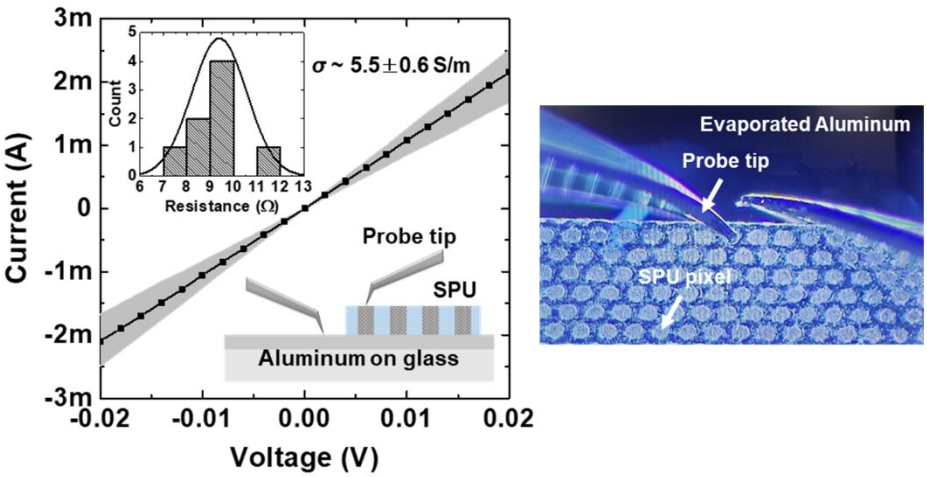

Figure 3.12 | Measured resistance of one SPU pixel. The inset graph depicts the resistance distribution of eight pixels. The right image shows the measurement setup with the fine probe tip with the diameter of 10 μm.

In addition to the measurement of resistance of each pixel, the SPU was employed to the contact between electrodes with a fine pitch of 50 μm (Figure 3.13). Two bottom electrodes with a width and gap of 15 μm and 35 μm were inkjet-printed on the PEN substrate using a EHD printer. After the SPU was laminated on the bottom substrate, the top electrode with a width of 15 μm was aligned with the SPU. The measured current-voltage characteristics were depicted in Figure 3.13a. The resistance was measured at three types of contact: direct contact without the SPU, SPU-inserted contact, and SPU-only contact without the top electrode. When the SPU was inserted between top and bottom electrodes, the resistance increased about 40 Ω due to addition of two SPU pixels to the current path. When the top electrode was not in contact with the SPU laminated on the bottom electrodes, there was no current flow between two bottom electrodes. This result implies that the crosstalk

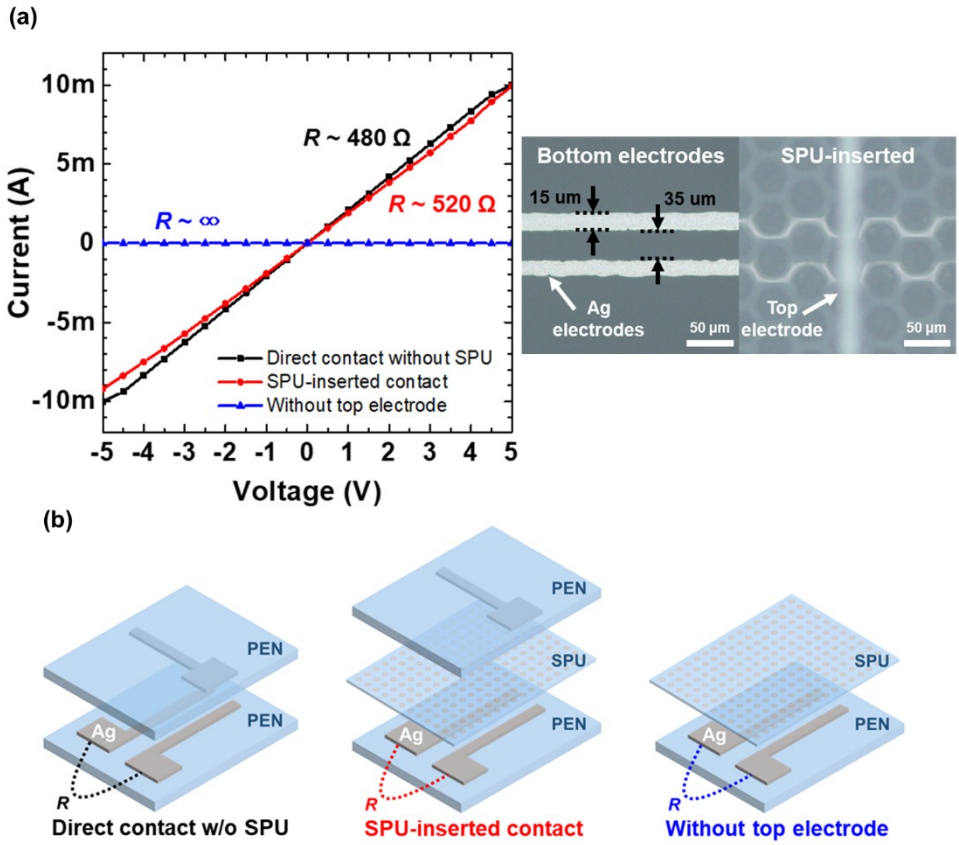

Figure 3.13 | Measured resistance of the SPU-inserted contact between fine-pitch electrodes. (a) Measured resistance in three cases. Electrodes with a width and gap of 15 μm and 35 μm were used. (b) Schematic illustrations of three different contact conditions. To figure out the leakage current through the SPU, the resistance between neighboring electrodes was measured without the top electrode.

does not occur at the electrodes with a gap greater than 20 μm because the SPU pixel is isolated to a size of 20 μm with a perforated membrane.

3.3.4. Application of SPU to the Inspection Process of Deformable Display

To verify the applicability of the SPU to the FPCB that is generally used as a connector, two FPCBs with sockets that are used to align the contact pads on FPCBs were fabricated (Figure 3.14a). The width and gap of copper electrodes on FPCBs are 50 μm and 150 μm, respectively. The siloxane bonding (-Si-O-Si-) method was introduced to bond the SPU made of PDMS to the FPCB made of PI without disturbance of the current flow.[28] The APTES solution was coated on the surface of FPCB to form silanol groups (-Si-OH) for siloxane bonds. With the air-plasma treatment, the activated silanol groups on the PI layer can form the chemical bonding

(a)

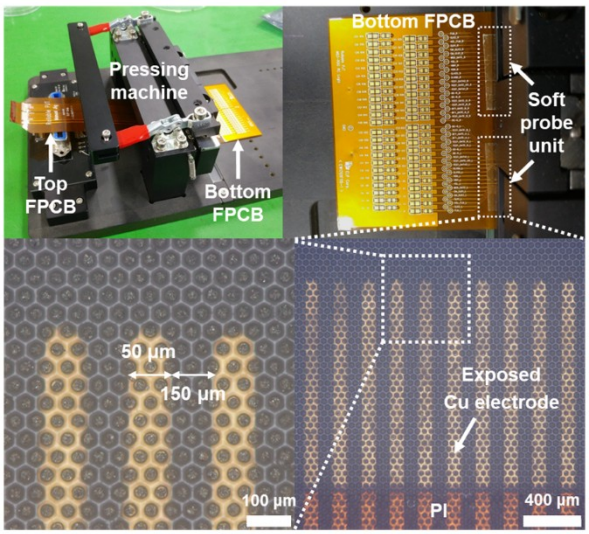

(b)

Contact pad number	Resistance w/o SPU (Ω)	Resistance w/ SPU (Ω)	Calculated resistance of SPU (Ω)
1	0.5	0.5	0.0
2	0.5	0.5	0.0
3	1.0	1.1	0.1
4	1.1	1.0	-0.1
5	0.9	1.1	0.2
6	1.0	1.1	0.1
7	1.0	0.9	-0.1
8	1.0	1.2	0.2
9	1.0	1.0	0.0
10	0.9	1.1	0.2
11	1.0	1.1	0.1
12	1.0	1.1	0.1
13	1.0	1.1	0.1
14	1.0	1.1	0.1
15	1.0	1.4	0.4
16	0.9	1.1	0.2
17	1.0	1.1	0.1
18	1.2	1.0	-0.2
19	0.9	1.0	0.1
20	1.0	1.1	0.1
21	1.0	1.4	0.4
Average			0.10 Ω
Stdev.			0.14 Ω

Figure 3.14 | Application of the SPU to electrodes on the commercial FPCB. (a) Optical images of setup for measuring the resistance of SPU-inserted contact between two FPCBs. (b) Measured resistance between two FPCBs at 21 contact pads.

with the activated PDMS layer. After the APTES-treated FPCB and SPU were treated with the air-plasma at 100 W for 1 min, the SPU was laminated on the FPCB to form irreversible siloxane bonding by the physical contact. The top FPCB was aligned with the bottom FPCB using the sockets on FPCBs and the pressure was applied to the crossover to form conformal contact by the custom-made pressing machine. When the resistance between two FPCBs was measured from 21 contact pads, the average resistance of SPU calculated from the resistance of SPU-inserted contact and direct contact without SPU was only 0.1 Ω (Figure 3.14b).

The graph in Figure 3.15a shows the measured resistance of the FPCB used as a connector of the display panel and inspection device. Similar to the aforementioned results, there was not much difference in resistance between the case of SPU-inserted contact and direct contact without SPU. On the other hand, in the case of the composite that was not patterned with the perforated membrane, the contact resistance increased because the filler concentration was lowered to eliminate the lateral crosstalk as shown in Figure 3.5b. Two types of FPCB connectors with the SPU and not-patterned composite were applied to inspection of the flexible display panel. The contact between the SPU-bonded FPCB and display panel was conducted using the pressing machine (Figure 3.15b). When the SPU-bonded FPCB was used as a connector between the display panel and inspection device, inspection operations such as color switching were performed normally (Figure 3.15c). In the case of the not-patterned composite, meanwhile, abnormal

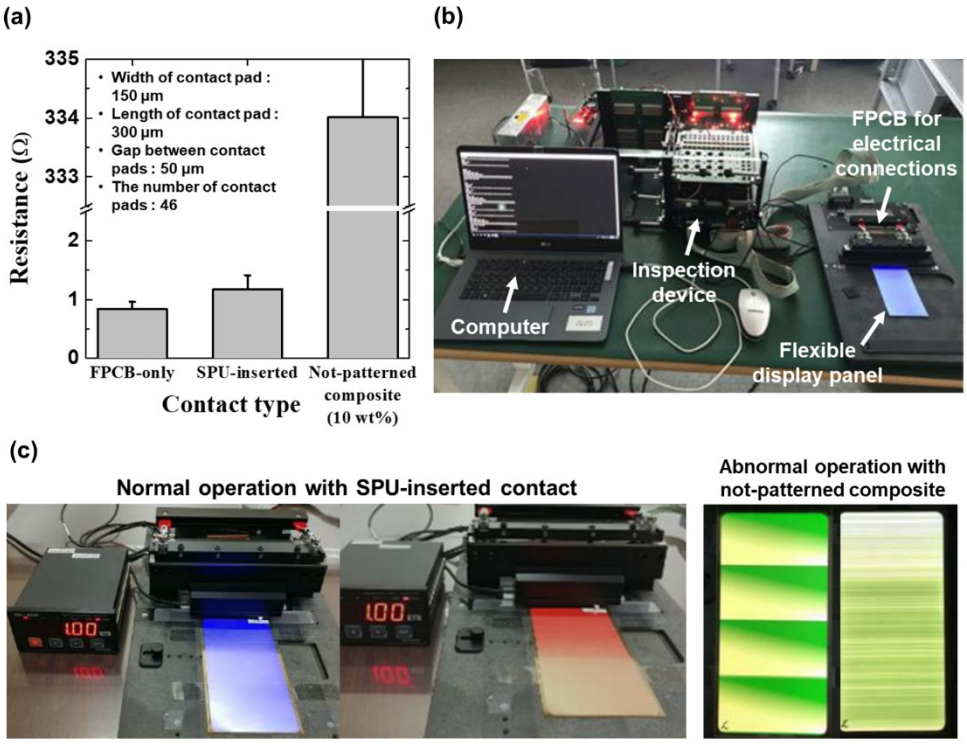

Figure 3.15 | Inspection of the flexible display panel using the SPU. (a) Changes of contact resistance between two FPCBs according to the contact type. (b) Image of setup for inspection of the display panel with the SPU-bonded FPCB connector. (c) Results of the color switching test of the display panel when the SPU and not-patterned composite were applied to the connector.

operations occurred because the inspection signal was not applied properly due to the high contact resistance.

In order to confirm the possibilities of the SPU to be applied to the inspection of the PLED, the SPU was introduced to the cathode of the PLED device. The PLED with stacked functional layers of electron injection layer (EIL), emission layer (EML), and hole injection layer (HIL) was fabricated by the solution process

(Figure 3.16a). Each layer was formed with spin-coating on the pre-patterned ITO anode/glass substrate. The SPU was laminated on the AgNW cathode using a plasma treatment to compose the stacked structure as shown in Figure 3.16b. Due to the conformal contact between EIL and cathode induced by the insertion of SPU, the PLED operated normally that the device emitted the light at the crossover of the anode and cathode (Figure 3.16c). In addition to introduction to the connector of the inspection device of the display panel, application to the cathode of the PLED for device operation shows the feasibility of our approach not only to the inspection in the device level, but also to the inspection in the pixel level of the deformable display.

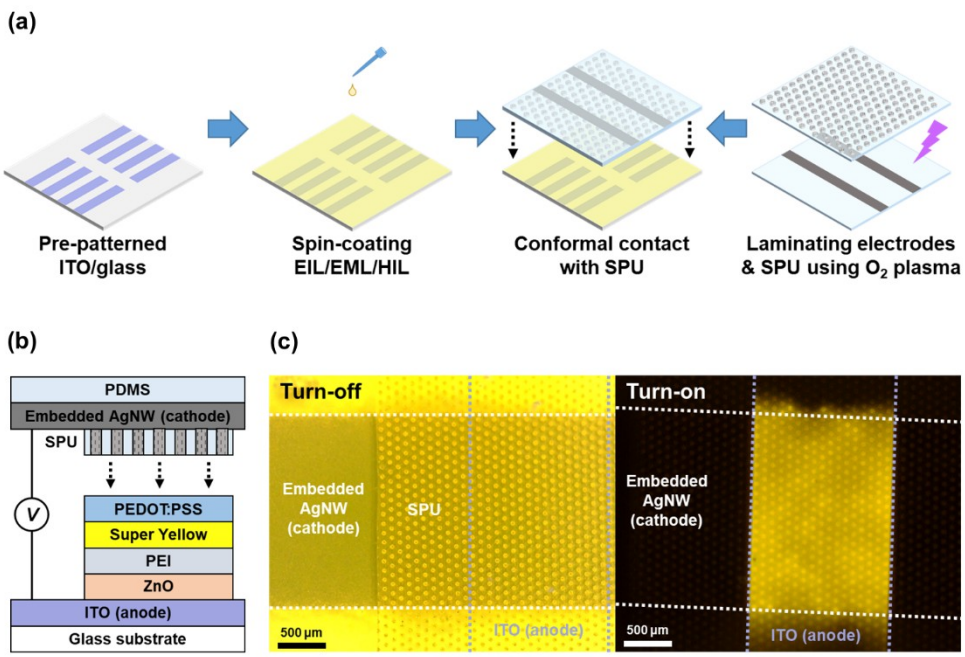

Figure 3.16 | Application of the SPU to the electrode of solution-processed PLED. (a) Fabrication process of solution-processed PLED and SPU-bonded cathode. (b) Schematic diagram of the PLED structure. (c) Results of operation of PLED when the SPU-bonded cathode was laminated on the PLED.

3.4. Conclusion

In summary, this chapter introduced the soft probe unit as a conductive buffer layer that prevents damage to the electrodes on deformable electronic devices caused by the physical contact for the electrical connections. Elastomeric characteristics of the composite of elastomer and ferromagnetic particles with high filler concentration was confirmed by the stress-strain measurement. By introducing highly conductive ferromagnetic particles with the core-shell structure, conductive elastomer composite that showed conductivity without the applied pressure even at the low filler concentration was achieved with magnetically induced filamentous structures. The filler with high concentration that is needed to enhance the conductivity of the composite induces the lateral current flow by the connections between the filamentous structures, resulting in the possibilities of crosstalk between contact pads. The soft probe unit with high conductivity and no crosstalk was achieved by implementation of patterning method using the micro-perforated membrane. By utilizing the PDMS replication process for the PDMS mold and optimized spin-coating process, the SPU with high resolution up to 500 ppi was successfully fabricated. When the SPU was applied to the inkjet-printed silver electrodes on the plastic substrate, the resistance changed only 0.6% after 100 times of repetitive pressing. In addition, the SPU acted as a shock-absorbing layer that prevents generation of scrape on the surface of the electrode. Because the SPU pixel was isolated to a size of 20 μm with a perforated membrane, short circuit between

neighboring electrodes with a gap of 35 μm did not occur when the contact of electrodes with fine pitch was carried out. When the SPU was bonded to the FPCB that was generally used as a connector to the inspection device by using an irreversible siloxane bonding method, the increase of contact resistance induced by insertion of the SPU was low as 0.1 Ω. In contrast to the case of not-patterned composite, inspection operations of flexible display panel such as color switching were performed normally when the SPU was applied to the FPCB connector of the inspection device. In addition, the solution-processed PLED could operate with the SPU-laminated cathode due to the conformal contact between the functional layer and cathode induced by the insertion of SPU. This demonstration of inspection of devices using the SPU shows the feasibility of proposed probe unit to be applied to the inspection process of the deformable display to prevent damages on the devices.

Chapter 4. Stretchable Vertical Interconnect Access for Multi-Layered Circuits

4.1. Introduction

Stretchable electronics have been widely studied in the single level devices, including electrodes,[22, 114, 115] sensors,[29, 48] thin-film transistors,[116, 117] and light-emitting diodes,[40, 53, 118] to improve the device performance and stretchability. Nevertheless, there are still challenges in integrating these low-level unit devices to realize high-level multifunctional systems due to difficulties in arranging devices in high density and making electrical connections between each component. To address the challenges encountered in realizing stretchable systems at the planar structure, the introduction of vertical interconnect access (VIA) is necessary (Figure 4.1). The VIA technology allows overcoming limitations on the device density at the two-dimensional (2D) scheme by extending the circuit design to the three-dimensional (3D) structures. In the case of conventional printed circuit boards (PCBs), holes are made with drilling and plated with metals to form conduction paths between desired layers. Formation of VIAs at the elastomeric substrate using mechanical drilling, meanwhile, is not a simple process because the elastomer is easily deformed by the external force to induce misalignment of drilling or damage to the devices on the substrate. In addition, due to the good chemical resistance of the elastomer such as

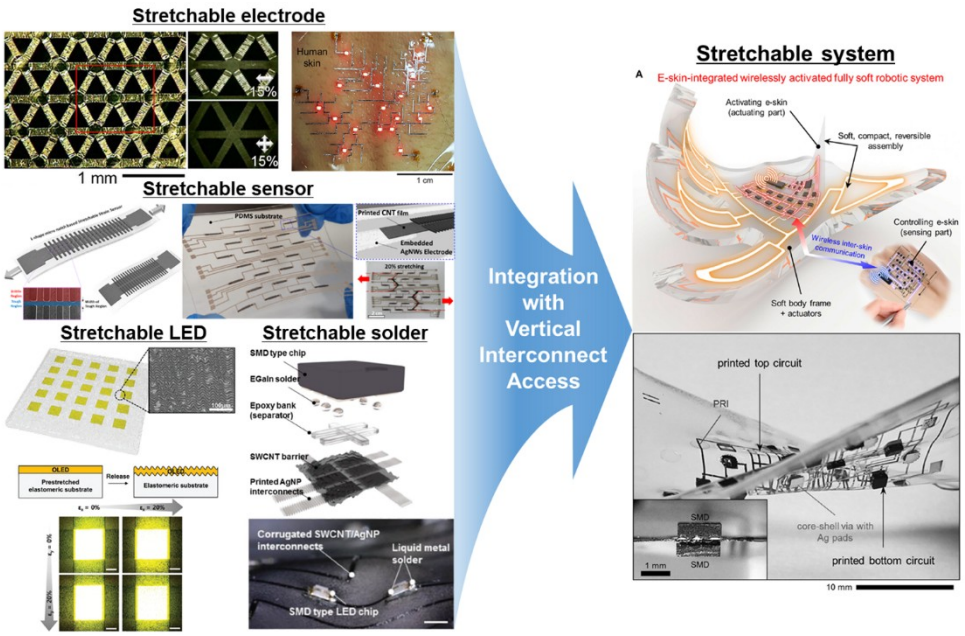

Figure 4.1 | VIA for realization of stretchable system integrating single-level devices. Various single-level stretchable devices have been studied including the electrode,[15] sensor,[29] LED,[40] and solder[18] for the integrated system.[8, 16]

PDMS, removal of the elastomer at desired positions with a chemical etching is also a formidable task.[119]

Recently, researchers have investigated various unique strategies for forming VIAs at the stretchable substrate, including patterning of polyimide (PI) at the serpentine metal/PI electrodes;[42, 120, 121] injection of a metal ink into a textile substrate;[122] direct 3D printing of metals;[123, 124] drilling holes using a laser and filling metal or liquid metal;[125-127] and filling a liquid metal at the microfluidic channel.[128] In the case of using rigid metals as VIAs and electrodes, the stretchability of the entire system can be limited depending on the density of VIAs and electrodes. In

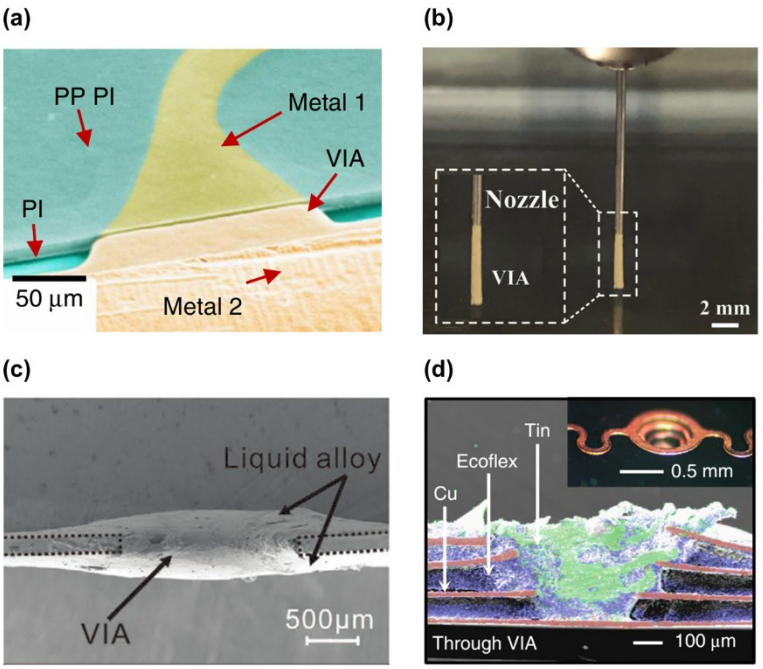

Figure 4.2 | Examples of VIA implemented on the stretchable substrate. (a) Patterning of polyimide (PI) at the serpentine metal/PI electrodes.[120] (b) Direct 3D printing of metal.[124] Drilling holes using a laser and filling (c) liquid metal,[127] or (d) metal.[125]

addition, concentrated mechanical stress at the interface between rigid metals and the elastomeric substrate can affect the mechanical reliability of the entire system. Direct 3D printing or injection methods have limitations on selection of materials for the substrate and electrodes. The laser ablation method takes longer than the other methods because a laser must scan each point one-by-one to drill a hole for the VIA. In the case of using liquid metals, elaborate encapsulation is required to prevent leakage of liquid metals while maintaining electrical connections with other components. Figure 4.2 and Table 4.1 summarize the aforementioned examples of

VIAs implemented on the stretchable substrate. Previously in our group, magnetically self-assembled modulus-gradient core-shell structures were proposed for highly stretchable VIA applications.[16, 17] However, the complex pre-stretching process of the elastomer substrate before the deposition of electrodes was needed to impart stretchability to brittle electrodes by forming wrinkles on the substrate. In addition, it was not compatible with the bottom-up process for the fabrication of multi-layered circuits exceeding the double-sided structure. Although many strategies have been developed to realize VIAs at the stretchable platform as described above, analysis of redistributed strain on the substrate induced by VIAs was rarely performed. Therefore, optimization of the structure of VIA for strain engineering and development of a facile process free from encountered problems during integration with other components are needed to realize multi-layered stretchable electronic systems.

In this chapter, a micro-structured anisotropic elastomer composite-based VIA utilizing magnetically aligned ferromagnetic particles and a perforated elastomer membrane is reported. By the applied magnetic field, ferromagnetic particles in the elastomer matrix form filamentous structures along the direction of the magnetic field to drastically lower the electrical resistance of the composite.[17, 56, 129, 130] Micro-structured composites, split into regularly arranged small VIAs by using the perforated membrane with through-holes as a frame, effectively disperse the mechanical stress to the elastomeric substrate under the stretched state, which can be confirmed by the finite element analysis (FEA) results and digital image correlation (DIC) analysis on strain distribution. In accordance with the results of strain analysis,

the micro-structured VIA shows enhanced mechanical reliability at the cyclic stretching test compared to the single VIA. By combining an automated patterning system with a bottom-up process for multi-layered structures, various types of VIAs used at commercialized PCBs are implemented on the stretchable substrate with four layers. Finally, to show the feasibility of proposed approach to the multi-layered stretchable electronics applications, stretchable passive matrix LED arrays operating stably under crumpled or biaxially stretched states are successfully demonstrated.

Table 4.1 | Summary of VIAs implemented on stretchable substrates

Reference	VIA material	Phase	Substrate	VIA patterning method	Electrode patterning method	Number of layers	VIA diameter (mm)	VIA thickness (µm)	Maximum strain	Cyclic stretching test
[127]	Liquid metal	Liquid	PDMS	Laser + spraying	Selective sticking of liquid metal	3	~ 0.7	~ 250	97%	1500 cycles @ 50%
[125]	Sn paste	Solid	Ecoflex	Laser + screen printing	Photolithography (Cu/PI)	10	0.045	100	100%	N/A
[120]	Cu/PI bilayer	Solid	Ecoflex	Photolithography	Photolithography	2	0.05	20	260%	N/A
[121]	Au/PI bilayer	Solid	Dragon skin	Photolithography	Photolithography	4	~ 0.2	1.5	30% (biaxial)	N/A
[122]	Ag flake/PVDF-HFP composite	Solid	PU nanofiber textile	Injection using a needle	Inkjet printing	2	~ 1.6	300	N/A	N/A
[123]	Field's metal/epoxy (core-shell)	Solid (low m.p.)	PDMS	EHD printing	EHD printing	2	~ 0.2	~ 1000	40%	100 cycles @ 10%
[124]	Ag paste	Solid	PDMS	3D printing	3D printing	3	N/A	2000	50%	1000 cycles @ 40%
[16]	Ni/PDMS composite	Solid	PDMS	Dispensing + magnetic alignment	Inkjet printing (Ag nanoparticle)	2	2	300	~ 90%	5000 cycles @ 50%
This work	Silver-coated-iron/PDMS composite	Solid	PDMS	Dispensing + perforated membrane	Monolithically embedded AgNWs	4	0.4 - 1.5	100	100%	1000 cycles @ 50%

4.2. Experimental Section

4.2.1. Materials

Poly(dimethylsiloxane) (PDMS) was purchased from Dow Corning Corp. (Sylgard 184) and mixed with a curing agent at an appropriate ratio before use. Trichloro(1H,1H,2H,2H-perfluorooctyl)silane (FOTS) (Sigma-Aldrich) was used as an anti-adhesion agent that makes cured PDMS delaminate from the carrier substrate with ease. Silver nanowires (AgNWs) with a diameter of 100 nm (10 mg/mL dispersed in ethanol, Yurui Chemical Co., Ltd.) were used as stretchable electrodes embedded in PDMS. Poly(ethylene 2,6-naphthalate) (PEN) film with a thickness of 125 μm was purchased from DuPont Teijin Films (Teonex Q65HA) and used as a carrier substrate for spray-coated AgNWs. Ferromagnetic silver-coated iron (Ag-Fe) particles with a mean size of 4.5 μm (Conduct-O-Fil SI03P40, Potters Industries LLC.) were mixed with PDMS at the desired concentration to form the conductive elastomer composite. Silver epoxy (LOCTITE ABLESTIK CE 3103WLV, Henkel Corp.) and 50 μm-thick copper wire (Nilaco Corp.) were used to make electrical connections between electrodes and the source measure unit. Pure and silver epoxy (LOCTITE ABLESTIK DX20C and 84-1LMISR4, Henkel Corp.) were used to attach SMD LED chips to the elastomer substrate and make electrical connections between LED chips and AgNW contact pads, respectively.

4.2.2. Fabrication Process

Base Layer with AgNW Electrodes for Multi-Layered Structure: In order to fabricate a bottom PDMS layer with stretchable electrodes, the AgNW-spray-coated carrier substrate was prepared. First, PDMS was spin-coated on the PEN substrate at 1000 rpm for 1 min. After PDMS was fully cured at 100 °C for 1h, the vapor deposition of FOTS was conducted as the same procedure described above. The AgNW solution was spray-coated on the PDMS layer through the metal mask for the desired pattern using a spray-coater (eNano, Enjet Corp.) at the stage temperature of 100 °C. The AgNW-spray-coated substrate was annealed at 100 °C for 30 min to fully evaporate the remaining solvent. At the embedding process of AgNWs in PDMS, to fabricate a PDMS layer with the desired thickness, spacers with an intended thickness were formed with Kapton tape on the FOTS-treated glass substrate. After PDMS was poured on the glass substrate, the substrate was covered with the AgNW-spray-coated PDMS/PEN film. The curing process at 100 °C for 1 h was followed by peeling off the PDMS/PEN film from the AgNW-embedded PDMS layer.

Multi-layered Circuits Utilizing Micro-Structured VIAs: The micro-perforated PDMS membrane was fabricated using the replication method mentioned in Chapter 3. To stack up the second layer on the bottom AgNW-embedded PDMS layer, the PDMS membrane was bonded using the air-plasma treatment. After both the bottom PDMS layer and membrane were treated with air-plasma at 100 W for 1 min, the membrane was laminated on the point where VIAs had to be formed. Spacers having the same thickness as the membrane were attached to make other parts where the

membrane was not bonded have the same thickness as the VIA region. For forming VIAs, the mixture of 60 wt% Ag-Fe particles in PDMS was patterned on the PDMS membrane using a pneumatic dispensing system (Shot mini 200SX, Musashi Engineering). To make the patterned mixture fill the holes at the membrane, the sample was placed in the vacuum desiccator until all air bubbles were removed. Then, pure PDMS was poured on the whole region including the parts where the membrane was not bonded. After the air bubbles were entirely eliminated using the vacuum desiccator, the blade-coating was conducted to remove excess Ag-Fe particles and PDMS on the membrane. The top side of the sample was covered with the AgNW-spray-coated PDMS/PEN substrate to achieve the embedding of AgNWs and the formation of VIAs simultaneously. A pair of samarium-cobalt permanent magnets were placed at the top and bottom sides of the sample to apply the uniform magnetic field. The sample was left for 10 min to give enough time for rearrangement of Ag-Fe particles in the magnetic field. After the sample was cured at 100 °C for 1 h with a pair of magnets attached to it, the PDMS/PEN film was peeled off from the PDMS layer. By repeating the process described above, the multi-layered structure including stretchable electrodes and VIAs could be fabricated.

Stretchable LED Arrays: The substrate, including two layers of AgNW electrodes and one layer of micro-structured VIAs, was prepared as described above. As a soldering material, silver epoxy was printed on AgNW contact pads using a dispensing system to make electrical connections between SMD LED chips and electrodes. Pure epoxy was printed between two contact pads of a LED chip to strongly bond the chip to the substrate and prevent a short circuit due to the spread

of silver epoxy. SMD LED (SML-P11UT, Rohm Co., Ltd.) chips were placed using an automated pick-and-place machine (TM220A; Hangzhou NeoDen Technology Co., Ltd.) at the desired positions. The curing process of silver and pure epoxy proceeded at 170 °C for 1 h. Electrical connections to the source measure unit used for driving LEDs were formed using copper wire and silver epoxy.

4.2.3. Characterization

All electrical measurements for electrical characteristics of the micro-structured VIAs were conducted using a Keithley 2400 SourceMeter (Tektronix, Inc.). For 4-wire measurement, a probe station with four probe positioners connected to the source measure unit was used. For the passive matrix addressing of 3x3 LED arrays, driving LEDs at each row with the current of 0.1 mA was conducted using a switching system (Keithley 3706a, Tektronix, Inc.) at intervals of 5 ms.

The stretching tests were performed with a custom-made automatic 1D stretching equipment at a speed of 100-200 mm/min. To obtain optical images of speckle patterns on the VIAs for the DIC analysis, a custom-made manual 1D stretching equipment was used to stretch the substrate to the desired length.

Optical images of VIAs were obtained with an optical microscope (DSC510, Olympus). A field emission scanning electron microscope (FE-SEM) (S-4800, Hitachi) was used to capture the images of PDMS mold, membrane, and AgNW networks.

4.3. Results and Discussion

4.3.1. Site-Selective Formation of Micro-Structured VIA for Multi-Layered Structure

The fabrication process of multi-layered circuits containing VIAs with the micro-perforated membrane and anisotropic elastomer composite is depicted as the schematic illustration in Figure 4.3. To obtain the perforated PDMS membrane, the replication method aforementioned in Chapter 3 was used. Different from the SPU where the conductive composite is patterned at regular intervals on the entire substrate, VIA has to be site-selectively patterned to make electrical connections only between the desired nodes in the electric circuit. A pneumatic dispensing system is used to pattern the highly viscous elastomer composite with the high filler concentration. As shown in Figure 4.4, by decreasing the pressure and dispensing time, the composite could be patterned to the size of 500 μm. After all patterns of the composite was formed at the desired points of the membrane, filling the remained through-holes with the pure PDMS was conducted to obtain the flat substrate.

To realize the intrinsically stretchable electronics for which the complex fabrication process such as pre-stretching of the substrate or formation of serpentine-shaped electrodes is not required, intrinsically stretchable electrodes are also needed in addition to the stretchable VIA. Silver nanowire (AgNW) is selected as a material for stretchable electrodes due to its intrinsic stretchability when embedded in

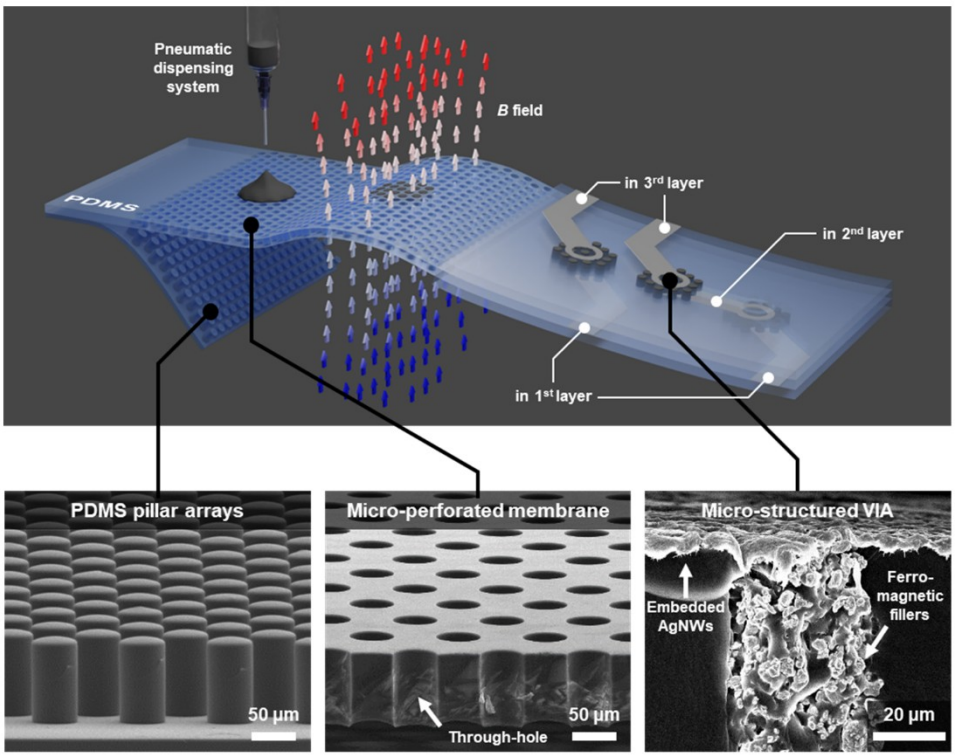

Figure 4.3 | Schematic illustration of the fabrication process of multi-layered stretchable circuits with micro-structured VIAs. Bottom SEM images show the cross-sectional images of PDMS mold, membrane, and micro-structured VIA with the AgNW electrode.

PDMS.[28] When the liquid PDMS is poured on the AgNW-spray-coated PEN substrate and cured, the random network of AgNWs embedded in PDMS is easily delaminated from the PEN substrate due to the weak adhesion force between the substrate and AgNW. By utilizing this embedding technique of AgNW in PDMS, formation of embedded AgNW electrodes could be carried out with the fabrication of VIAs simultaneously. After the membrane where the composite and PDMS are filled in the all through-holes is covered by the AgNW-spray-coated PEN substrate

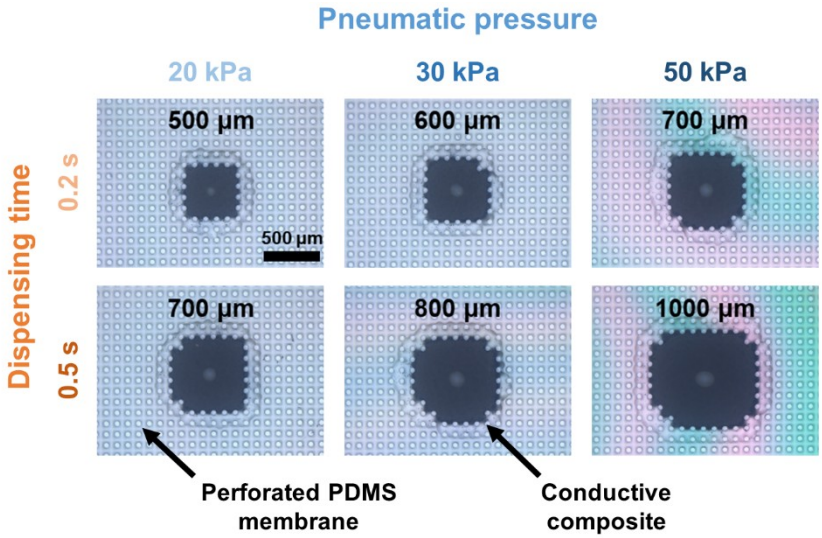

Figure 4.4 | Changes of patterned size of the composite according to the pneumatic pressure and dispensing time. The composite was printed on the perforated membrane using a pneumatic dispenser.

before the curing step of VIAs, micro-structured VIAs with embedded AgNW-electrodes could be achieved as shown in the SEM image of Figure 4.3. By stacking up the fabricated substrate including the VIAs and electrodes, stretchable circuits with multi-layered structures could be implemented.

4.3.2. Optimization of Micro-Structures with FEA Simulation

To check the effect of VIAs on redistribution of strain on the elastomer substrate, the FEA simulation was conducted using COMSOL Multiphysics (COMSOL Inc.) software. The overall designs of stretchable substrates with VIAs for simulation are presented in Figure 4.5. In order to prevent distortion of the strain distribution due

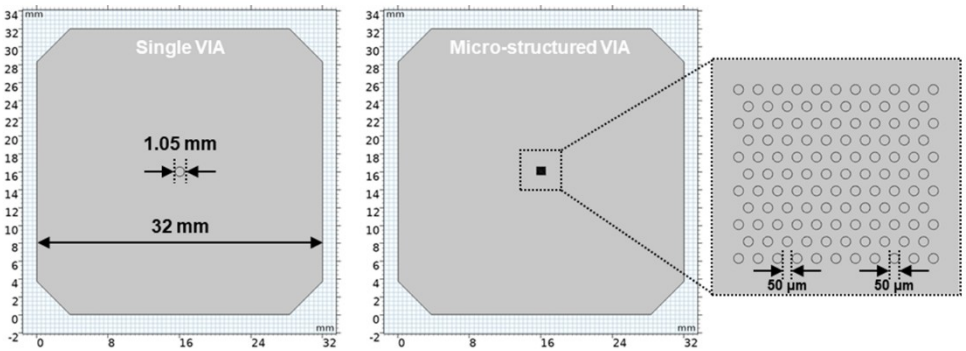

Figure 4.5 | The overall designs of stretchable substrates with VIAs for FEA simulation. In the case of micro-structured VIA, an area of 1.05x1.05 mm^2 was filled with micro-structured VIAs with radius of 50 μm while maintaining the spacing between the micro-structures equal to the diameter of the VIAs.

to the change in the width of the substrate except for VIAs according to the change in the size of VIA, the substrate width (32 mm) was set much larger than the size of VIA (1.05 mm). Figure 4.6a shows the FEA results of strain distribution when substrates are biaxially stretched by 20%. The strain distributed inside the composites is lower than that on the substrate because the composites with higher Young's modulus act as rigid islands that disperse the applied strain to the substrate. When the large single VIA is formed on the substrate, the strain is concentrated in a large area at the interface between VIA and the substrate. On the other hand, in the case of the substrate with micro-structured VIAs that the VIA is split into the smaller VIA arrays, the strain is concentrated only in a very narrow area around the VIAs. The profile of strain distribution along dotted red lines is presented in Figure 4.6b. There is no significant difference in the maximum strain in both cases. As shown in the inset graph of the difference in strain between the single and micro-structured

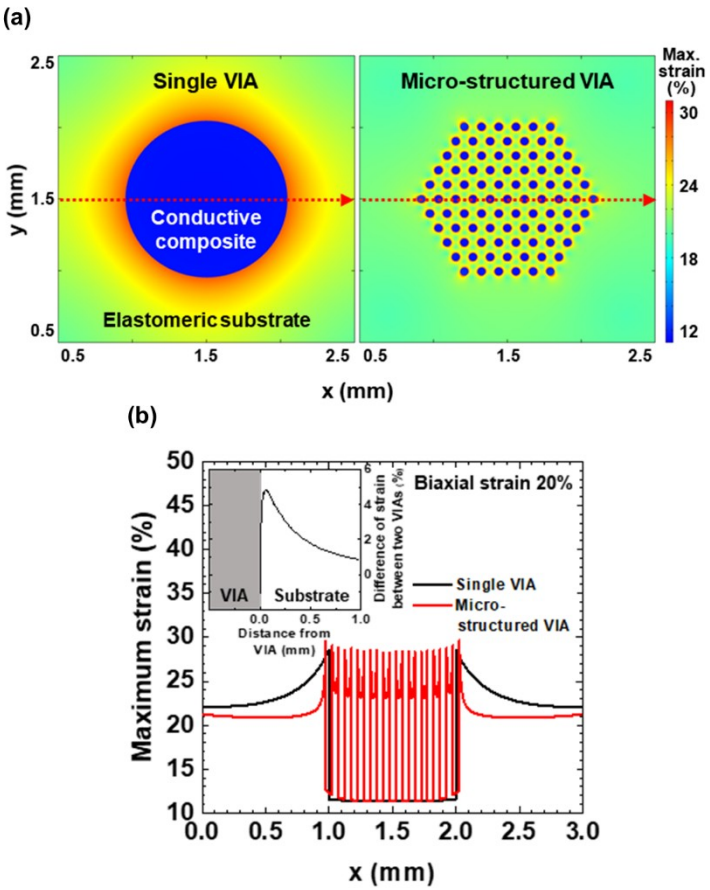

Figure 4.6 | FEA results of strain distribution on the substrate with VIAs. (a) Strain distribution when substrates are biaxially stretched by 20% in the case of the single and micro-structured VIAs. (b) The profile of strain distribution along dotted red lines.

VIAs, a higher strain of up to 5% is applied at the interface in the case of the single VIA. This higher strain in a large area induces the formation of cracks at the electrode connected to the VIA, resulting in reliability issues under repeated deformation.

To systematically analyze the effect of micro-structures on alleviating mechanical stress induced by the concentrated strain, the FEA simulation was

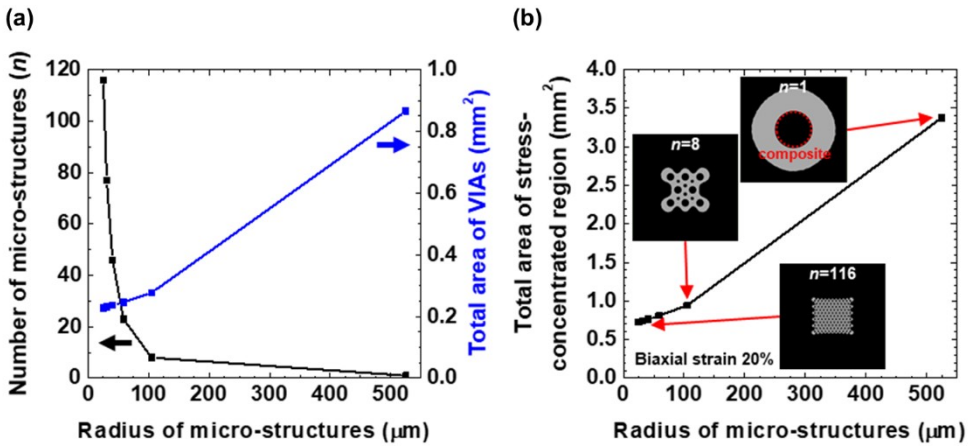

Figure 4.7 | FEA results of stress distribution when the area occupied by micro-structured VIAs remains the same. (a) Changes of number of micro-structures and total area of micro-structured VIAs according to the radius of micro-structures. (b) Changes of total area of stress-concentrated region where the von Mises stress is higher than the average von Mises stress on the pure PDMS substrate without VIA when the substrate is biaxially stretched by 20%. The gray-colored regions at the inset images indicate the stress-concentrated regions around the micro-structured VIAs.

conducted by varying the radius of micro-structured VIAs. An area of 1.05x1.05 mm^2 was filled with micro-structured VIAs with radii ranging from 50 to 525 μm while maintaining the spacing between the micro-structures equal to the diameter of the VIAs. When the VIA was split into smaller and more micro-structures, the number of micro-structures increased while the total area of VIAs gradually decreased (Figure 4.7a). When the substrate is biaxially stretched by 20%, the region where the von Mises stress is higher than 3.0 MPa is defined as the 'stress-concentrated region' because the average von Mises stress on the pure PDMS

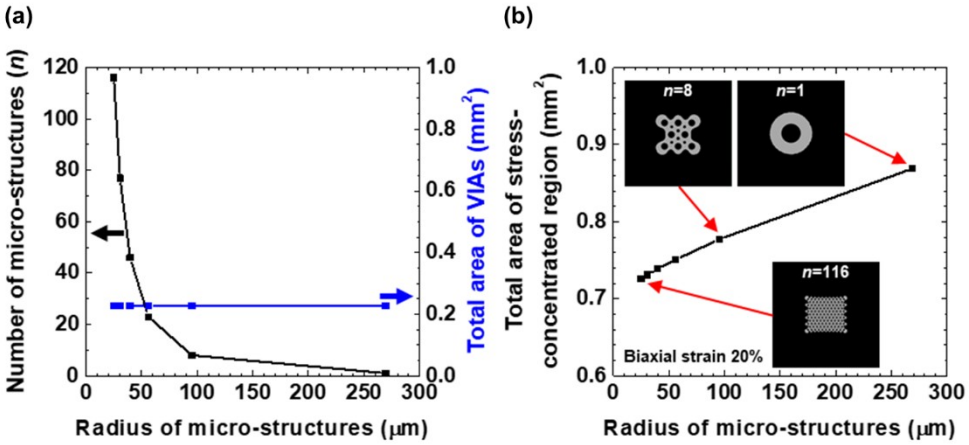

Figure 4.8 | FEA results of stress distribution when the total area of micro-structured VIAs remains the same. (a) Changes of number of micro-structures according to the radius of micro-structures. (b) Changes of total area of stress-concentrated region when the substrate is biaxially stretched by 20%.

substrate without VIA is 3.0 MPa. The gray-colored regions at the inset images of Figure 4.7b indicate the stress-concentrated regions around the micro-structured VIAs. The total area of stress-concentrated region decreases as the radius of micro-structured VIAs decreases, which is consistent with the strain distribution profile in Figure 4.6a. It is noted that the reduction in the total area of stress-concentrated region (decreased by 4.6 times from 3.38 mm^2 to 0.73 mm^2) is greater than the reduction in the total area of VIAs (decreased by 3.8 times from 0.87 mm^2 to 0.23 mm^2). In addition, even when radii of micro-structures are controlled to make the total area of VIAs same in each case, the total area of stress-concentrated region also decreases as the radius of micro-structured VIAs decreases (Figure 4.8). Therefore, the smaller the single VIA is split into micro-structures, the smaller the area where

the stress is concentrated, resulting in enhanced mechanical reliability of stretchable circuits. However, as the diameter of micro-structures decreases, there is a possibility that holes are clogged with the filler to disrupt the filling process of the composite. In order for the composite with a high volume fraction of filler to pass through a hole without clogging, the diameter of the hole must be at least 6 to 10 times of that of the filler.[131] Since the mean size of the silver-coated iron particles used in this paper is 4.5 μm, the diameter of micro-structures is determined to be 50 μm to avoid clogging issues.

4.3.3. Electrical and Mechanical Characteristics of Micro-Structured VIA

To compare the stretchability of VIAs according to the structure, stretching tests of stretchable electrodes with VIAs were conducted. A pair of single or micro-structured VIAs was inserted between the bottom and two top AgNW electrodes to make electrical connections between two layers (Figure 4.9a). The single VIA was fabricated using a magnetic field modulator that can induce convergence of ferromagnetic particles through modulation of the magnetic field as mentioned in Chapter 2. Changes in resistance of electrodes with VIAs according to the tensile strain were represented in Figure 4.9b. In the case of single VIAs, the electrode showed unstable resistance changes that the resistance increased rapidly even at low strain. On the other hand, the resistance of electrodes with micro-structured VIAs gradually increased according to the applied strain.

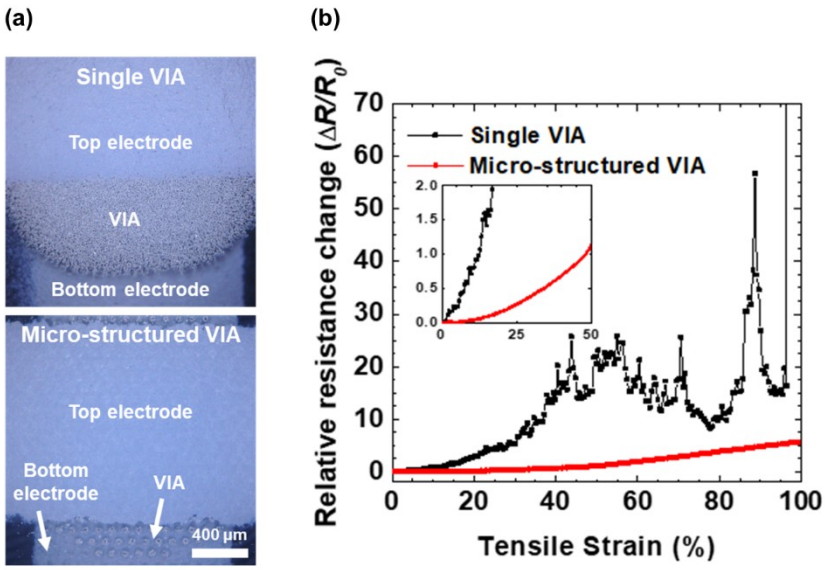

Figure 4.9 | Comparison of resistance characteristics between single and multi-structured VIAs according to the tensile strain. (a) Optical images of single and micro-structured VIAs inserted between top and bottom AgNW electrodes. (b) Relative resistance changes of electrodes with single and multi-structured VIAs according to the tensile strain.

In order to examine the mechanical stability of electrodes with VIAs in more detail, cyclic stretching tests were conducted. As shown in Figure 4.10, the resistance of electrodes with single VIAs increased by more than 50 times after just 100 repetitive stretching cycles. Contrastively, electrodes with micro-structured VIAs showed a stable resistance change even after 1000 cycles. Although the change of resistance at 50% strain increased from 1.4 to 2.3 times after 1000 cycles, the base resistance in a released state only changed by 10%. These results showed that the application of micro-structured VIAs had little effect on the stretchability of the

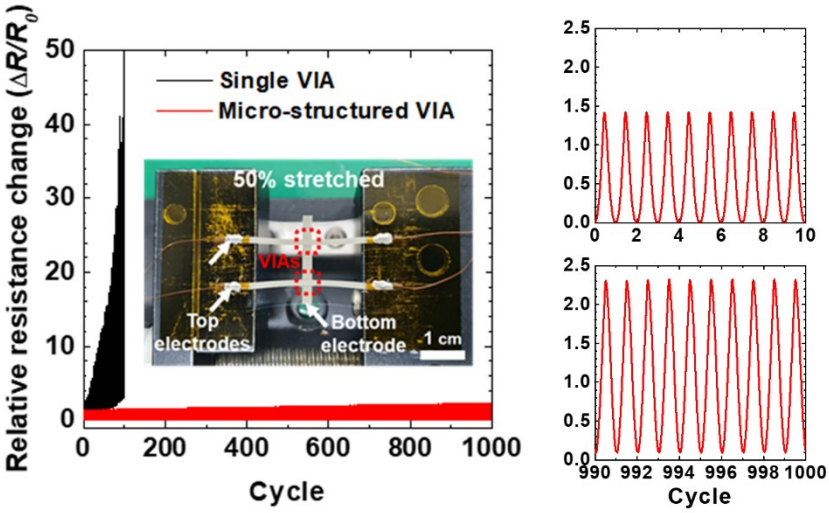

Figure 4.10 | Results of cyclic stretching tests of electrodes with single and micro-structured VIAs with the uniaxial strain of 50%. The first and last 10 cycles in case of micro-structured VIAs are depicted in the right side.

substrate, thereby curbing the occurrence of reliability issues compared to single VIAs.

To figure out the distribution of strain on actual samples under stretched states, the DIC analysis was conducted. The fine sodium percarbonate powder was uniformly scattered on the substrate using a N_2 gun to form random speckle patterns over the surface. After optical images of VIAs at the same position were captured according to the strain, the strain distribution was analyzed by tracking the movement of the speckle patterns using VIC-2D (Correlated Solutions) software (Figure 4.11). Under the uniaxially stretched state, in the case of the single VIA, the strain was concentrated at the interface between the VIA and substrate along the stretching direction, consistent with FEA results in Figure 4.6a. This concentrated

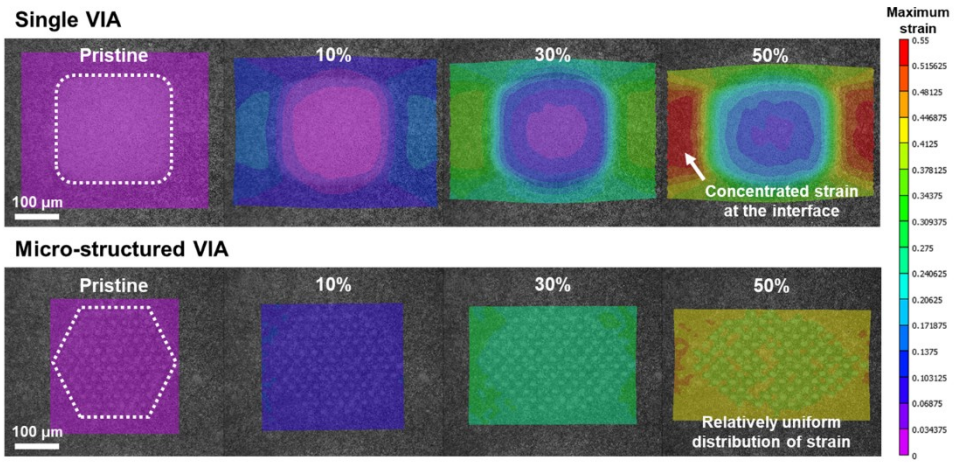

Figure 4.11 | Strain distribution of single and multi-structured VIAs according to the uniaxial strain analyzed by the DIC method. The optical images of speckle patterns on the surface were converted to the binary images for the analysis.

strain at the interface induced the formation of cracks at AgNWs under repetitive deformation as shown in the SEM image in Figure 4.12. These cracks caused mechanical instability that the resistance values under released and stretched states were both increased due to disconnection of conducting paths. On the other hand, in the case of micro-structured VIAs, the strain was uniformly distributed all over the surfaces compared to the single VIA. Due to the relatively lower strain at the interface induced by the uniform strain distribution, electrodes with micro-structured VIAs could show enhanced mechanical stability as shown in Figure 4.10.

Because measured resistance in Figure 4.9 is the sum of the resistance of AgNW electrodes and VIAs, it is ambiguous to figure out the resistance change of VIA itself according to the applied strain. Therefore, the transmission line method (TLM) was used to separate the resistance of VIAs from the resistance of AgNW

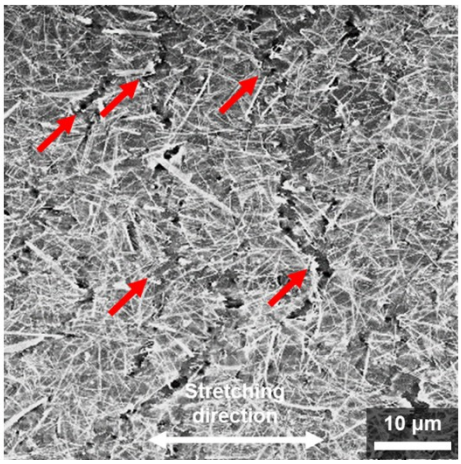

Figure 4.12 | SEM image of AgNWs at the interface between the single VIA and substrate when uniaxially stretched by 50%. Red arrows indicate cracks on AgNWs generated by repetitive deformation.

electrodes.[132, 133] As shown in Figure 4.13a, micro-structured VIAs with top AgNW electrodes were prepared on the bottom AgNW electrode. Intervals between each VIA varied from 1 mm to 5 mm, and the width of AgNW electrodes was 1 mm. The total resistance (R_{total}) between one VIA and another neighboring VIA can be expressed as

$$R_{total} = 2R_{lead} + 2R_{VIA} + R_{AgNW} \tag{4.1}$$

where R_{lead}, R_{VIA}, and R_{AgNW} are the resistance of the lead wire, VIAs, and AgNW electrode, respectively. Generally, R_{lead} can be ignored because other resistance values are much higher than R_{lead}. However, in this case, R_{VIA} and R_{AgNW} are too small to be distorted by R_{lead}. To prevent distortion of measured resistance originated from R_{lead}, the 4-wire measurement that can exclude the resistance of lead wires from the measured resistance was conducted.[134] A circuit diagram in Figure 4.13b shows the

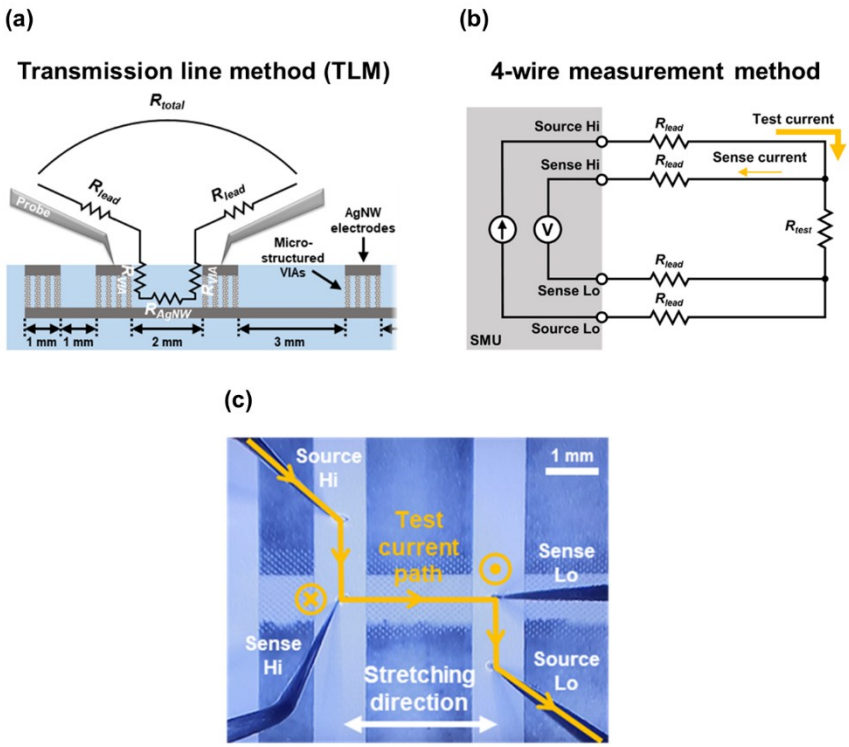

Figure 4.13 | Two measurement methods to accurately measure the resistance of VIA excluding the resistance of AgNW and contact resistance. (a) Schematic diagram of TLM for measurement of resistance of VIAs. Rlead, RVIA, and RAgNW represent the resistance of lead wires, VIAs, and AgNW electrodes, respectively. (b) Electric circuit diagram of measuring the voltage drop at the resistor under test with two lead wires when the constant test current is applied. (c) Optical image of the setup for measuring resistance of VIAs with four lead wires.

situation of measuring the voltage drop at the resistor under test with two lead wires when the constant current is applied with the other two lead wires. Due to the high input impedance of the voltmeter (>10^{10} Ω) compared with the resistance under test (R_{test}) (<10 Ω), the sense current that flows into the voltmeter is negligible compared with the test current. Therefore, regardless of the existence of R_{lead}, the voltage

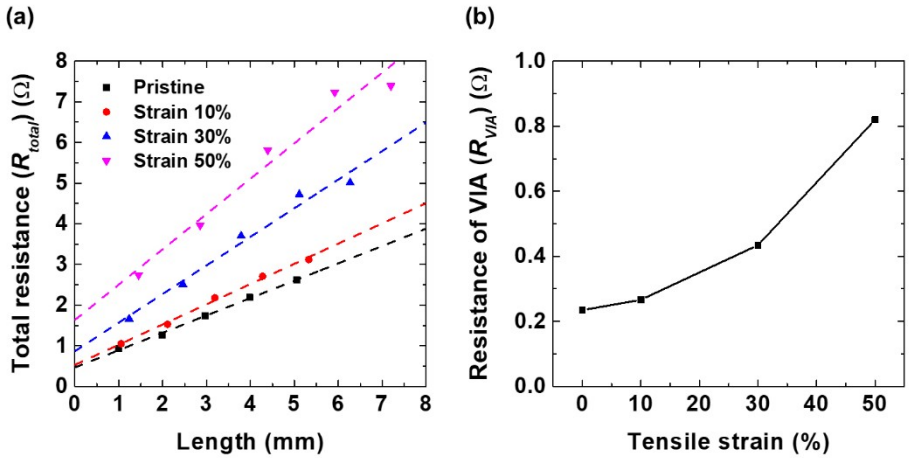

Figure 4.14 | Results of resistance measurement by combining TLM and 4-wire measurement method. (a) Measured total resistance according to the applied strain and intervals and fitted lines of total resistance at the different strain. (b) Resistance values of micro-structured VIAs according to the tensile strain extracted from the fitted lines in Figure 4d.

measured by the voltmeter divided by the test current can be approximated by R_{test} because the voltage drop at R_{lead} is insignificant. By combining this 4-wire measurement with the TLM, Equation (4.1) can be approximated by

$$R_{total} = 2R_{VIA} + R_{AgNW} \tag{4.2}$$

By assuming that the resistance of AgNW electrodes is uniform throughout the substrate, Equation (4.2) can be rewritten as[133]

$$R_{total} = 2R_{VIA} + R_S \frac{L}{W} \tag{4.3}$$

where R_S, L, and W are the sheet resistance, length, and width of the AgNW electrode, respectively. Measuring the resistance between two neighboring VIAs with different intervals were conducted with four lead wires (Figure 4.13c). The test current flowed

from the node 'Source Hi' to the node 'Source Lo' through a pair of micro-structured VIA. To figure out the effect of tensile strain on the resistance of VIA, the substrate was uniaxially stretched up to 50% parallel to the bottom electrode. Measured R_{total} and fitted lines according to the applied strain are plotted in Figure 4.14a. According to Equation (4.3), the y-intercepts (when L=0) of fitted lines represent $2R_{VIA}$. Extracted values of R_{VIA} according to the tensile strain are shown in Figure 4.14b. When the strain was not applied to the substrate, VIA with a cross-section area of 1 mm^2 showed resistance of 0.23 Ω (conductivity: 435 S/m) that was much smaller than that of AgNW electrodes. Although R_{VIA} gradually increased according to the tensile strain and increased by 3.6 times at 50% strain, it was still negligible compared to the change of R_{AgNW}. Therefore, it can be seen that micro-structured VIAs have insignificant effects on the resistance of entire circuits when applied to stretchable electronics.

4.3.4. Realization of Multi-Layered Stretchable Electronics Utilizing Micro-structured VIA

For the practical application of micro-structured VIAs to electric circuits, a facile and site-selective patterning method of VIA is needed. A pneumatic dispensing system is used to pattern the elastomer composite due to its jettability of highly viscous liquid. Desired VIA patterns are achieved on the PDMS membrane by inputting a CAD file to the dispensing system that is designed using AutoCAD (Autodesk Inc.) software. By using this automated patterning system, complex

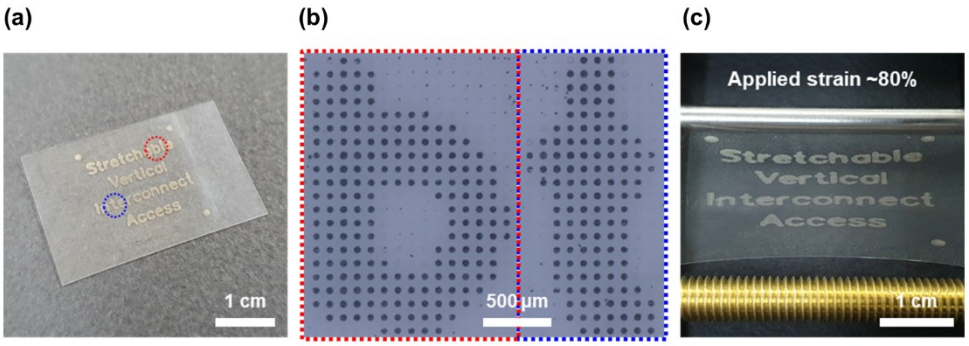

Figure 4.15 | Patternability test of automated patterning system. (a) Optical image of the PDMS substrate with micro-structured VIAs patterned as the English words 'Stretchable Vertical Interconnect Access' and (b) magnified images of the letter 'b' and 't'. (c) Optical image of the PDMS substrate with VIA patterns when uniaxially stretched up to 80%.

patterns such as the English words 'Stretchable Vertical Interconnect Access' could be implemented (Figure 4.15a). With a 28-gauge nozzle (inner diameter of 0.18 mm), letters were finely patterned enough to distinguish the font of the letters (Figure 4.15b). Even under the high tensile strain, the fabricated VIA patterns were not torn or delaminated from the PDMS substrate to stably maintain their shapes (Figure 4.15c).

A bottom-up fabrication process of multi-layered circuits utilizing the patterning technique is shown in Figure 4.16a. The overall process is carried out with one carrier glass where the PDMS base substrate for multi-layered structures is attached. Lamination of the micro-perforated membrane for the second layer is followed by patterning of the PDMS composite on the desired area. The membrane is covered by the plastic substrate for embedding of AgNW electrodes and cured

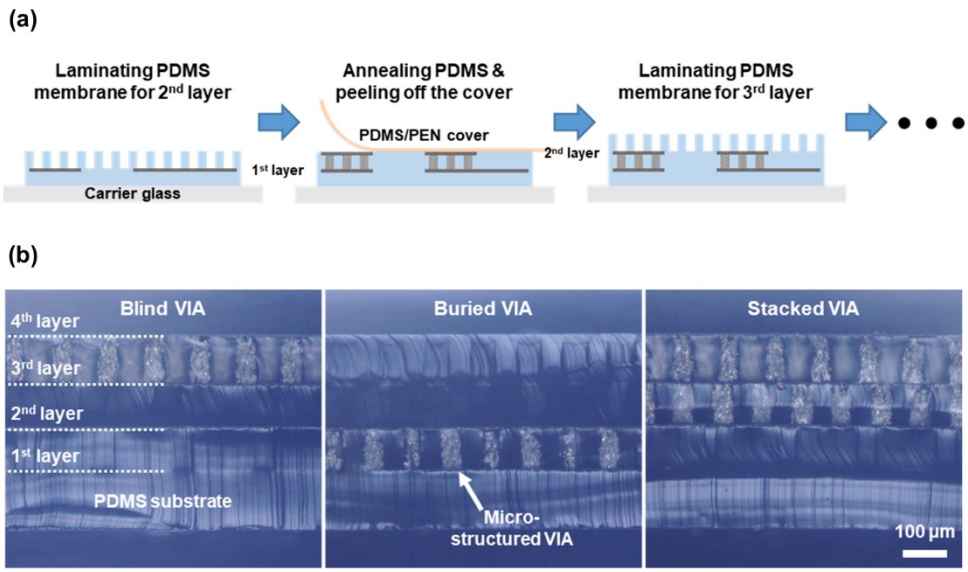

Figure 4.16 | Facile bottom-up process for the multi-layered structure. (a) Schematic illustration of the bottom-up fabrication process of multi-layered circuits with micro-structured VIAs. (b) Cross-sectional images of stretchable multi-layered circuits with various types of VIAs that are used in commercial PCBs

with the applied magnetic field. To fabricate the multi-layered structures, these processes are repeated until the desired number of layers is achieved. Using this stacking process, a demonstration of VIAs connecting different layers at multi-layered structures like PCBs was conducted. In commercial PCBs, various types of VIAs are used for efficient electrical connections between two or more different layers in multi-layered electric circuits, such as a blind VIA that connects an outer layer to one of the inner layers; a buried VIA that connects the inner layers without being exposed to the outer layer; and a stacked VIA that connects more than three layers. These three types of VIAs were successfully implemented to the stretchable platform through the multi-layered structure with four layers of circuits (Figure

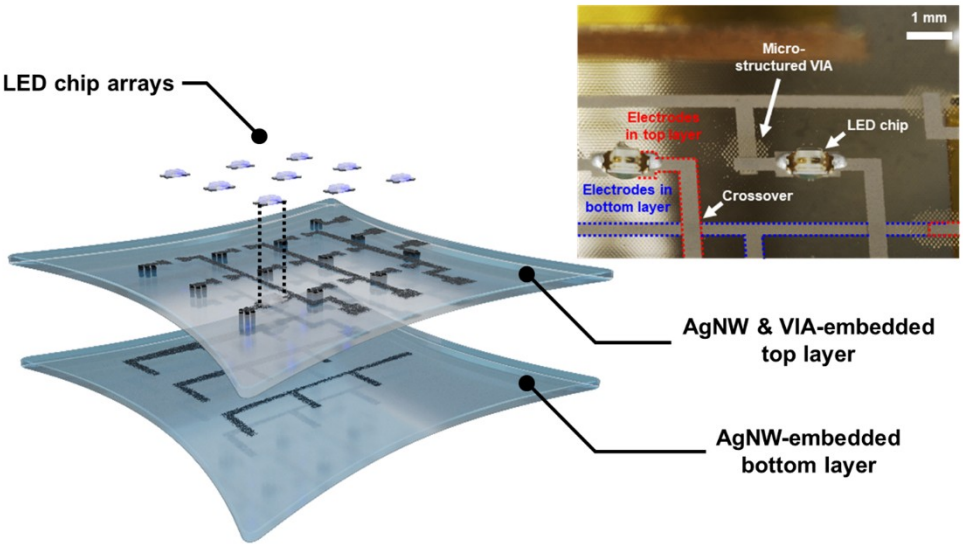

Figure 4.17 | Application of micro-structured VIAs to the stretchable electronics. (a) Schematic illustration of 3x3 passive matrix LED arrays fabricated on the stretchable substrate with embedded AgNW electrodes and micro-structured VIAs. (b) Optical image of micro-structured VIAs, crossover, and LED chips bonded to the stretchable substrate.

4.16b). Due to the facile patterning and stacking processes, proposed micro-structured VIAs have possibilities to be applied to realize multi-layered stretchable electronics applications.

To examine the feasibility of multi-layered stretchable circuits containing micro-structured VIAs, stretchable hybrid electronics (SHE) applications were demonstrated with surface mount device light-emitting diode (SMD LED) chips. Previously in our group, for SHE applications, the pre-stretching process of the elastomer substrate before the deposition of electrodes was conducted to give stretchability to brittle electrodes by forming wrinkles on the substrate. In addition,

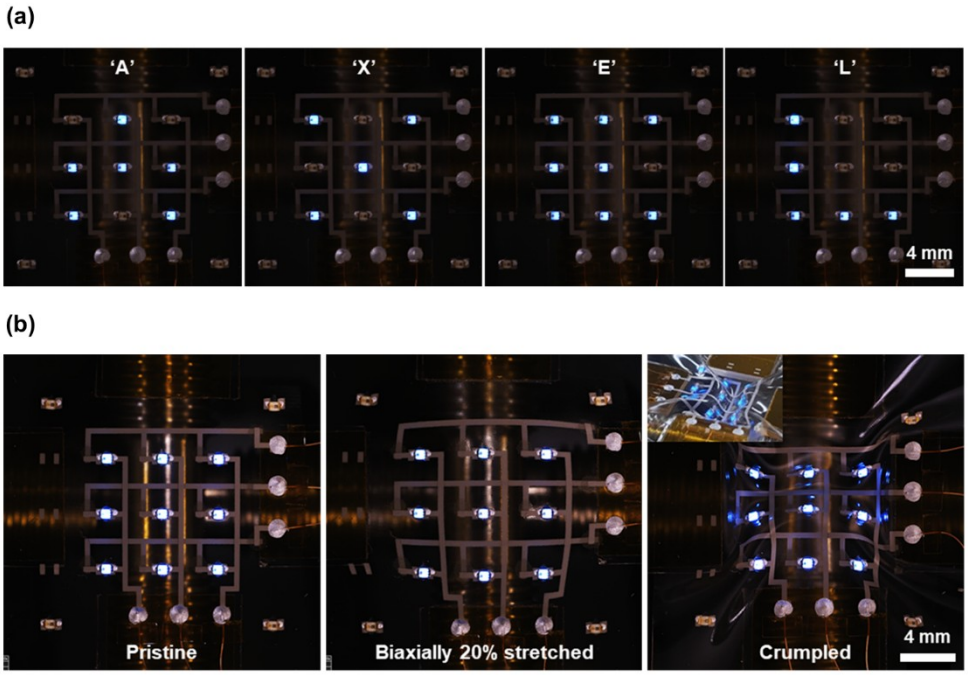

Figure 4.18 | Operation of stretchable LED arrays. (a) Passive matrix addressing of LED arrays for indicating letters of 'A', 'X', 'E', and 'L'. (b) Optical images of operating LED arrays under biaxially 20% stretched or crumpled states.

manual operation for the formation of the crossover was needed due to the absence of VIAs. These complex processes are not suitable for the fabrication of multi-layered structures because they are time-consuming and have the possibility of misalignment due to distortion of the substrate during the process. In order to apply a facile fabrication process that can solve these problems, intrinsically stretchable AgNW electrodes and micro-structured VIAs were used to fabricate 3x3 passive matrix LED arrays (Figure 4.17). SMD LED chips were placed on contact pads of AgNW electrodes by a pick-and-place machine (TM220A, Hangzhou NeoDen Technology Co., Ltd.) after the silver and pure epoxy as soldering materials were

printed by a dispensing system. An optical image that the LED chip is bonded to the contact pads and connected to the circuits through the crossover and VIAs is shown in Figure 4.17. Since the LED arrays were fabricated in the form of a passive matrix, driving the arrays by each pixel, column, and row was possible. By driving each row at intervals of 5 ms using a switching, indicating letters of ‘A’, ‘X’, ‘E’, and ‘L’ was successfully conducted (Figure 4.18a). The stretchable platform with LED arrays was attached to the custom-made biaxially stretching equipment to verify that the device normally operated even under deformed states. Due to the mechanical stability of micro-structured VIAs, LED arrays could operate stably without any visible degradation of performance when biaxially stretched up to 20% or crumpled (Figure 4.18b). This demonstration of stretchable LED arrays shows the applicability of micro-structured VIAs to the bottom-up process for the realization of highly integrated stretchable electronics applications.

4.4. Conclusion

In summary, this chapter introduced micro-structured anisotropic elastomer composite-based VIAs for multi-layered stretchable electronics utilizing the micro-perforated membrane and highly conductive ferromagnetic particles with core-shell structure. The elastomer composite in which the applied magnetic field formed the anisotropic filamentous structures showed drastically increased conductivity compared to the isotropic composite while maintaining its stretchability. Micro-structured VIAs were achieved by inserting the composite into through-holes at the perforated membrane that was fabricated with a replication method. Micro-structures efficiently dispersed the mechanical stress concentrated at the interface between VIA and the substrate under the stretched state. The dispersed strain throughout the substrate greatly enhanced the mechanical reliability of micro-structured VIAs, that the electrode with VIAs showed a resistance change of only 10% after the 1000 cycles at the repeated stretching test. In addition, the change of the resistance of VIA itself according to the tensile strain was analyzed by combining TLM and 4-wire measurement. Micro-structured VIAs had negligible effects on the change of resistance of entire circuits under the stretched state because the change of resistance of VIAs was insignificant compared to that of stretchable AgNW electrodes. The proposed fabrication method that simultaneously forms VIAs and embedded AgNW electrodes on one substrate enables the bottom-up process for multi-layered structures without any complex strategies used in the other fabrication processes of

stretchable VIAs. By utilizing the bottom-up process, various types of VIAs used in the commercial PCBs were implemented to the stretchable substrate with four layers of circuits. Additionally, passive matrix LED arrays for SHE applications were demonstrated to examine the feasibility of multi-layered stretchable circuits containing micro-structured VIAs. Time-consuming and complex fabrication processes for SHE applications, such as the pre-stretching process or manual fabrication of the crossover, were not needed at the proposed method. As a result, stretchable LED arrays could operate stably under crumpled or biaxially stretched states due to the mechanical durability of micro-structured VIAs. This demonstration shows that proposed micro-structured VIAs have the possibilities to play a major role in the realization of highly integrated stretchable electronics.

Chapter 5. Conclusion

5.1. Summary

In this dissertation, the comprehensive strategies with novel materials and designs were proposed to demonstrate the key components for realization of multi-functional stretchable electronic systems. The components for the highly integrated multi-functional system can be divided into three main categories: a single-level functional device, a VIA for integrating each functional device in 3D scheme, and a probe unit forming electrical connections for signal transfer and inspection of fabricated devices. The material-based and structure-based strategies were applied to impart not only the softness, but also the functionality suitable for each role to the device components. As a material-based strategy, ferromagnetic particles whose 3D structures as well as 2D distribution on the substrate can be controlled with the magnetic field were used for optimization of electrical characteristics. By forming the composite with elastomer, ferromagnetic particles could achieve stretchability while retaining the functionality according to characteristics of the filler. In addition, as a structure-based strategy, micro-structures introduced to the composite through the perforated membrane enabled additional characteristics such as high spatial resolution or dispersion of the mechanical stress. The feasibility of each component

to be applied to soft electronics was verified through the demonstration of practical applications.

As a single-level active device for the multi-functional system, soft pressure sensor arrays with high resolution up to 100 ppi that can cover the resolution of various types of human tactile sense were introduced in Chapter 2. By applying the magnetic field to the ferromagnetic elastomer composite that shows piezoresistivity, sensitivity of the pressure sensor was highly enhanced with the anisotropic filamentous structure of ferromagnetic particles. Due to the use of ferromagnetic particles as the filler, pressure sensor arrays could be patterned with modulation of the magnetic field. However, when resolution of the modulator reached 50 ppi, ferromagnetic particles were not fully patterned due to reduced gradient of the magnetic flux density induced by the interference between pillar structures. Therefore, the patterning method utilizing perforated membrane as a frame was applied to achieve resolution of 100 ppi that is the minimum limit of the human tactile receptor for sensing injurious forces. The patterned pressure sensor showed remarkable sensitivity of higher than 10^5 kPa^{-1} and great mechanical reliability that the sensor operated stably even after cyclic press of 5,000 times. At the 2PD test that determines the spatial resolution of the sensor, pressure sensor arrays could distinguish two pressed points with the minimum gap of 250 μm without any severe crosstalk with neighboring pixels. Real-time pressure mapping of 2,304 pixels was carried out using the computer-connected readout system. In addition, real-time categorization of applied forces according to the pressure level and pressure-applied area was implemented using Python program.

As a connector for the signal transfer and inspection process, the soft probe unit that prevents damage to the electrodes on deformable electronic devices caused by the physical contact was introduced in Chapter 3. By introducing highly conductive ferromagnetic particles with the core-shell structure, conductive elastomer composite that showed conductivity without the applied pressure even at the low filler concentration was achieved. The soft probe unit with high conductivity and no crosstalk was achieved by introduction of patterning method using the micro-perforated membrane. By utilizing the PDMS replication process for the PDMS mold and optimized spin-coating process, the SPU with high resolution up to 500 ppi was successfully fabricated. When the SPU was applied to the inkjet-printed silver electrodes on the plastic substrate, the resistance changed only 0.6% after 100 times of repetitive pressing. In addition, the SPU acted as a shock-absorbing layer that prevents generation of scrape on the surface of the electrode. Because the SPU pixel was isolated to a size of 20 μm with a perforated membrane, short circuit between neighboring electrodes with a gap of 35 μm did not occur when the contact of electrodes with fine pitch was carried out. When the SPU was bonded to the FPCB by using an irreversible siloxane bonding method, the increase of contact resistance induced by insertion of the SPU was low as 0.1 Ω. In contrast to the case of not-patterned composite, inspection operations of flexible display panel such as color switching were performed normally when the SPU was applied to the FPCB connector of the inspection device. In addition, the solution-processed PLED could operate with the SPU-laminated cathode due to the conformal contact between the functional layer and cathode induced by the insertion of SPU.

As a connecting link for integration of single-level devices for the multi-functional system, the mechanically durable stretchable VIA enabling the facile bottom-up stacking process was introduced in Chapter 4. Micro-structures fabricated with the perforated membrane efficiently dispersed the mechanical stress concentrated at the interface between VIA and the substrate under the stretched state. The dispersed strain throughout the substrate greatly enhanced the mechanical reliability of micro-structured VIAs, that the electrode with VIAs showed a resistance change of only 10% after the 1000 cycles at the repeated stretching test. In addition, the change of the resistance of VIA itself according to the tensile strain was analyzed by combining TLM and 4-wire measurement. Micro-structured VIAs had negligible effects on the change of resistance of entire circuits under the stretched state because the change of resistance of VIAs was insignificant compared to that of stretchable AgNW electrodes. The proposed fabrication method that simultaneously forms VIAs and embedded AgNW electrodes on one substrate enables the bottom-up process for multi-layered structures without any complex strategies used in the other fabrication processes of stretchable VIAs. By utilizing the bottom-up process, various types of VIAs used in the commercial PCBs were implemented to the stretchable substrate with four layers of circuits. Additionally, passive matrix LED arrays for SHE applications were demonstrated to examine the feasibility of multi-layered stretchable circuits containing micro-structured VIAs. Time-consuming and complex fabrication processes for SHE applications, such as the pre-stretching process or manual fabrication of the crossover, were not needed at the proposed method. As a result, stretchable LED arrays could operate stably under

crumpled or biaxially stretched states due to the mechanical durability of micro-structured VIAs.

In conclusion, this dissertation provides the novel methodologies for realization of key components for highly integrated stretchable electronics utilizing the micro-structured anisotropic elastomer composite. Impartment of functionality and enhancement of device performance were carried out with formation of the magnetic field, change of filler characteristics, and introduction of micro-structures. By utilizing these engineered elastomer composites, various practical applications were demonstrated, such as high resolution real-time pressure mapping and categorization; non-damaging inspection of deformable light-emitting devices at pixel- and device level; and multi-layered stretchable electronics fabricated with the facile stacking process. In addition to the verified feasibility of proposed methodologies, facile and large-area processability of the micro-perforated membrane fabricated by utilizing a silicon master mold manufactured with the photolithography process used in the semiconductor industry, facilitates the commercialization of the proposed technology. It is expected that systematic approaches to implementing soft electrical components through design, analysis, and optimization in this dissertation will pave the way for realization of highly integrated multi-functional stretchable electronic systems.

Bibliography

(1) Cai, P.; Wan, C.; Pan, L.; Matsuhisa, N.; He, K.; Cui, Z.; Zhang, W.; Li, C.; Wang, J.; Yu, J.; et al. Locally coupled electromechanical interfaces based on cytoadhesion-inspired hybrids to identify muscular excitation-contraction signatures. *Nat. Commun.* **2020**, *11* (1), 2183.

(2) Shi, X.; Zuo, Y.; Zhai, P.; Shen, J.; Yang, Y.; Gao, Z.; Liao, M.; Wu, J.; Wang, J.; Xu, X.; et al. Large-area display textiles integrated with functional systems. *Nature* **2021**, *591* (7849), 240-245.

(3) Boutry, C. M.; Kaizawa, Y.; Schroeder, B. C.; Chortos, A.; Legrand, A.; Wang, Z.; Chang, J.; Fox, P.; Bao, Z. A stretchable and biodegradable strain and pressure sensor for orthopaedic application. *Nat. Electron.* **2018**, *1* (5), 314-321.

(4) Lee, Y.; Chung, J. W.; Lee, G. H.; Kang, H.; Kim, J. Y.; Bae, C.; Yoo, H.; Jeong, S.; Cho, H.; Kang, S. G.; et al. Standalone real-time health monitoring patch based on a stretchable organic optoelectronic system. *Sci. Adv.* **2021**, *7* (23), eabg9180.

(5) Lee, Y.; Kim, D. S.; Jin, S. W.; Lee, H.; Jeong, Y. R.; You, I.; Zi, G.; Ha, J. S. Stretchable array of CdSe/ZnS quantum-dot light emitting diodes for visual display of bio-signals. *Chem. Eng. J.* **2022**, *427*, 130858.

(6) Yang, J. C.; Mun, J.; Kwon, S. Y.; Park, S.; Bao, Z.; Park, S. Electronic skin: recent progress and future prospects for skin-attachable devices for health monitoring, robotics, and prosthetics. *Adv. Mater.* **2019**, *31* (48), 1904765.

(7) Wang, M.; Luo, Y.; Wang, T.; Wan, C.; Pan, L.; Pan, S.; He, K.; Neo, A.; Chen, X. Artificial skin perception. *Adv. Mater.* **2021**, *33* (19), 2003014.

(8) Byun, J.; Lee, Y.; Yoon, J.; Lee, B.; Oh, E.; Chung, S.; Lee, T.; Cho, K. J.; Kim, J.; Hong, Y. Electronic skins for soft, compact, reversible assembly of wirelessly activated fully soft robots. *Sci. Robot.* **2018**, *3* (18), eaas9020.

(9) Su, Q.; Zou, Q.; Li, Y.; Chen, Y.; Teng, S. Y.; Kelleher, J. T.; Nith, R.; Cheng, P.; Li, N.; Liu, W.; et al. A stretchable and strain-unperturbed pressure sensor for

motion interference-free tactile monitoring on skins. *Sci. Adv.* **2021**, *7* (48), eabi4563.

(10) Loughrey, C. *Minority Report: 6 predictions that came true, 15 years on*. Independent, https://www.independent.co.uk/arts-entertainment/films/features/minority-report-15th-anniversary-predictive-policing-gesture-based-computing-facial-and-optical-recognition-a7807666.html (accessed 25th November, 2022).

(11) Tonino, R. P. B.; Larimer, K.; Eissen, O.; Schipperus, M. R. Remote patient monitoring in adults receiving transfusion or infusion for hematological disorders using the VitalPatch and accelerateIQ monitoring system: Quantitative feasibility study. *JMIR Hum. Factors* **2019**, *6* (4), e15103.

(12) *Someya Group Organic Transistor Lab*. Someya Group, http://www.ntech.t.u-tokyo.ac.jp/en/research_results/index.html (accessed 25th November, 2022).

(13) *Blast From the Past: Vintage Technologies That We No Longer Use*. WebdesignerDepot, https://www.webdesignerdepot.com/2010/02/blast-from-the-past-vintage-technologies-that-we-no-longer-use/ (accessed 25th November, 2022).

(14) Johnson, L. *Samsung Gear S3 release date, design, features, price and everything you need to know*. Ditial Spy, https://www.digitalspy.com/tech/wearables/a798568/samsung-gear-s3-release-date-design-features-price-and-everything-you-need-to-know/ (accessed 25th November, 2022).

(15) Byun, J.; Lee, B.; Oh, E.; Kim, H.; Kim, S.; Lee, S.; Hong, Y. Fully printable, strain-engineered electronic wrap for customizable soft electronics. *Sci. Rep.* **2017**, *7*, 45328.

(16) Byun, J.; Oh, E.; Lee, B.; Kim, S.; Lee, S.; Hong, Y. A Single Droplet-Printed Double-Side Universal Soft Electronic Platform for Highly Integrated Stretchable Hybrid Electronics. *Adv. Funct. Mater.* **2017**, *27* (36), 1701912.

(17) Oh, E.; Byun, J.; Lee, B.; Kim, S.; Kim, D.; Yoon, J.; Hong, Y. Modulus-Gradient Conductive Core-Shell Structures Formed by Magnetic Self-

Assembling and Printing Processes for Highly Stretchable Via Applications. *Adv. Electron. Mater.* **2017**, *3* (3), 1600517.

(18) Oh, E.; Kim, T.; Yoon, J.; Lee, S.; Kim, D.; Lee, B.; Byun, J.; Cho, H.; Ha, J.; Hong, Y. Highly Reliable Liquid Metal–Solid Metal Contacts with a Corrugated Single-Walled Carbon Nanotube Diffusion Barrier for Stretchable Electronics. *Adv. Funct. Mater.* **2018**, *28* (51), 1806014.

(19) Kim, Y. S.; Mahmood, M.; Lee, Y.; Kim, N. K.; Kwon, S.; Herbert, R.; Kim, D.; Cho, H. C.; Yeo, W. H. All-in-one, wireless, stretchable hybrid electronics for smart, connected, and ambulatory physiological monitoring. *Adv. Sci.* **2019**, *6* (17), 1900939.

(20) Lee, B.; Cho, H.; Jeong, S.; Yoon, J.; Jang, D.; Lee, D. K.; Kim, D.; Chung, S.; Hong, Y. Stretchable hybrid electronics: combining rigid electronic devices with stretchable interconnects into high-performance on-skin electronics. *J. Inf. Disp.* **2022**, 1-22.

(21) Oh, J. Y.; Kim, S.; Baik, H. K.; Jeong, U. Conducting polymer dough for deformable electronics. *Adv. Mater.* **2016**, *28* (22), 4455-4461.

(22) Wang, Y.; Zhu, C.; Pfattner, R.; Yan, H.; Jin, L.; Chen, S.; Molina-Lopez, F.; Lissel, F.; Liu, J.; Rabiah, N. I.; et al. A highly stretchable, transparent, and conductive polymer. *Sci. Adv.* **2017**, *3* (3), e1602076.

(23) Lee, J. H.; Jeong, Y. R.; Lee, G.; Jin, S. W.; Lee, Y. H.; Hong, S. Y.; Park, H.; Kim, J. W.; Lee, S.-S.; Ha, J. S. Highly conductive, stretchable, and transparent PEDOT: PSS electrodes fabricated with triblock copolymer additives and acid treatment. *ACS Appl. Mater. Interfaces* **2018**, *10* (33), 28027-28035.

(24) Yang, Y.; Sun, N.; Wen, Z.; Cheng, P.; Zheng, H.; Shao, H.; Xia, Y.; Chen, C.; Lan, H.; Xie, X. Liquid-metal-based super-stretchable and structure-designable triboelectric nanogenerator for wearable electronics. *ACS Nano* **2018**, *12* (2), 2027-2034.

(25) Pan, C.; Markvicka, E. J.; Malakooti, M. H.; Yan, J.; Hu, L.; Matyjaszewski, K.; Majidi, C. A liquid-metal–elastomer nanocomposite for stretchable dielectric materials. *Adv. Mater.* **2019**, *31* (23), 1900663.

(26) Krisnadi, F.; Nguyen, L. L.; Ma, J.; Kulkarni, M. R.; Mathews, N.; Dickey, M. D. Directed Assembly of Liquid Metal–Elastomer Conductors for Stretchable and Self-Healing Electronics. *Adv. Mater.* **2020**, *32* (30), 2001642.

(27) Chortos, A.; Zhu, C.; Oh, J. Y.; Yan, X.; Pochorovski, I.; To, J. W.-F.; Liu, N.; Kraft, U.; Murmann, B.; Bao, Z. Investigating limiting factors in stretchable all-carbon transistors for reliable stretchable electronics. *ACS Nano* **2017**, *11* (8), 7925-7937.

(28) Yoon, J.; Joo, Y.; Oh, E.; Lee, B.; Kim, D.; Lee, S.; Kim, T.; Byun, J.; Hong, Y. Soft Modular Electronic Blocks (SMEBs): A Strategy for Tailored Wearable Health-Monitoring Systems. *Adv. Sci.* **2019**, *6* (5), 1801682.

(29) Kim, T.; Kim, D.; Yoon, J.; Joo, Y.; Hong, Y. Stamp-Perforation-Inspired Micronotch for Selectively Tearing Fiber-Bridged Carbon Nanotube Thin Films and Its Applications for Strain Classification. *ACS Appl. Mater. Interfaces* **2021**, *13* (27), 32307-32315.

(30) Matsuhisa, N.; Kaltenbrunner, M.; Yokota, T.; Jinno, H.; Kuribara, K.; Sekitani, T.; Someya, T. Printable elastic conductors with a high conductivity for electronic textile applications. *Nat. Commun.* **2015**, *6* (1), 1-11.

(31) Ko, Y.; Oh, J.; Park, K. T.; Kim, S.; Huh, W.; Sung, B. J.; Lim, J. A.; Lee, S.-S.; Kim, H. Stretchable conductive adhesives with superior electrical stability as printable interconnects in washable textile electronics. *ACS Appl. Mater. Interfaces* **2019**, *11* (40), 37043-37050.

(32) Wang, H.; Yao, Y.; He, Z.; Rao, W.; Hu, L.; Chen, S.; Lin, J.; Gao, J.; Zhang, P.; Sun, X. A highly stretchable liquid metal polymer as reversible transitional insulator and conductor. *Adv. Mater.* **2019**, *31* (23), 1901337.

(33) Chiang, Y.-C.; Wu, H.-C.; Wen, H.-F.; Hung, C.-C.; Hong, C.-W.; Kuo, C.-C.; Higashihara, T.; Chen, W.-C. Tailoring Carbosilane Side Chains toward Intrinsically Stretchable Semiconducting Polymers. *Macromol.* **2019**, *52* (11), 4396-4404.

(34) Scott, J. I.; Xue, X.; Wang, M.; Kline, R. J.; Hoffman, B. C.; Dougherty, D.; Zhou, C.; Bazan, G.; O'Connor, B. T. Significantly Increasing the Ductility of

High Performance Polymer Semiconductors through Polymer Blending. *ACS Appl. Mater. Interfaces* **2016**, *8* (22), 14037-14045.

(35) Mun, J.; Kang, J.; Zheng, Y.; Luo, S.; Wu, H. C.; Matsuhisa, N.; Xu, J.; Wang, G. N.; Yun, Y.; Xue, G.; et al. Conjugated Carbon Cyclic Nanorings as Additives for Intrinsically Stretchable Semiconducting Polymers. *Adv. Mater.* **2019**, *31* (42), e1903912.

(36) Oh, J. Y.; Rondeau-Gagne, S.; Chiu, Y. C.; Chortos, A.; Lissel, F.; Wang, G. N.; Schroeder, B. C.; Kurosawa, T.; Lopez, J.; Katsumata, T.; et al. Intrinsically stretchable and healable semiconducting polymer for organic transistors. *Nature* **2016**, *539* (7629), 411-415.

(37) Wang, G.-J. N.; Shaw, L.; Xu, J.; Kurosawa, T.; Schroeder, B. C.; Oh, J. Y.; Benight, S. J.; Bao, Z. Inducing Elasticity through Oligo-Siloxane Crosslinks for Intrinsically Stretchable Semiconducting Polymers. *Adv. Funct. Mater.* **2016**, *26* (40), 7254-7262.

(38) Mun, J.; Wang, G. J. N.; Oh, J. Y.; Katsumata, T.; Lee, F. L.; Kang, J.; Wu, H. C.; Lissel, F.; Rondeau-Gagné, S.; Tok, J. B. H.; et al. Effect of Nonconjugated Spacers on Mechanical Properties of Semiconducting Polymers for Stretchable Transistors. *Adv. Funct. Mater.* **2018**, *28* (43), 1804222.

(39) Yin, D.; Feng, J.; Jiang, N.-R.; Ma, R.; Liu, Y.-F.; Sun, H.-B. Two-dimensional stretchable organic light-emitting devices with high efficiency. *ACS Appl. Mater. Interfaces* **2016**, *8* (45), 31166-31171.

(40) Jeong, S.; Yoon, H.; Lee, B.; Lee, S.; Hong, Y. Distortion-Free Stretchable Light-Emitting Diodes via Imperceptible Microwrinkles. *Adv. Mater. Technol.* **2020**, *5*, 2000231.

(41) Park, K.; Lee, D. K.; Kim, B. S.; Jeon, H.; Lee, N. E.; Whang, D.; Lee, H. J.; Kim, Y. J.; Ahn, J. H. Stretchable, transparent zinc oxide thin film transistors. *Adv. Funct. Mater.* **2010**, *20* (20), 3577-3582.

(42) Kim, N.; Kim, J.; Seo, J.; Hong, C.; Lee, J. Stretchable Inorganic LED Displays with Double-Layer Modular Design for High Fill Factor. *ACS Appl. Mater. Interfaces* **2022**, *14* (3), 4344-4351.

(43) Lee, J.; Wu, J.; Shi, M.; Yoon, J.; Park, S. I.; Li, M.; Liu, Z.; Huang, Y.; Rogers, J. A. Stretchable GaAs photovoltaics with designs that enable high areal coverage. *Adv. Mater.* **2011**, *23* (8), 986-991.

(44) Lee, J.; Wu, J.; Ryu, J. H.; Liu, Z.; Meitl, M.; Zhang, Y. W.; Huang, Y.; Rogers, J. A. Stretchable Semiconductor Technologies with High Areal Coverages and Strain-Limiting Behavior: Demonstration in High-Efficiency Dual-Junction GaInP/GaAs Photovoltaics. *Small* **2012**, *8* (12), 1851-1856.

(45) Cantarella, G.; Costanza, V.; Ferrero, A.; Hopf, R.; Vogt, C.; Varga, M.; Petti, L.; Münzenrieder, N.; Büthe, L.; Salvatore, G. Design of engineered elastomeric substrate for stretchable active devices and sensors. *Adv. Funct. Mater.* **2018**, *28* (30), 1705132.

(46) Wu, C.; Wang, X.; Lin, L.; Guo, H.; Wang, Z. L. Paper-based triboelectric nanogenerators made of stretchable interlocking kirigami patterns. *ACS Nano* **2016**, *10* (4), 4652-4659.

(47) Xu, R.; Zverev, A.; Hung, A.; Shen, C.; Irie, L.; Ding, G.; Whitmeyer, M.; Ren, L.; Griffin, B.; Melcher, J. Kirigami-inspired, highly stretchable micro-supercapacitor patches fabricated by laser conversion and cutting. *Microsyst. Nanoeng.* **2018**, *4* (1), 1-10.

(48) Chen, W.; Liu, L.-X.; Zhang, H.-B.; Yu, Z.-Z. Kirigami-inspired highly stretchable, conductive, and hierarchical Ti3C2T x MXene films for efficient electromagnetic interference shielding and pressure sensing. *ACS Nano* **2021**, *15* (4), 7668-7681.

(49) Guo, Z.; Yu, Y.; Zhu, W.; Zhang, Q.; Liu, Y.; Zhou, J.; Wang, Y.; Xing, J.; Deng, Y. Kirigami-Based Stretchable, Deformable, Ultralight Thin-Film Thermoelectric Generator for BodyNET Application. *Adv. Energy Mater.* **2022**, *12* (5), 2102993.

(50) Bartlett, M. D.; Fassler, A.; Kazem, N.; Markvicka, E. J.; Mandal, P.; Majidi, C. Stretchable, high-k dielectric elastomers through liquid-metal inclusions. *Adv. Mater.* **2016**, *28* (19), 3726-3731.

(51) Lee, B.; Cho, H.; Park, K. T.; Kim, J.-S.; Park, M.; Kim, H.; Hong, Y.; Chung, S. High-performance compliant thermoelectric generators with magnetically

self-assembled soft heat conductors for self-powered wearable electronics. *Nat. Commun.* **2020**, *11* (1), 1-12.

(52) Xu, J.; Wang, S.; Wang, G.-J. N.; Zhu, C.; Luo, S.; Jin, L.; Gu, X.; Chen, S.; Feig, V. R.; To, J. W. Highly stretchable polymer semiconductor films through the nanoconfinement effect. *Science* **2017**, *355* (6320), 59-64.

(53) Liu, J.; Wang, J.; Zhang, Z.; Molina-Lopez, F.; Wang, G. N.; Schroeder, B. C.; Yan, X.; Zeng, Y.; Zhao, O.; Tran, H.; et al. Fully stretchable active-matrix organic light-emitting electrochemical cell array. *Nat. Commun.* **2020**, *11* (1), 3362.

(54) Lee, S.; Reuveny, A.; Reeder, J.; Lee, S.; Jin, H.; Liu, Q.; Yokota, T.; Sekitani, T.; Isoyama, T.; Abe, Y. A transparent bending-insensitive pressure sensor. *Nat. Nanotechnol.* **2016**, *11* (5), 472-478.

(55) Taherian, R. Development of an equation to model electrical conductivity of polymer-based carbon nanocomposites. *ECS J. Solid State Sci. Technol.* **2014**, *3* (6), M26.

(56) Boudenne, A.; Mamunya, Y.; Levchenko, V.; Garnier, B.; Lebedev, E. Improvement of thermal and electrical properties of Silicone–Ni composites using magnetic field. *Eur. Polym. J.* **2015**, *63*, 11-19.

(57) Dong, S.; Wang, X. Alignment of carbon iron into polydimethylsiloxane to create conductive composite with low percolation threshold and high piezoresistivity: Experiment and simulation. *Smart Mater. Struct.* **2017**, *26* (4), 045027.

(58) Nielsen, L. E. Generalized equation for the elastic moduli of composite materials. *J. Appl. Phys.* **1970**, *41* (11), 4626-4627.

(59) Duffy, D. C.; Jackman, R. J.; Vaeth, K. M.; Jensen, K. F.; Whitesides, G. M. Electroluminescent Materials with Feature Sizes as Small as 5 μm Using Elastomeric Membranes as Masks for Dry Lift-Off. *Adv. Mater.* **1999**, *11* (7), 546-552.

(60) Wassei, J. K.; Tung, V. C.; Jonas, S. J.; Cha, K.; Dunn, B. S.; Yang, Y.; Kaner, R. B. Stenciling Graphene, Carbon Nanotubes, and Fullerenes Using Elastomeric Lift-Off Membranes. *Adv. Mater.* **2010**, *22* (8), 897-901.

(61) Tahk, D.; Paik, S.-M.; Lim, J.; Bang, S.; Oh, S.; Ryu, H.; Jeon, N. L. Rapid large area fabrication of multiscale through-hole membranes. *Lab Chip* **2017**, *17* (10), 1817-1825.

(62) Cho, H.; Kim, J.; Park, H.; Won Bang, J.; Seop Hyun, M.; Bae, Y.; Ha, L.; Do Kim, Y.; Min Kang, S.; Jung Park, T. Replication of flexible polymer membranes with geometry-controllable nano-apertures via a hierarchical mould-based dewetting. *Nat. Commun.* **2014**, *5* (1), 1-10.

(63) Hernández-Castro, J. A.; Li, K.; Meunier, A.; Juncker, D.; Veres, T. Fabrication of large-area polymer microfilter membranes and their application for particle and cell enrichment. *Lab Chip* **2017**, *17* (11), 1960-1969.

(64) Wong, H. C.; Zhang, Y.; Viasnoff, V.; Low, H. Y. Predictive Design, Etch-Free Fabrication of Through-Hole Membrane with Ordered Pores and Hierarchical Layer Structure. *Adv. Mater. Technol.* **2017**, *2* (2), 1600169.

(65) Bartolo, D.; Degré, G.; Nghe, P.; Studer, V. Microfluidic stickers. *Lab Chip* **2008**, *8* (2), 274-279.

(66) Zheng, Y.; Dai, W.; Ryan, D.; Wu, H. Fabrication of freestanding, microperforated membranes and their applications in microfluidics. *Biomicrofluidics* **2010**, *4* (3), 036504.

(67) Lamoureux, A.; Lee, K.; Shlian, M.; Forrest, S. R.; Shtein, M. Dynamic kirigami structures for integrated solar tracking. *Nat. Commun.* **2015**, *6* (1), 1-6.

(68) Lee, Y. K.; Jang, K. I.; Ma, Y.; Koh, A.; Chen, H.; Jung, H. N.; Kim, Y.; Kwak, J. W.; Wang, L.; Xue, Y. Chemical sensing systems that utilize soft electronics on thin elastomeric substrates with open cellular designs. *Adv. Funct. Mater.* **2017**, *27* (9), 1605476.

(69) Rong, Y.; Huang, Y.; Lin, C.; Liu, Y.; Shi, S.; Zhang, G.; Wu, C. Stretchability improvement of flexiable electronics by laser micro-drilling array holes in PDMS film. *Opt. Lasers Eng.* **2020**, *134*, 106307.

(70) Zhang, Y.; Lo, C. W.; Taylor, J. A.; Yang, S. Replica molding of high-aspect-ratio polymeric nanopillar arrays with high fidelity. *Langmuir* **2006**, *22* (20), 8595-8601.

(71) Kim, J. Y.; Park, K.-S.; Kim, Z.-S.; Baek, K.-H.; Do, L.-M. Fabrication of low-cost submicron patterned polymeric replica mold with high elastic modulus over a large area. *Soft Matter* **2012**, *8* (4), 1184-1189.

(72) Lin, Y.; Hu, Z.; Zhang, M.; Xu, T.; Feng, S.; Jiang, L.; Zheng, Y. Magnetically induced low adhesive direction of nano/micropillar arrays for microdroplet transport. *Adv. Funct. Mater.* **2018**, *28* (49), 1800163.

(73) Gong, S.; Schwalb, W.; Wang, Y.; Chen, Y.; Tang, Y.; Si, J.; Shirinzadeh, B.; Cheng, W. A wearable and highly sensitive pressure sensor with ultrathin gold nanowires. *Nat. Commun.* **2014**, *5* (1), 1-8.

(74) An, B. W.; Heo, S.; Ji, S.; Bien, F.; Park, J.-U. Transparent and flexible fingerprint sensor array with multiplexed detection of tactile pressure and skin temperature. *Nat. Commun.* **2018**, *9* (1), 1-10.

(75) Yin, B.; Liu, X.; Gao, H.; Fu, T.; Yao, J. Bioinspired and bristled microparticles for ultrasensitive pressure and strain sensors. *Nat. Commun.* **2018**, *9* (1), 1-8.

(76) Sun, J. Y.; Keplinger, C.; Whitesides, G. M.; Suo, Z. Ionic skin. *Adv. Mater.* **2014**, *26* (45), 7608-7614.

(77) Hua, Q.; Sun, J.; Liu, H.; Bao, R.; Yu, R.; Zhai, J.; Pan, C.; Wang, Z. L. Skin-inspired highly stretchable and conformable matrix networks for multifunctional sensing. *Nat. Commun.* **2018**, *9* (1), 1-11.

(78) Wu, W.; Wen, X.; Wang, Z. L. Taxel-addressable matrix of vertical-nanowire piezotronic transistors for active and adaptive tactile imaging. *Science* **2013**, *340* (6135), 952-957.

(79) Dagdeviren, C.; Su, Y.; Joe, P.; Yona, R.; Liu, Y.; Kim, Y.-S.; Huang, Y.; Damadoran, A. R.; Xia, J.; Martin, L. W. Conformable amplified lead zirconate titanate sensors with enhanced piezoelectric response for cutaneous pressure monitoring. *Nat. Commun.* **2014**, *5* (1), 1-10.

(80) Zhao, G.; Zhang, X.; Cui, X.; Wang, S.; Liu, Z.; Deng, L.; Qi, A.; Qiao, X.; Li, L.; Pan, C. Piezoelectric polyacrylonitrile nanofiber film-based dual-function self-powered flexible sensor. *ACS Appl. Mater. Interfaces* **2018**, *10* (18), 15855-15863.

(81) Pan, C.; Dong, L.; Zhu, G.; Niu, S.; Yu, R.; Yang, Q.; Liu, Y.; Wang, Z. L. High-resolution electroluminescent imaging of pressure distribution using a piezoelectric nanowire LED array. *Nat. Photonics* **2013**, *7* (9), 752-758.

(82) Peng, M.; Li, Z.; Liu, C.; Zheng, Q.; Shi, X.; Song, M.; Zhang, Y.; Du, S.; Zhai, J.; Wang, Z. L. High-resolution dynamic pressure sensor array based on piezo-phototronic effect tuned photoluminescence imaging. *ACS Nano* **2015**, *9* (3), 3143-3150.

(83) Wang, X.; Que, M.; Chen, M.; Han, X.; Li, X.; Pan, C.; Wang, Z. L. Full dynamic-range pressure sensor matrix based on optical and electrical dual-mode sensing. *Adv. Mater.* **2017**, *29* (15), 1605817.

(84) Wang, S.; Xu, J.; Wang, W.; Wang, G.-J. N.; Rastak, R.; Molina-Lopez, F.; Chung, J. W.; Niu, S.; Feig, V. R.; Lopez, J. Skin electronics from scalable fabrication of an intrinsically stretchable transistor array. *Nature* **2018**, *555* (7694), 83-88.

(85) Sim, K.; Rao, Z.; Kim, H.-J.; Thukral, A.; Shim, H.; Yu, C. Fully rubbery integrated electronics from high effective mobility intrinsically stretchable semiconductors. *Sci. Adv.* **2019**, *5* (2), eaav5749.

(86) Schwartz, G.; Tee, B. C.-K.; Mei, J.; Appleton, A. L.; Kim, D. H.; Wang, H.; Bao, Z. Flexible polymer transistors with high pressure sensitivity for application in electronic skin and health monitoring. *Nat. Commun.* **2013**, *4* (1), 1-8.

(87) Oh, H.; Yi, G.-C.; Yip, M.; Dayeh, S. A. Scalable tactile sensor arrays on flexible substrates with high spatiotemporal resolution enabling slip and grip for closed-loop robotics. *Sci. Adv.* **2020**, *6* (46), eabd7795.

(88) Matsuhisa, N.; Sakamoto, H.; Yokota, T.; Zalar, P.; Reuveny, A.; Lee, S.; Someya, T. A mechanically durable and flexible organic rectifying diode with a polyethylenimine ethoxylated cathode. *Adv. Electron. Mater.* **2016**, *2* (10), 1600259.

(89) You, I.; Choi, S. E.; Hwang, H.; Han, S. W.; Kim, J. W.; Jeong, U. E-skin tactile sensor matrix pixelated by position-registered conductive microparticles creating pressure-sensitive selectors. *Adv. Funct. Mater.* **2018**, *28* (31), 1801858.

(90) Roudaut, Y.; Lonigro, A.; Coste, B.; Hao, J.; Delmas, P.; Crest, M. Touch sense: functional organization and molecular determinants of mechanosensitive receptors. *Channels* **2012**, *6* (4), 234-245.

(91) Lee, B.; Oh, J.-Y.; Cho, H.; Joo, C. W.; Yoon, H.; Jeong, S.; Oh, E.; Byun, J.; Kim, H.; Lee, S. Ultraflexible and transparent electroluminescent skin for real-time and super-resolution imaging of pressure distribution. *Nat. Commun.* **2020**, *11* (1), 1-11.

(92) Mehdizadeh, A.; Mei, R.; Klausner, J. F.; Rahmatian, N. Interaction forces between soft magnetic particles in uniform and non-uniform magnetic fields. *Acta Mech. Sin.* **2010**, *26* (6), 921-929.

(93) Rosická, D.; Šembera, J. Influence of structure of iron nanoparticles in aggregates on their magnetic properties. *Nanoscale Res. Lett.* **2011**, *6* (1), 1-9.

(94) Dawson, J.; Adkins, C. Conduction mechanisms in carbon-loaded composites. *J. Phys. Condens. Matter* **1996**, *8* (43), 8321.

(95) Dargahi, J.; Najarian, S. Human tactile perception as a standard for artificial tactile sensing—a review. *Int. J. Med. Robot. Comput. Assist. Surg.* **2004**, *1* (1), 23-35.

(96) Tong, J.; Mao, O.; Goldreich, D. Two-point orientation discrimination versus the traditional two-point test for tactile spatial acuity assessment. *Front. Hum. Neurosci.* **2013**, *7*, 579.

(97) Suo, Z.; Ma, E.; Gleskova, H.; Wagner, S. Mechanics of rollable and foldable film-on-foil electronics. *Appl. Phys. Lett.* **1999**, *74* (8), 1177-1179.

(98) Mao, S.; Han, X.; Tian, Y.; Luo, J.; Zhang, Z.; Ji, Y.; Wu, M. In situ EBSD investigations of the asymmetric stress-induced martensitic transformation in TiNi shape memory alloys under bending. *Mater. Sci. Eng. A* **2008**, *498* (1-2), 278-282.

(99) Mao, L.; Meng, Q.; Ahmad, A.; Wei, Z. Mechanical analyses and structural design requirements for flexible energy storage devices. *Adv. Energy Mater.* **2017**, *7* (23), 1700535.

(100) Kim, T.-W.; Lee, J.-S.; Kim, Y.-C.; Joo, Y.-C.; Kim, B.-J. Bending strain and bending fatigue lifetime of flexible metal electrodes on polymer substrates. *Mater.* **2019**, *12* (15), 2490.

(101) Jeong, J. W.; Yeo, W. H.; Akhtar, A.; Norton, J. J.; Kwack, Y. J.; Li, S.; Jung, S. Y.; Su, Y.; Lee, W.; Xia, J. Materials and optimized designs for human-machine interfaces via epidermal electronics. *Adv. Mater.* **2013**, *25* (47), 6839-6846.

(102) Cho, H.; Lee, Y.; Lee, B.; Byun, J.; Chung, S.; Hong, Y. Stretchable strain-tolerant soft printed circuit board: A systematic approach for the design rules of stretchable interconnects. *J. Inf. Disp.* **2020**, *21* (1), 41-47.

(103) Choi, S.; Lee, S.; Lee, B.; Kim, T.; Hong, Y. Selective crack formation on stretchable silver nano-particle based thin films for customized and integrated strain-sensing system. *Thin Solid Films* **2020**, *707*, 138068.

(104) Chang, M.; Chen, B.-C.; Gabayno, J. L.; Chen, M.-F. Development of an optical inspection platform for surface defect detection in touch panel glass. *Int. J. Optomechatronics* **2016**, *10* (2), 63-72.

(105) Chen, S.-H.; Perng, D.-B. Automatic optical inspection system for IC molding surface. *J. Intell. Manuf.* **2016**, *27* (5), 915-926.

(106) Wang, W.-C.; Chen, S.-L.; Chen, L.-B.; Chang, W.-J. A machine vision based automatic optical inspection system for measuring drilling quality of printed circuit boards. *IEEE Access* **2016**, *5*, 10817-10833.

(107) Abd Al Rahman, M.; Mousavi, A. A review and analysis of automatic optical inspection and quality monitoring methods in electronics industry. *IEEE Access* **2020**, *8*, 183192-183271.

(108) Kandalaft, N.; Basith, I. I.; Rashidzadeh, R. Low-contact resistance probe card using MEMS technology. *IEEE Trans. Instrum. Meas.* **2014**, *63* (12), 2882-2889.

(109) Kim, B.-H.; Park, S.-J.; Chun, K.; Cho, D.-I.; Park, W.-K.; Jun, T.-U.; Yun, S. A fine pitch MEMS probe unit for flat panel display as manufacturing MEMS application. *Sens. Actuator A: Phys.* **2004**, *115* (1), 46-52.

(110) Watanabe, N.; Suzuki, M.; Kawano, K.; Eto, M.; Aoyagi, M. Fabrication of a membrane probe card using transparent film for three-dimensional integrated circuit testing. *Jpn. J. Appl. Phys.* **2014**, *53* (6S), 06JM06.

(111) Choi, W.-C.; Ryu, J.-Y. Fabrication of a guide block for measuring a device with fine pitch area-arrayed solder bumps. *Microsyst. Technol.* **2012**, *18* (3), 333-339.

(112) Roca-Cusachs, P.; Rico, F.; Martinez, E.; Toset, J.; Farre, R.; Navajas, D. Stability of microfabricated high aspect ratio structures in poly(dimethylsiloxane). *Langmuir* **2005**, *21* (12), 5542-5548.

(113) Yuan, B.; Li, Y.; Wang, D.; Xie, Y.; Liu, Y.; Cui, L.; Tu, F.; Li, H.; Ji, H.; Zhang, W.; et al. A General Approach for Patterning Multiple Types of Cells Using Holey PDMS Membranes and Microfluidic Channels. *Adv. Funct. Mater.* **2010**, *20* (21), 3715-3720.

(114) Pan, C.; Markvicka, E. J.; Malakooti, M. H.; Yan, J.; Hu, L.; Matyjaszewski, K.; Majidi, C. A Liquid-Metal-Elastomer Nanocomposite for Stretchable Dielectric Materials. *Adv. Mater.* **2019**, *31* (23), e1900663.

(115) Hong, S. Y.; Jee, S. M.; Ko, Y.; Cho, J.; Lee, K. H.; Yeom, B.; Kim, H.; Son, J. G. Intrinsically Stretchable and Printable Lithium-Ion Battery for Free-Form Configuration. *ACS Nano* **2022**, *16* (2), 2271-2281.

(116) Wang, W.; Wang, S.; Rastak, R.; Ochiai, Y.; Niu, S.; Jiang, Y.; Arunachala, P. K.; Zheng, Y.; Xu, J.; Matsuhisa, N. Strain-insensitive intrinsically stretchable transistors and circuits. *Nat. Electron.* **2021**, *4* (2), 143-150.

(117) Zheng, Y. Q.; Liu, Y.; Zhong, D.; Nikzad, S.; Liu, S.; Yu, Z.; Liu, D.; Wu, H. C.; Zhu, C.; Li, J.; et al. Monolithic optical microlithography of high-density elastic circuits. *Science* **2021**, *373* (6550), 88-94.

(118) Kim, J. H.; Park, J. W. Intrinsically stretchable organic light-emitting diodes. *Sci. Adv.* **2021**, *7* (9), eabd9715.

(119) Lee, J. N.; Park, C.; Whitesides, G. M. Solvent compatibility of poly(dimethylsiloxane)-based microfluidic devices. *Anal. Chem.* **2003**, *75* (23), 6544-6554.

(120) Biswas, S.; Schoeberl, A.; Hao, Y.; Reiprich, J.; Stauden, T.; Pezoldt, J.; Jacobs, H. O. Integrated multilayer stretchable printed circuit boards paving the way for deformable active matrix. *Nat. Commun.* **2019**, *10* (1), 4909.

(121) Xiang, Z.; Wang, H.; Wan, J.; Miao, L.; Xu, C.; Zhao, P.; Guo, H.; Zhang, H.; Han, M. High-density stretchable microelectrode array based on multilayer serpentine interconnections. *J. Micromech. Microeng.* **2022**, *32* (8), 084002.

(122) La, T. G.; Qiu, S.; Scott, D. K.; Bakhtiari, R.; Kuziek, J. W. P.; Mathewson, K. E.; Rieger, J.; Chung, H. J. Two-Layered and Stretchable e-Textile Patches for Wearable Healthcare Electronics. *Adv. Healthc. Mater.* **2018**, *7* (22), 1801033.

(123) Ren, P.; Dong, J. Direct Fabrication of VIA Interconnects by Electrohydrodynamic Printing for Multi-Layer 3D Flexible and Stretchable Electronics. *Adv. Mater. Technol.* **2021**, *6* (9), 2100280.

(124) Sun, P.; Zhang, J.; Zhu, X.; Li, H.; Li, Y.; Yang, J.; Peng, Z.; Zhang, G.; Wang, F.; Lan, H. Directly Printed Interconnection Wires between Layers for 3D Integrated Stretchable Electronics. *Adv. Mater. Technol.* **2022**, *7* (9), 2200302.

(125) Huang, Z.; Hao, Y.; Li, Y.; Hu, H.; Wang, C.; Nomoto, A.; Pan, T.; Gu, Y.; Chen, Y.; Zhang, T.; et al. Three-dimensional integrated stretchable electronics. *Nat. Electron.* **2018**, *1* (8), 473-480.

(126) Green Marques, D.; Alhais Lopes, P.; A, T. d. A.; Majidi, C.; Tavakoli, M. Reliable interfaces for EGaIn multi-layer stretchable circuits and microelectronics. *Lab Chip* **2019**, *19* (5), 897-906.

(127) Jiang, Q.; Zhang, S.; Jiang, J.; Fei, W.; Wu, Z. Pneumatic Enabled Vertical Interconnect Access of Liquid Alloy Circuits toward Highly Integrated Stretchable Electronics. *Adv. Mater. Technol.* **2021**, *6* (3), 2000966.

(128) Pan, X.; He, H. Fabrication and integration of functional stretchable circuit based on liquid metal. *J. Phys. D: Appl. Phys.* **2022**, *55* (38), 384003.

(129) Jin, S.; Tiefel, T. N.; Wolfe, R. Directionally-conductive, optically-transparent composites by magnetic alignment. *IEEE Trans. Magn.* **1992**, *28* (5), 2211-2213.

(130) Jang, S. H.; Park, Y. L.; Yin, H. Influence of Coalescence on the Anisotropic Mechanical and Electrical Properties of Nickel Powder/Polydimethylsiloxane Composites. *Mater.* **2016**, *9* (4), 239.

(131) Beran, T.; Mulholland, T.; Henning, F.; Rudolph, N.; Osswald, T. A. Nozzle clogging factors during fused filament fabrication of spherical particle filled polymers. *Addit. Manuf.* **2018**, *23*, 206-214.

(132) Ha, J.; Seo, J.; Lee, S.; Oh, E.; Lee, T.; Chung, S.; Hong, Y. Efficient Surface Treatment to Improve Contact Properties of Inkjet-Printed Short-Channel Organic Thin-Film Transistors. *J. Nanosci. Nanotechnol.* **2017**, *17* (8), 5718-5721.

(133) Oh, E.; Kim, T.; Yoon, J.; Lee, S.; Kim, D.; Lee, B.; Byun, J.; Cho, H.; Ha, J.; Hong, Y. Highly Reliable Liquid Metal-Solid Metal Contacts with a Corrugated Single-Walled Carbon Nanotube Diffusion Barrier for Stretchable Electronics. *Adv. Funct. Mater.* **2018**, *28* (51), 1806014.

(134) Miccoli, I.; Edler, F.; Pfnur, H.; Tegenkamp, C. The 100th anniversary of the four-point probe technique: the role of probe geometries in isotropic and anisotropic systems. *J. Phys. Condens. Matter* **2015**, *27* (22), 223201.

Publication List

International Journals

1. **J. Seo**, J. Yoon, G. Kim, H. Cho, D. Jang, H. Yoon, S. Choi, and Y. Hong*, "Micro-Structured Anisotropic Elastomer Composite-Based Vertical Interconnect Access (VIA) for Multi-Layered Stretchable Electronics", *ACS Appl. Mater. Interfaces* (submitted)

2. **J. Seo**, J. Ha, B. Lee, H. Kim, and Y. Hong*, "Fluoroelastomer encapsulation for enhanced reliability of solution-processed carbon nanotube thin-film transistors", *Thin Solid Films* **704**, 138021 (2020)

3. J. Ha†, H. Yoo†, **J. Seo**, J. Yoon, and Y. Hong*, "Photoresponse Analysis of All-Inkjet-Printed Single-Walled Carbon Nanotube Thin-Film Transistors for Flexible Light-Insensitive Transparent Circuit Applications", *ACS Appl. Mater. Interfaces* **15**, 2, 3192-3201 (2023)

4. G. Kim, J. Yoon, H. Yoon, H. Cho, **J. Seo**, and Y. Hong*, "High-resolution maskless patterning of AgNWs based on adhesion enhancement of printed conductive polymer", *Flex. Print. Electron*. **7**, 4, 045009 (2022)

5. H. Kim†, S. Choi†, B. Lee, **J. Seo**, S. Lee, J. Yoon, and Y. Hong*, "Nonpatterned Soft Piezoresistive Films with Filamentous Conduction Paths for Mimicking Multiple-Resolution Receptors of Human Skin", *ACS Appl. Mater. Interfaces* **14**, 49, 55088-55097 (2022)

6. B. Park, J. Jang, H. Kim, **J. Seo**, H. Yoo, T. Kim, and Y. Hong*, "Enhanced current path by circularly and periodically-aligned semiconducting single-

walled carbon nanotubes for logic circuit device", *Flex. Print. Electron*. **7**, 015005 (2022)

7. D. Kim, D. K. Lee, J. Yoon, D. Hahm, B. Lee, E. Oh, G. Kim, **J. Seo**, and Y. Hong*, "Electronic Skin Based on Cellulose/Carbon Nanotube Fiber Network for Large-Area 3D Touch and Real-Time 3D Surface Scanning", *ACS Appl. Mater. Interfaces* **13**, 44, 53111-53119 (2021)

8. B. Park, J. Jang, H. Kim, **J. Seo**, H. Yoo, T. Kim*, and Y. Hong*, "Dense Assembly of Finely Patterned Semiconducting Single-Walled Carbon Nanotubes via a Selective Transfer Method of Nanotube-Attracting Layers", *ACS Appl. Mater. Interfaces* **12**, 38441 (2020)

9. H. Yoo, J. Ha, H. Kim, **J. Seo**, S.-Y. Lee*, and Y. Hong*, "Tunable Stability of All-Inkjet-Printed Double-Gate Carbon Nanotube Thin Film Transistors", *IEEE Electron Device Lett.* **41**, 6 (2020)

10. H. Kim, **J. Seo**, N. Seong, S. Lee, S. Lee, T. Kim*, and Y. Hong*, "Multi-Dipping Technique for Fabrication Time Reduction and Performance Improvement of Solution-Processed Single-walled Carbon Nanotube Thin-Film Transistors", *Adv. Eng. Mater.* **22**, 8, 1901413 (2020)

11. B. Lee†, J.-Y. Oh*†, H. Cho, C. W. Joo, H. Yoon, S. Jeong, E. Oh, J. Byun, H. Kim, S. Lee, **J. Seo**, C. W. Park, S. Choi, N.-M. Park, S.-Y. Kang, C.-S. Hwang, S.-D. Ahn, J.-I. Lee, and Y. Hong*, "Ultraflexible and transparent electroluminescent skin for real-time and super-resolution imaging of pressure distribution", *Nat. Commun.* **11**, 663 (2020)

12. J. Park, H. Yoon, G. Kim, B. Lee, S. Lee, S. Jeong, T. Kim, **J. Seo**, S. Chung, and Y. Hong*, "Highly Customizable All Solution–Processed Polymer Light Emitting Diodes with Inkjet Printed Ag and Transfer Printed Conductive Polymer Electrodes", *Adv. Funct. Mater.* **29**, 1902412 (2019)

13. T.-Y. Kim†, J. Ha†, K. Cho, J. Pak, **J. Seo**, J. Park, J.-K. Kim, S. Chung*, Y. Hong*, and T. Lee*, “Transparent Large-Area MoS2 Phototransistors with Inkjet-Printed Components on Flexible Platforms”, *ACS Nano* **11**, 10273 (2017)

14. J. Ha, **J. Seo**, S. Lee, E. Oh, T. Lee, S. Chung*, and Y. Hong*, "Efficient Surface Treatment to Improve Contact Properties of Inkjet-Printed Short-Channel Organic Thin-Film Transistors", *J. Nanosci. Nanotechnol.* **17**, 5718 (2017)

Conferences

1. **J. Seo,** G. Kim, J. Yoon, H. Cho, D. Jang, H. Kim, and Y. Hong*, "Customizable Soft Vertical Interconnect Access Utilizing Micro-Perforated Elastomer Membrane for Stretchable Multi-layered Circuits", 2022 Materials Research Society (MRS) Spring Meeting & Exhibit, Honolulu, USA, May (2022) (Oral)

2. **J. Seo**, S. Choi, H. Kim, D. Kim, H. Yoon, and Y. Hong*, "Stretchable Pressure Sensor Using Conductive Silicone Elastomer Composite with Rigid Island Structure", The 21th International Meeting on Information Display 2021 (IMID 2021), Seoul/Online, Korea, August (2021) (Poster)

3. **J. Seo**, S. Choi, H. Kim, S. Lee, and Y. Hong*, "A Soft Probe Unit for Flexible Electronic Device Inspection Using Conductive Silicone Elastomer Composite", FLEX 2020, San Jose, USA, February (2020) (Poster)

4. **J. Seo**, J. Ha, B. Lee, H. Kim, and Y. Hong*, "Fluoropolymer Encapsulation for Hysteresis-free-All-solution-processed Single-walled Carbon Nanotube Thin-film Transistors", The 5th International Conference on Advanced Electromaterials (ICAE 2019), Jeju island, Korea, November (2019) (Oral)

5. **J. Seo**, S. Choi, H. Kim, S. Lee, and Y. Hong*, "A Soft Probe Unit Using Conductive Silicone Elastomer Composite for Flexible Electronic Device Inspection", The 19th International Meeting on Information Display 2019 (IMID 2019), Gyeongju, Korea, August (2019) (Poster)

6. **J. Seo**, J. Ha, B. Lee, H. Kim, and Y. Hong*, “Hysteresis-free All-solution-processed Single-Walled Carbon Nanotube Thin-film Transistors Encapsulated with Fluoropolymer”, The 27th International Conference on Amorphous and Nanocrystalline Semiconductors (ICANS 27), Seoul, Korea, August (2017) (Poster)

7. **J. Seo**, J. Ha, T. Kim, N. Seong, H. Kim, and Y. Hong*, "Reduced turn-on voltage of all-solution-processed single-walled carbon nanotube thin-film transistors encapsulated with PDMS elastomer", The 8th International Workshop on Flexible & Printable Electronics (IWFPE 2016), Jeonju, Korea, November (2016) (Poster)

Patents

1. 홍용택, **서지석**, 김한울, "신축성 압력센서 어레이 및 그의 제조방법", 10-2023-0007771, 서울대학교산학협력단

2. 홍용택, 김한울, **서지석**, "신축성 압력센서 어레이 및 그를 포함하는 전자 장치", 10-2022-0151043, 서울대학교산학협력단

국 문 초 록

소프트 전자 소자(soft electronics)는 기기에 유연성(flexibility)을 넘어 신축성(stretchability)을 부여함으로써, 플렉시블 소자로는 구현할 수 없었던 다양한 변형이 가능한 전자 장치의 구현을 가능하게 한다. 소프트 전자 소자를 통한 미래지향적인 기기의 구현을 위해서는 단일 소자를 신축성 플랫폼에 집적하여 다기능 시스템을 구현하는 것이 필요하다. 이러한 고집적 다기능 시스템을 구현하기 위한 구성 요소는 단일 기능성 소자, 단일 소자의 3 차원 집적을 가능하게 하는 비아, 그리고 신호 전달과 기기의 검사를 위한 전기적 연결을 형성하는 프로브 유닛, 이렇게 크게 세 가지의 항목으로 나눌 수 있다. 각각의 구성 요소에 신축성뿐만 아니라 적합한 기능성을 부여하기 위해서 재료적인 측면과 구조적인 측면에서의 전략법이 사용된다. 본 논문에서는 자기장에 의해 유도되는 이방성 복합소재와 천공성 구조의 도입을 통해 각 구성 요소를 신축성 플랫폼 상에 구현하는 방법에 대해 논의한다.

다기능 시스템을 위한 단일 소자로서, 인체의 다양한 촉각의 해상도를 구현할 수 있는 고해상도 유연 압력 센서가 개발된다. 자기장을 통한 강자성 복합소재의 패턴 형성 가능성을 유한 요소

분석법을 통한 시뮬레이션으로 확인하고, 센서 픽셀을 분리시키기 위한 프레임의 필요성에 대해 논의한다. 천공성 구조물의 도입을 통해 패터닝된 압력 센서의 해상도가 이점식별검사를 통해 100 ppi 로 확인된다. 결론적으로, 100 ppi 의 해상도에서 실시간 압력 분포 측정 및 압력 분류가 출력 시스템을 통해 구현되었다.

신호 전달과 검사 공정을 위한 연결 장치로서, 변형 가능한 기기의 전극에의 물리적 접촉에 의해 발생하는 손상을 막을 수 있는 유연 프로브 유닛이 개발된다. 천공성 구조 형성을 위한 최적화된 공정을 통해 접촉 전극들 사이에 전기적 혼선이 발생하지 않는 500 ppi 해상도의 프로브 유닛이 제작된다. 유연 기판 상에 잉크젯 프린팅으로 제작된 전극에 적용함으로써, 프로브 유닛의 낮은 접촉 저항과 보호 특성을 확인한다. 플렉시블 디스플레이 패널의 검사를 위한 FPCB 커넥터나 용액 공정으로 제작된 폴리머 발광 다이오드(PLED) 전극에의 도입을 통해, 제안된 프로브 유닛의 실용화 가능성이 입증된다.

마지막으로 단일 소자를 집적하기 위한 연결부로서, 다층 구조를 위한 간단한 적층 공정 적용이 가능하고 기계적 내구성이 뛰어난 비아가 개발된다. 유한 요소 분석 시뮬레이션과 실제 샘플의 디지털 이미지 상관 분석을 통해, 인장 시 비아에 작용되는 기계적 응력(stress)을 신축성 기판으로 분산시키는 마이크로 구조물의 효과를 분석한다. 제안된 비아의 기계적 내구성과 신뢰성은 신축 테스트에서 전송선

기법과 4 선 저항 측정법을 결합한 전기적 측정을 통해 확인된다. 다층 신축성 전자 기기를 위한 제안된 접근법의 실현 가능성은 구겨지거나 2 축 인장 상태에서도 안정적으로 동작하는 수동 매트릭스 방식의 신축 발광 다이오드 배열을 통해 입증된다.

본 논문은 마이크로 구조를 가지는 이방성 엘라스토머 복합소재를 활용하여 고집적 신축 전자 소자를 위한 핵심 구성 요소를 구현하는 방법론을 제시한다는 데에 큰 의의가 있다. 자기장의 형성, 충전제의 특성 조절, 그리고 마이크로 구조의 도입을 통해 기능성 부여와 소자 성능 향상이 이루어진다. 제안된 방법론의 실현 가능성에 대한 입증과 더불어, 몰드를 활용해 제작된 마이크로 천공성막의 간단하고 대면적 공정 가능성은 제안된 기술의 상용화를 손쉽게 만들어 준다. 본 논문에서 다루어진 유연 전자 소자의 구현을 위한 다양한 설계, 분석, 그리고 최적화를 동반하는 체계적인 접근법은 고집적 다기능 신축성 전자 시스템의 구현을 위한 토대를 닦을 것으로 기대된다.

키워드 : 유연 전자 소자, 엘라스토머 복합소재, 압력 센서, 프로브 유닛, 비아, 마이크로 구조, 이방성 복합소재, 강자성

학번 : 2016-20919